

ICE NUCLEATION BY SURROGATES FOR ATMOSPHERIC MINERAL DUST
AND MINERAL DUST/SULFATE PARTICLES AT CIRRUS TEMPERATURES

by

Cassie M. Archuleta

Department of Atmospheric Science

Colorado State University

Fort Collins, CO

NSF

Under grant # NSF ATM-0071321

AMS Industry / Government Graduate Fellowship

Sponsored by NOAA's Office of Global Programs

March, 2003

ABSTRACT

ICE NUCLEATION BY SURROGATES FOR ATMOSPHERIC MINERAL DUST
AND MINERAL DUST/SULFATE PARTICLES AT CIRRUS TEMPERATURES

This research examines the potential role of some types of mineral dust as heterogeneous ice nuclei at cirrus temperatures. Commercially available nanoscale powder samples of aluminum oxide, alumina-silicate and iron oxide were atomized from suspensions, dried and selected at monodisperse sizes (50 to 200 nm) for use as surrogates for atmospheric mineral dust particles. A tube furnace with a linear temperature gradient was used to condense sulfuric acid on the particles. The degree of acid coatings on the particles was determined by measuring their cloud condensation activity with a static thermal gradient diffusion chamber and applying Köhler theory for mixed particles. Measurements of ice nucleation were made using a continuous flow ice-thermal diffusion chamber (CFDC) operated to expose aerosols to temperatures between -45 and -60°C and a range of relative humidity above ice-saturated conditions.

A clear size effect was indicated for ice formation by all of the particles as larger particles consistently nucleated ice at lower humidity than smaller particles at the same temperatures. Ice nucleation results from the minerals without a sulfuric acid coating indicate that relatively pure mineral oxide aerosols that are larger than about 100 nm nucleate ice at lower relative humidity than that required to homogeneously freeze sulfuric acid drops of the same size. The freezing nucleation behavior of the same mineral oxides coated with approximately 1-2 monolayers of sulfuric acid indicated

heterogeneous freezing by core particles larger than about 100 nm at lower relative humidity than values calculated to be required for homogeneous freezing of the diluted particle coatings. Nevertheless, the particles nucleated at generally higher relative humidity than the respective uncoated particles. It is theorized that the particle coatings rendered surface active sites of the untreated particles inactive.

A sample of reference Asian dust was also examined for ice nucleation properties in the same manner as done for the manufactured particles. Strong size effects on nucleation were also noted for these natural particles. The 200 nm natural mineral dust particles were the most effective ice nuclei tested in this study, activating heterogeneous ice formation at an ice relative humidity of around 133%, irrespective of temperature.

Results are shown to compare well, at least in form, to those obtained in two other recent studies and it is demonstrated that modified homogeneous freezing parameterizations work quite well for describing the results for use in numerical models.

Acknowledgments

First, I would like to extend gratitude to my advisor, Prof. Sonia Kreidenweis for her constant support. Equally, I would like to thank Dr. Paul DeMott, whose enthusiasm, expertise and insight were essential during the progression of this research. Thank you also to my other committee members, Prof. William Cotton and Prof. Tina Rinker for the time, effort and input they provided.

Thanks to Dr. Tony Prenni who offered help and advice in operating the CFDC and to Brian Jesse who contributed his skill in the maintenance, and in some cases the construction, of experimental equipment. Thanks also to Dr. Prenni and to Dr. Sarah Brooks for performing the HTDMA analysis presented this study. I would also like to acknowledge Dr. Masutaka Nishikawa who extended considerable effort in collecting and refining the Asian mineral dust sample used in this study.

Thank you to the National Science Foundation for financially supporting this research and NOAA's Office of Global Programs who sponsored me with a fellowship through the American Meteorological Society.

Lastly, I would like to acknowledge the ongoing support of my family including my husband Ruben, my son Simon and my parents.

Table of Contents

1. Introduction.....	1
1.1 <i>Cirrus clouds and climate feedback.....</i>	<i>1</i>
1.2 <i>Ice Formation Processes in Cirrus Clouds.....</i>	<i>2</i>
1.2.1 Homogeneous freezing nucleation.....	2
1.2.2 Heterogeneous nucleation.....	5
1.3 <i>Mineral dust in the upper troposphere</i>	<i>6</i>
1.4 <i>Objectives and Expected Significance</i>	<i>8</i>
2. Instrumentation.....	10
2.1 <i>Particle Generation system.....</i>	<i>11</i>
2.1.1 Constant Output Atomizer	11
2.1.2 Differential Mobility Analyzer	12
2.1.3 Sulfuric acid coating system	16
2.2 <i>Condensation Nuclei Counter.....</i>	<i>18</i>
2.3 <i>Humidified Tandem Differential Mobility Analyzer</i>	<i>20</i>
2.4 <i>Cloud Condensation Nuclei Counter.....</i>	<i>21</i>
2.5 <i>Continuous Flow Diffusion Chamber.....</i>	<i>24</i>
2.6 <i>Data Acquisition</i>	<i>28</i>
3. Experimental Results.....	30
3.1 <i>Sample Information.....</i>	<i>30</i>
3.1.1 Commercially produced nanoparticles	30
3.1.2 Asian Mineral Dust Sample	32
3.2 <i>HTDMA water uptake results</i>	<i>34</i>
3.3 <i>CCN Results.....</i>	<i>36</i>
3.3.1 Aluminum oxide, alumina-silicate and iron oxide.....	37
3.4 <i>CFDC Results</i>	<i>42</i>
3.4.1 Aluminum Oxide	43
3.4.2 Alumina-silicate.....	45
3.4.3 Iron Oxide	46
3.4.4 Asian mineral dust sample	47
4. Discussion and conclusions	53
4.1 <i>Summary of results.....</i>	<i>53</i>
4.2 <i>Comparison to other laboratory investigations.....</i>	<i>59</i>
4.2.1 Parameterization using freezing point depression	59

4.2.2	Parameterization using water activity	64
4.2.3	Nucleation rates for ice formation	67
4.3	<i>Conclusions</i>	72
4.4	<i>Recommendations for Future Work</i>	74
Appendix A		77
Appendix B		83
Appendix C		87
REFERENCES		95

List of Figures

<i>Figure 2.1: Overall schematic of the particle generation and classification systems.....</i>	<i>10</i>
<i>Figure 2.2: Schematic of the atomizer (adapted from TSI Model 3075/3076 Constant Output Atomizer manual, 1994).....</i>	<i>12</i>
<i>Figure 2.3: Schematic of DMA (from TSI Model 3071A Classifier manual, 2000). Note that the flow rates in this figure are double the flow rates actually used for these experiments.</i>	<i>15</i>
<i>Figure 2.4: The experimentally determined bipolar charge distribution of aerosol particles in atmospheric air (points) compared with the Fuchs model (lines) (from Wiedensohler and Fissan, 1991).....</i>	<i>16</i>
<i>Figure 2.5: Horizontal temperature profile in the tube furnace.....</i>	<i>18</i>
<i>Figure 2.6: Flow schematic of the CNC (from TSI Model 3025A UCPC Manual, 2002). Bypass flow is not a consideration when operating at 0.3 lpm.</i>	<i>20</i>
<i>Figure 2.7: Schematic diagram of the humidified tandem differential mobility analyzer (from Prenni et al., 2001).</i>	<i>21</i>
<i>Figure 2.8: Horizontal cross section of the CCN counter.....</i>	<i>24</i>
<i>Figure 2.9: Vertical cross section and supersaturation profile for the CCN counter.....</i>	<i>24</i>
<i>Figure 2.10: Schematic of the CFDC.</i>	<i>27</i>
<i>Figure 2.11: Steady-state temperature, supersaturation and velocity profile inside the CFDC.....</i>	<i>28</i>
<i>Figure 2.12: The data display mode of the CFDC data acquisition program developed by Original Code Consulting of Boulder, Co. The upper left graph is the temperature profile in the CFDC, the upper right is the ice and water supersaturation conditions, the lower left is the CN profile and the IN profile, and the lower right is the MCA particle size spectra (the darker color is a five second sum and the white is a 1 second value). ..</i>	<i>30</i>
<i>Figure 3.1: Number size distributions for aluminum oxide (squares), alumina-silicate (triangles) and iron oxide (circles) as determined at CSU using a scanning DMA coupled with a CPC.....</i>	<i>32</i>

<i>Figure 3.2: Number size distribution of the mineral dust sample. The distribution above 0.3 μm (300 nm) was determined Dr. Masataka Nishikawa, National Institute for Environmental Studies, Japan. Size distribution below 0.3 μm was determined at CSU using a scanning DMA coupled with a CNC.</i>	<i>34</i>
<i>Figure 3.3: HTDMA water uptake results for 50 nm (circles) 100 nm (triangles) and 200 nm (squares) Asian dust particles.</i>	<i>35</i>
<i>Figure 3.4: Measured CCN activity for 100 nm (a) and 200 nm (b) aluminum oxide particles. Symbols indicate cases of untreated aluminum oxide particles (closed circles) and aluminum oxide particles treated with H_2SO_4 (open circles). The lines indicate exponential fits to the data, and S_{crit} is the point on the line where 50% of the particles have activated as CCN.</i>	<i>39</i>
<i>Figure 3.5: As in Figure 3.2, but for 100 (a) and 200 (b) nm alumina-silicate particles.</i>	<i>40</i>
<i>Figure 3.6: As in Figure 3.2, but for 100 (a) and 200 (b) nm iron oxide particles.</i>	<i>41</i>
<i>Figure 3.7: Average CFDC conditions for the formation of ice on 1% of aluminum oxide particles. Data are presented for 50 nm (circles), 100 nm (triangles), and 200 nm (squares) aerosol particles. Error bars indicate a 95% confidence level (see appendix C). For comparison homogeneous freezing for pure H_2SO_4 particles are included for 50 nm (dotted), 100 nm (dash-dot) and 200 nm (dashed) conditions based on observations from Chen et al. (2000). Also included is a line for $\text{RH}_w = 100\%$.</i>	<i>49</i>
<i>Figure 3.8: Average CFDC conditions for the formation of ice on 1% of aluminum oxide particles treated with H_2SO_4. Data are presented for 50 nm (circles), 100 nm (triangles), and 200 nm (squares) aerosol particles. Error bars indicate a 95% confidence level (see appendix C). Lines indicate predictions for the conditions required for homogeneous freezing of the H_2SO_4 coatings on the 50 nm (dotted), 100 nm (dash-dot) and 200 nm (dashed) core particles, based on Chen et al. (2000). Also included is a line for $\text{RH}_w = 100\%$.</i>	<i>49</i>
<i>Figure 3.9: As in Figure 3.5, but for CFDC conditions for the formation of ice on 1% of alumina-silicate particles.</i>	<i>50</i>
<i>Figure 3.10: As in Figure 3.6, but for CFDC conditions for the formation of ice on 1% of alumina-silicate particles treated with H_2SO_4.</i>	<i>50</i>
<i>Figure 3.11: As in Figure 3.5, but for CFDC conditions for the formation of ice on 1% of iron oxide particles.</i>	<i>51</i>
<i>Figure 3.12: As in Figure 3.6, but for CFDC conditions for the formation of ice on 1% of iron oxide particles treated with H_2SO_4.</i>	<i>51</i>

Figure 3.13: As in Figure 3.5, but for CFDC conditions for the formation of ice on 1% of particles from the reference sample of Asian dust particles..... 52

Figure 4.1: The ice formation conditions of 200 nm untreated mineral oxide particles (a) and the treated mineral aerosols along with the Asian dust aerosols (b). A line summarizing the relative humidity required for cirrus nucleation (HM95) derived in a different study (FIRE-II) by Heymsfield and Miloshevich (1995) is also shown. Other lines indicate conditions for homogeneous freezing of 200 nm pure sulfate particles based on CFDC measurements by Chen et al. (2000) and saturation with respect to water. 58

Figure 4.2: Example of data for heterogeneous freezing temperature vs. water activity. The dark solid curve is the activity of water in a bulk solution in equilibrium with ice (a_w^i) and the intersecting solid horizontal line is the bulk freezing temperature for pure water (273.15K) (Buck, 1981). The diamonds represent heterogeneous freezing data (1% of particles freezing in the CFDC residence time) for 200 nm treated Al_2O_3 particles. Arrows represent the melting point depression for pure water (ΔT_m) and the nucleation point depression for diluted sulfuric acid with a mineral immersion ($\lambda \Delta T_m$). The dotted line represents the equation $T = 244 - 1.6 \Delta T_m$ (a) and horizontal dotted line represents the temperature at which pure water with a mineral immersion is expected to freeze (T_{hetf0}). The solid line represents a_w^i shifted by $\Delta a_w = 0.42$ 63

Figure 4.3: Comparison of freezing data using line fits to constant Δa_w . The thick solid line represents results from Zuberi et al. (2002) for large koalinite and montmorillite inclusions in aqueous $(NH_4)_2SO_4$. The dotted (dashed) lines represent results from this study for 100 nm (200 nm) aluminum oxide, alumina-silicate and iron oxide particles with H_2SO_4 coatings..... 66

Figure 4.4: Number size distributions of hematite cores prepared from several different $FeCl_3(aq)$ precursor concentrations (from Hung et al., 2002). Particles generated from 10 mM $FeCl_3(aq)$ precursor had an 80 nm mode (1), 100 mM a 150 nm mode (2) and 1000 mM a 250 nm mode (3). 70

Figure 4.5: Lines with open diamonds represent lines of constant a_w for 1.0 and 0.1% activation of 100 and 200 nm aluminum oxide particles treated with H_2SO_4 . Lines with filled diamonds represent data from Hung et al. (2002) for constant a_w lines indicating between 0.003 and 0.000003% activation of aluminum oxide particles treated with $(NH_4)_2SO_4$ with mode diameters of 50, 120, 150 and 200 nm. The different lines represent $a_w = 0.91$ (solid) $a_w = 0.87$ (dashed) and $a_w = 0.79$ (dotted). 71

Figure 4.6: Lines with open diamonds represent lines of constant a_w for 1.0 and 0.1% activation of 50, 100 and 200 nm iron oxide particles treated with H_2SO_4 . Lines with filled diamonds represent data from Hung et al. (2002) for constant a_w lines indicating between 0.03 and 0.0003% activation of iron oxide particles treated with $(NH_4)_2SO_4$ with mode diameters of 80, 150 and 250 nm. The different lines represent $a_w = 0.91$ (solid) $a_w = 0.87$ (dashed) and $a_w = 0.79$ (dotted). 71

List of Tables

<i>Table 2.1: Diameter of particles and fraction of the total particle concentration (assuming an even distribution) corresponding to selected diameters.....</i>	<i>16</i>
<i>Table 3.1: Descriptions of nanoscale powder products as provided by the NanoProducts Corporation in Longmont, CO.....</i>	<i>31</i>
<i>Table 3.2: Chemical constituents of the sample as determined by ICP analysis with acid digestion ($\text{HNO}_3 + \text{HClO}_4 + \text{HF}$) treatment. Si was not determined, but can be assumed to be about 28%. Data provided by Dr. Masataka Nishikawa, National Institute for Environmental Studies, Japan.</i>	<i>33</i>
<i>Table 3.3: The weight % of sulfuric acid deposited on the mineral particles determined using S_{crit} and Köhler theory for partially soluble spheres. The corresponding number of monolayers of acid is included in parenthesis where spherical particles are assumed with uniform coverage.</i>	<i>42</i>
<i>Table 4.1: Comparison of the best fit equations for two methods, $T=T_l+\lambda T_m$ and $\Delta a_w=a_w-a_w^i$, used to describe heterogeneous nucleation data for treated 100 and 200 nm aluminum oxide, alumina silicate particles and treated 50, 100 and 200 nm iron oxide particles. Also included is r^2 for each equation as compared to the experimental data set.</i>	<i>64</i>

1. Introduction

In order to unravel the intricacies of climate change, it is important to include the role of cirrus clouds. The net impact of cirrus clouds on our climate system is determined by the balance between the reflectance of incoming solar radiation back to space and the trapping of outgoing infrared fluxes emitted from the earth's surface. These radiative properties are strongly impacted by the microphysical composition, altitude and frequency of formation of cirrus clouds. Upper tropospheric aerosols indirectly affect these physical properties through their role in the ice formation process. Mineral dust aerosols are of particular interest for this study because of their common atmospheric occurrence and inferred presence in cirrus cloud residuals.

1.1 *Cirrus clouds and climate feedback*

Cirrus clouds appear globally in the upper troposphere, at altitudes of 8 to 15 km, and recent studies indicate that as much as 30% of the earth is covered with cirrus at any given time (Liou, 1986; Dowling and Radke, 1990). Cirrus are ice-dominated clouds inhabiting the upper troposphere with their most distinguishing characteristic being their optical thickness. High-level cirrus are normally optically thin and nonblack, consisting of low concentrations (on the order of 1-100 per liter) of nonspherical ice particles (Liou, 1986).

The effects of cloud radiation feedbacks play a major role in climate perturbation processes. For example, total cloud forcing is on the order of -20 W m^{-2} as compared to the average radiative forcing of -2.5 W m^{-2} by greenhouse gases today (Penner et al.,

2001) which implies that even small changes in their radiative properties could be important. The effect of cirrus on the radiative balance of the earth-atmosphere system depends on the greenhouse-verses-albedo effect, which incorporates both the solar and infrared radiative properties of the clouds (Liou, 1986).

Because of their high location in the atmosphere and low reflection of incoming solar flux, Liou (1986) suggests that it is physically recognized that the presence of cirrus clouds will normally produce a greenhouse effect from their downward emission. In a model study by Stephens et al. (1990) it is demonstrated that this predicted greenhouse effect is influenced by inadequate treatment of the physics of cirrus clouds and that the impact of cirrus on climate change remains largely elusive. The conclusions of Stephens et al. were based upon modeling studies indicating that even the sign of any feedback that might exist between cirrus clouds and climate is sensitive to cloud microphysical and macrophysical properties that are either poorly known or poorly understood.

1.2 *Ice Formation Processes in Cirrus Clouds*

Aerosol particles affect the microphysical properties of cirrus clouds through their role in ice formation processes. Presently, it is unclear what the relative roles of homogeneous versus heterogeneous ice formation processes are under different atmospheric conditions (DeMott et al., 1999).

1.2.1 Homogeneous freezing nucleation

Homogeneous freezing nucleation refers to the spontaneous freezing of cloud droplets and haze particles that usually occurs below about -40°C . This involves soluble particles that deliquesce and dilute as they equilibrate with rising relative humidity and

cooling during lifting of air parcels. One common basis for quantifying homogeneous ice nucleation in cirrus for use in numerical models has been from classical nucleation theory. The validity of this approach for cloud droplets is supported by numerous laboratory studies on the freezing of pure water and dilute solution drops (see, e.g., Pruppacher and Klett, 1997). In contrast, quantifying laboratory observations of homogeneous ice nucleation of more concentrated solution droplets at lower cirrus temperatures has required use of empirical or semi-empirical parameterizations (e.g., Chen et al., 2000; Koop et al., 2000). Since most observations suggest that the bulk of upper tropospheric particles are primarily composed of sulfates, the homogeneous freezing nucleation of sulfate particles has dominated laboratory studies (DeMott, 2002).

The potential inadequacy of homogeneous freezing as the singular mechanism for cirrus cloud formation may be understood by comparing the conditions required for homogeneous freezing of sulfate haze particles in the cirrus regime to atmospheric observations of the conditions required for cirrus formation. There are some observations of environmental conditions for which cirrus were observed to be present. Figure 1.1 shows frequency distributions of relative humidity with respect to ice (RH_i) and temperature (Jensen et al., 2001) derived from aircraft measurements inside and outside cirrus clouds. The figure represents data from the 1996 Subsonic Aircraft: Contrail and Cloud Effects Study (SUCCESS) which was an aircraft campaign conducted over the central and western United States. Some maritime samples are also represented in the data set. For this study, efforts were made to sample regions where the relative humidity was forecast to be high such that cirrus and/or persistent contrails would be likely. Data are segregated for updraft velocities below 1 m s^{-1} to limit the oversaturation that occurs

in strong updrafts. Overlain on the figure is an average of the conditions required for homogeneous freezing of liquid sulfate aerosols based on laboratory data (Koop et al., 2000; Chen et al., 2000). Also included in the figure is the RH_i for the onset of continental cirrus cloud formation based on observations of Heymsfield and Milosевич (1995) during the NASA FIRE-II program. If one considers that the peak RH_i values are indicative of values required for cloud formation in the respective studies, then the figure shows that the large ice supersaturations required to homogeneously freeze sulfate aerosols do not correspond to the full range of conditions for the formation of ice observed in cirrus clouds.

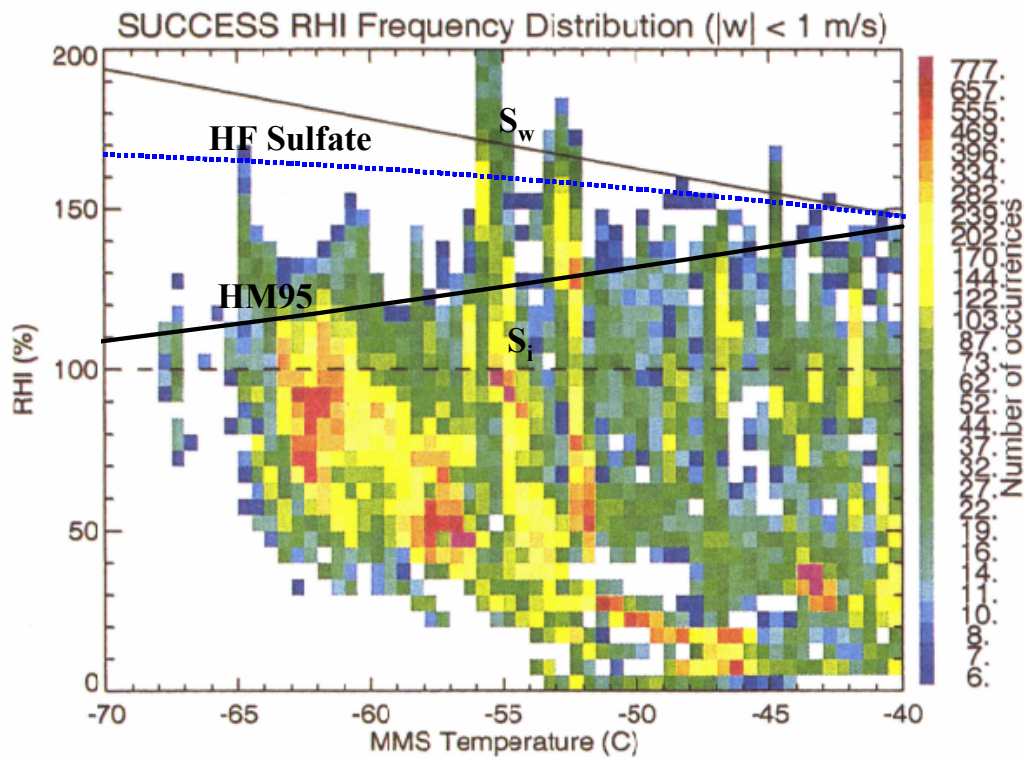


Figure 1.1: Probability distribution of 1 s observations of temperature and RH_i inside and outside cirrus when cirrus were present at flight level (from Jensen et al., 2001). Observations are from the 1996 NASA SUCCESS program and includes data only when updrafts were below 1 m s^{-1} . Overlain on the Figure are lines for the homogeneous freezing of pure sulfates (HF Sulfate) from measurements by Koop et al. (2000) or Chen et al. (2000) and the relative humidity for cirrus nucleation (HM95) derived from field measurements by Heymsfield and Milosевич (1995). Also indicated are saturation with respect to ice (S_i) and saturation with respect to water (S_w).

1.2.2 Heterogeneous nucleation

As suggested by Figure 1.1, it is possible that some cirrus clouds may be formed via some heterogeneous nucleation mechanism. Heterogeneous nucleation refers to the catalytic action of an insoluble particle (e.g. soot or mineral aerosol) leading to ice formation either directly or within the condensed liquid phase. At least four mechanisms have been identified as possibilities for heterogeneous ice nucleation. Condensation freezing is the condensation of water vapor on a nucleus that catalyzes freezing instantaneously. Immersion freezing is similar to condensation freezing and refers to the nucleation of a cloud drop by an ice nucleus that is immersed within the drop. Vapor deposition nucleation involves the direct deposition of ice from the vapor phase onto an insoluble surface or onto un-deliquesced sulfate salt particles. There is also a contact nucleation mode of freezing, which refers to the nucleation of a supercooled drop by a solid particle that makes contact with the drop. The theoretical basis for quantifying heterogeneous nucleation is less certain than for homogeneous freezing because theoretical descriptions require information on complex surface properties for innumerable substances that could act as ice nuclei (DeMott, 2002).

Heterogeneous nucleation mechanisms are clearly important for ice formation in precipitating clouds warmer than -40°C , but there is inferential evidence that they may be important as well for cirrus clouds. Single particle analysis of atmospheric aerosols indicates that while a bulk sample might be dominated by sulfate, most individual particles are internally mixed containing both insoluble and soluble components (Noble and Prather, 1996). DeMott et al. (1999) performed one of very few studies of heterogeneous nucleation in the cirrus regime. This study involved black carbon (soot)

particles generated with various layered coatings of sulfuric acid. Those studies indicated that soot particles with multi-layer sulfuric acid coatings at temperatures below -53°C lowered, by up to 10%, the relative humidity (with respect to water) necessary to nucleate pure sulfuric acid particles. This was the first direct evidence for the potential importance of this heterogeneous mechanism in cirrus clouds. Numerical model simulations also suggest that heterogeneous nucleation could dominate in cirrus formed by the widespread slow ascent of air (DeMott et al., 1997; Jensen and Toon, 1997). The predicted consequences of the presence of heterogeneous ice nuclei in such cirrus are lowered number concentrations of ice crystals forming at warmer temperatures and requiring lower relative humidity for formation. Lower crystal concentrations forming sooner in updraft cycles also lead to a mode of larger crystals.

Because heterogeneous nucleation is effective at warmer temperatures than homogeneous freezing nucleation, even relatively modest populations of ice nuclei (IN) can have substantial impacts on the conditions under which cirrus clouds could form (DeMott et al., 1994). The impacts of heterogeneous nucleation on the formation of cirrus clouds could have significant implications for the extent and duration of cirrus cloud cover, which could ultimately impact climate.

1.3 *Mineral dust in the upper troposphere*

Minerals comprise the dominant mass fraction of the atmospheric aerosol burden (Buseck and Posfai, 1999). Every year anywhere from 200-5000 metric tons of mineral dust are emitted from arid and semi-arid regions into the atmosphere. The size of arid regions is increasing by millions of hectares per year due to changes in precipitation and

anthropogenic disturbances, including overgrazing, devegetation, erosion, land salinization and mining activities (Zhang and Carmichael, 1999).

While dusts are often characterized as supermicron aerosols that would not be readily transported to the upper troposphere except by deep convection, this description is only applicable on a mass basis. In fact, the mode number size of African dust is at or below 1 μm (Afeti and Resch, 2000) and size distributions are highly dispersive.

Ambient dust at and near source regions is dry and usually consists of an irregularly shaped insoluble core, with components including silicates, aluminosilicates, iron and other metal oxides. These particles can also advect long distances and become coated with aqueous solutions of sulfates, nitrates and other electrolytes when passing through marine or polluted continental regions (Zhang and Carmichael, 1999). Dentener et al. (1996) calculate that 50-70% of sulfate in the vicinity of dust source regions is associated with mineral aerosol. The mechanism by which sulfate is found on mineral dust is believed to originate from evaporating cloud drops, which were originally nucleated on sulfate cloud condensation nuclei (CCN) and subsequently collected by dry interstitial mineral dust particles (Levin et al., 1996). Such dust particles are also sometimes found without significant sulfate or condensed components, especially away from urban areas.

Mineral dusts from the arid regions of the Asiatic continent were implicated as possible heterogeneous ice nuclei many years ago by Isono et al. (1959). Isono et al. used air trajectory analysis to show that high IN concentrations over Japan and the northwestern U.S. are often the result of local dust storms over arid regions of North China and Mongolia. More recently, further evidence has emerged indicating that mineral particles may serve as efficient ice nuclei in cirrus clouds. In an aircraft

campaign conducted over the Alps, Heintzenberg et al. (1996) found that minerals (with similar compositions to Pinatubo ash and Saharan dust) were a common constituent in cirrus crystal residues. Upper tropospheric IN activated in a diffusion chamber and subsequently collected (Chen et al., 1998) also had enhanced number fractions of crustal particles when compared with the ambient aerosol population. A study of lidar data by Sassen (2002) suggests cirrus ice clouds associated with transported Asian aerosols are considerably warmer than climatological means for cirrus.

In addition, some recent laboratory studies indicate the possible role of mineral dust associated with sulfate as effective ice nuclei. Zuberi et al. (2002) used drops (10-55 μm) of $(\text{NH}_4)_2\text{SO}_4$ with immersions of the clay minerals kaolinite and montmorillonite to determine that the mineral immersions lead to freezing at warmer temperatures than those required for homogeneous freezing of the $(\text{NH}_4)_2\text{SO}_4$ solution in these large drops. Hung et al. (2002) studied ice freezing of $(\text{NH}_4)_2\text{SO}_4(\text{aq})$ particles containing hematite (Fe_2O_3) and corundum (Al_2O_3) mineral dust cores using FTIR spectroscopy, and reported that the cores induce freezing heterogeneously at temperatures warmer than homogeneous nucleation.

1.4 Objectives and Expected Significance

Because laboratory findings regarding homogeneous freezing nucleation alone do not represent the full range of the conditions at which cirrus form, it is hypothesized that the inclusion of heterogeneous nucleation could give a more accurate representation of cirrus cloud behavior.

The current study focuses on the role of mineral aerosols as likely insoluble components of heterogeneous IN. The objectives of this research are to quantify the

heterogeneous freezing rates of submicrometer iron oxide, aluminum oxide and alumina-silicate particles, both alone and as multi-component particles with soluble H_2SO_4 coatings as well as the ice nucleation rates of a sample of reference Asian dust. The experiments exposed nearly monodisperse samples of the submicrometer aerosols (0.05-0.2 μm) to cirrus-relevant temperatures between -45 and -60°C and a range of relative humidity above ice-saturated conditions to map out regions of RH_i and temperature space where significant ice nucleation rates occur.

The experimental results reported here can be used to develop quantitative descriptions of the ice nucleating behavior of these aerosols, and compare these with existing observations of ice formation in clouds. These results will be useful for modeling ice formation in cirrus conditions, interpreting observations of ice formation in clouds, and predicting the radiative forcing of cold clouds. From this study we also expect to provide some enlightenment as to whether desertification and deforestation may influence cirrus clouds by affecting the abundances of IN transported to the upper troposphere by dust storms and subsequent convection and atmospheric dispersion. Also, there may be implications to the future need to study mineral dust effects on precipitating cloud systems.

2. Instrumentation

This chapter describes the individual instruments used for generating and analyzing ice nucleating behavior of metal oxides and metal oxides with surface coatings of sulfuric acid. The approach taken in this study involves atomizing nanoscale powder samples from suspensions using a constant output atomizer, size selecting using a differential mobility analyzer (DMA), and coating the particles with sulfuric acid using a tube furnace characterized by a linear temperature gradient. These coated particles are sent to a condensation nuclei counter (CNC) and simultaneously to either a cloud condensation nuclei (CCN) counter or to the continuous flow diffusion chamber (CFDC). The CFDC is equipped with an optical particle counter (OPC) to detect ice crystals nucleated from particles and a software system for data acquisition and display. Figure 2.1 is an overall schematic of the particle generation and classification systems described in this section.

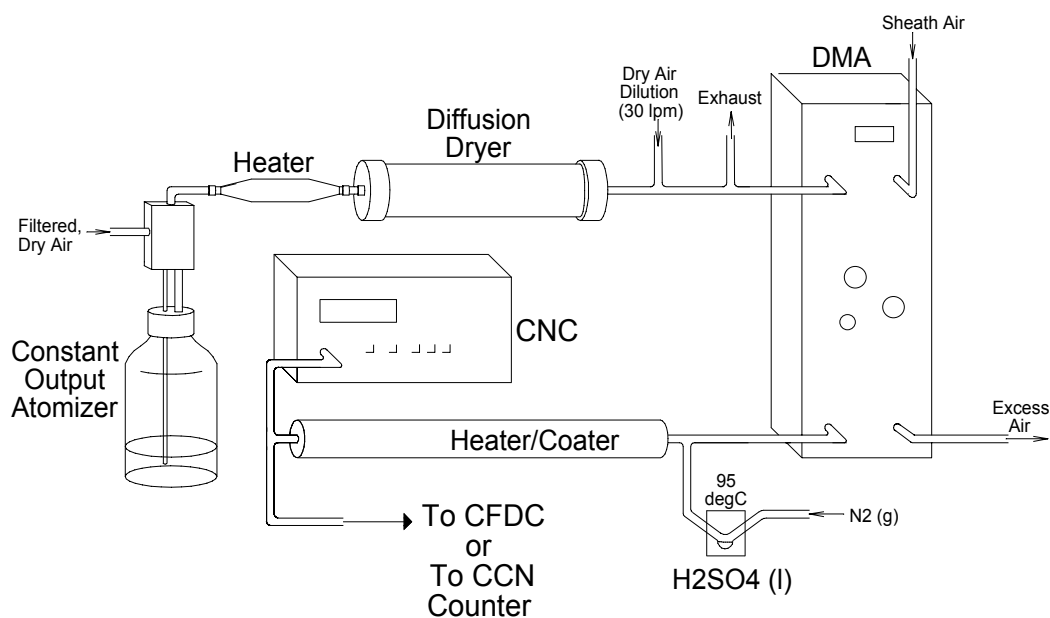


Figure 2.1: Overall schematic of the particle generation and classification systems.

2.1 Particle Generation system

2.1.1 Constant Output Atomizer

Continuous particle streams were generated using a Constant Output Atomizer (TSI 3076). Reservoir solutions for the atomizer consisted of 1.0 weight percent mixtures of particles suspended in high purity water. The particle suspensions were sustained using a magnetic stirrer.

A schematic of the atomizer is shown in Figure 2.2. The atomizer operates by forcing particle-free compressed air through a 0.0135 inch diameter orifice, forming a high-velocity jet. The jet passes over a vertical inlet that leads to the reservoir and draws liquid up to be atomized by the jet. Large droplets are removed by impaction on the wall opposite the jet. Excess liquid drains back into the reservoir through the bottom of the atomizer and a fine spray containing particles exits through the top of the atomizer.

Before the particle stream is sent to other instrumentation, it is first dried and diluted. The 1 lpm particle stream passes first through a heater that heats the stream to 60°C and then moisture is removed by a diffusion dryer (TSI 3062). A dilution of ~30 lpm of filtered, dry compressed air is then introduced, which serves the double purpose of additionally drying the particles and lowering the particle number density. From this particle stream the attached instrumentation pulls off about 1.0 lpm, and the excess is sent to exhaust.

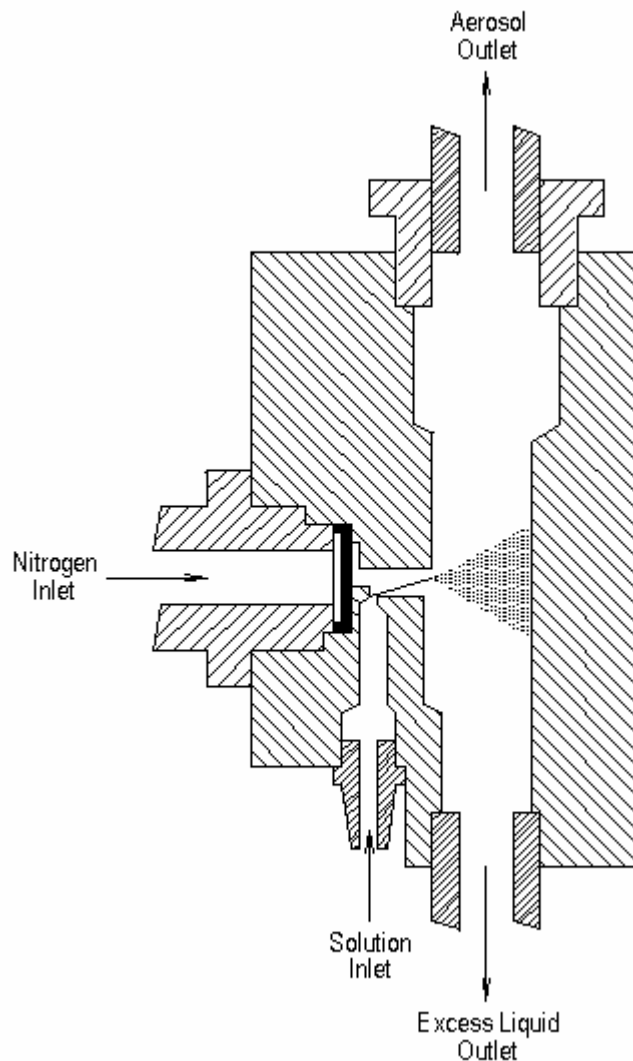


Figure 2.2: Schematic of the atomizer (adapted from TSI Model 3075/3076 Constant Output Atomizer manual, 1994).

2.1.2 Differential Mobility Analyzer

A nearly monodisperse distribution of particles is size-selected from the polydisperse aerosol using a differential mobility analyzer (DMA). Particles are separated in the DMA based upon the relationship between electrical mobility and particle size (see appendix A.1). A schematic of the DMA is shown in Figure 2.3.

Upon entering the DMA the sample passes through a Kr-85 neutralizer, which exposes the aerosol to high concentrations of bipolar ions. The ions collide with the

particles and quickly reach a state of equilibrium where particles carry a bipolar charge distribution. This charged polydisperse aerosol, along with clean sheath air, is introduced at the top of the instrument and flows down the annular space between the two concentric cylinders. The sheath:aerosol flow ratio is maintained at 10:1 and stream flow is laminar through the annulus. This flow ratio defines the width of the mobility (diameter) channel. The inner cylinder (the collector rod) is maintained at a controlled negative voltage between 1 and 10,000 volts, while the outer cylinder is electrically grounded. The voltage chosen dictates the size of the particles separated from the particle stream by creating an electric field between the two cylinders and causing positively charged particles to be attracted through the sheath air to the negatively charged collector rod. Particles that are smaller than the desired size are precipitated along the length of the collector rod with the location of the precipitating particles depending on the particle electrical mobility. Particles with a narrow range of electrical mobilities exit as monodisperse air flow through a small slit at the bottom of the collector rod. Particles larger than the desired size do not have sufficient mobility to reach the slit and exit the DMA through the excess air line. The excess:monodisperse flow ratio is also maintained at 10:1.

A purely monodisperse distribution is not achieved by mobility classification because some of the particles become more than singly charged. While the majority of charged particles carry a single charge, a fraction exists as multiply charged particles. Multiple charges on a larger particle give it a higher mobility, equal to that of a smaller, singly charged particle. This means that some larger particles reach the exit slit of the DMA and are carried in the monodisperse flow along with particles of the desired size.

The equilibrium charge distribution is asymmetrical because the fraction of negatively charged particles is larger than the fraction of positively charged particles. Wiedensohler (1988) developed a theoretical model for particle charge distribution that is a modification of the original theory by Fuchs (1963). Figure 2.4 from Wiedensohler (1991) shows the measured data from Wiedensohler and theoretical curves from the modified Fuchs theory. The figure indicates that the theoretical charge distribution agrees well with experimental data.

For the purposes of this research, we are interested in the charge distribution that might be encountered with the selection of 50, 100 and 200 nm diameter particles. Table 2.1 shows the size and fraction of particles corresponding to the charge distribution encountered for a selected diameter. The particle fractions are calculated for conditions in our laboratory using formulas from Wiedensohler (1988) and a derivation by Gunn in 1956 (TSI 3071A Classifier manual, 2000) (see appendix A.1). These fractions are determined for an even size distribution, so the actual proportion of multiplets are determined by the form of the size distribution (see Appendix A.3).

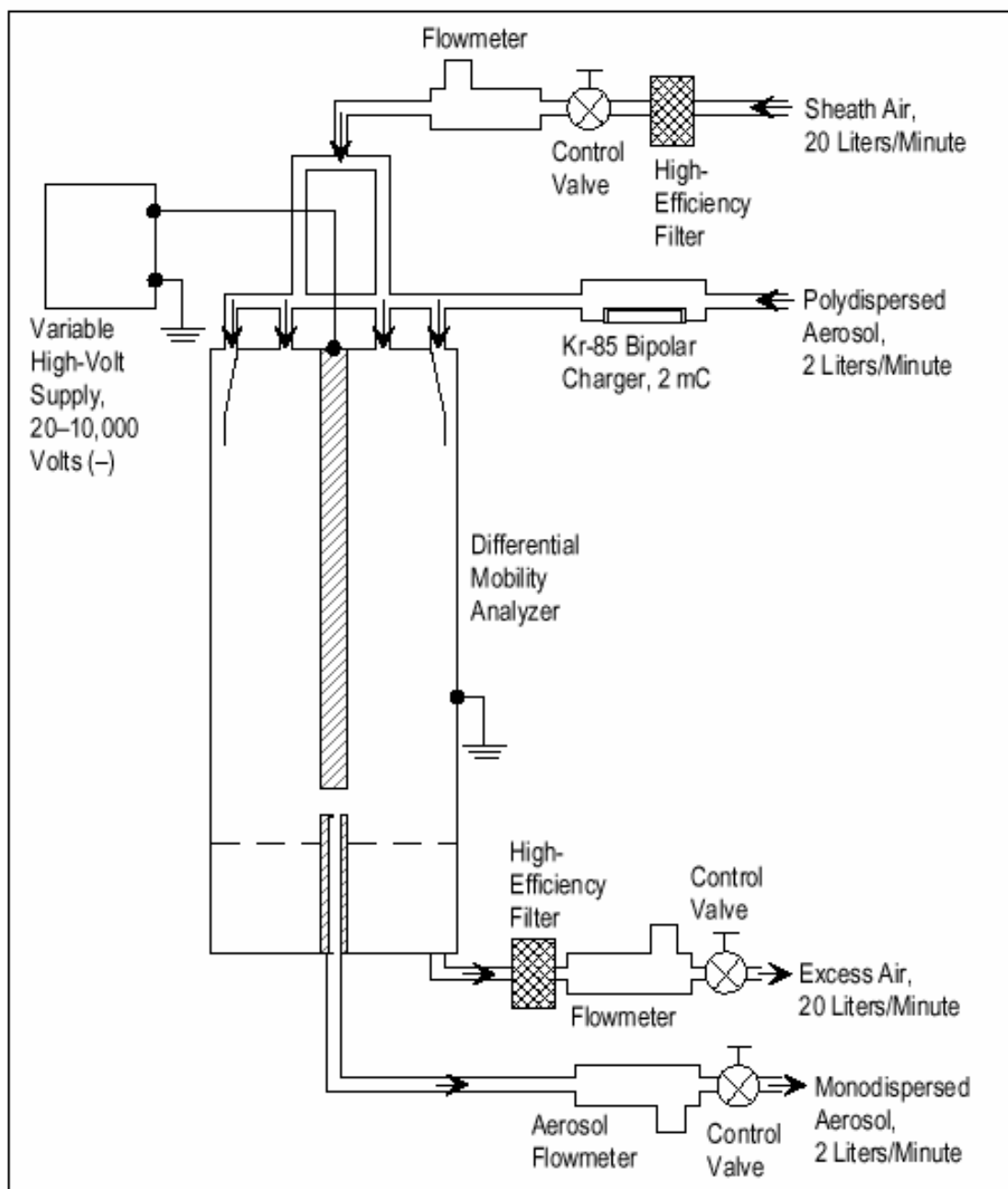


Figure 2.3: Schematic of DMA (from TSI Model 3071A Classifier manual, 2000). Note that the flow rates in this figure are double the flow rates actually used for these experiments.

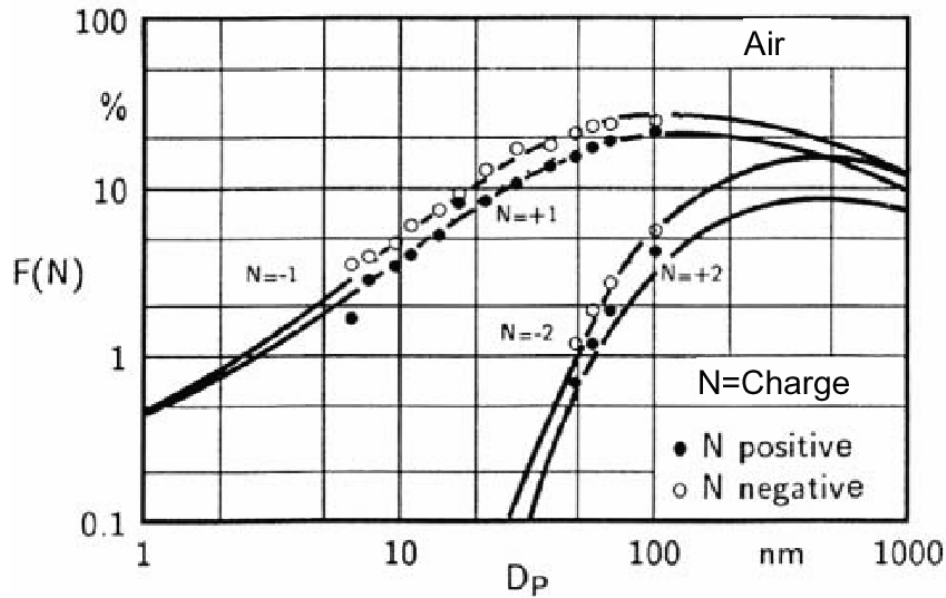


Figure 2.4: The experimentally determined bipolar charge distribution of aerosol particles in atmospheric air (points) compared with the Fuchs model (lines) (from Wiedensohler and Fissan, 1991).

Table 2.1: Diameter of particles and fraction of the total particle concentration (assuming an even distribution) corresponding to selected diameters.

Selected Diameter (nm)	Diameter of Particle in nm (<i>Fraction of total particle concentration</i>) corresponding to electrical mobility from indicated number of positive charges.		
	+1	+2	+3
50	50 (0.17)	72 (0.01)	90 (0.00)
100	100 (0.21)	149 (0.03)	191 (0.00)
200	200 (0.20)	317 (0.07)	426 (0.01)

2.1.3 Sulfuric acid coating system

To generate particles of mixed composition, in this case surrogate mineral dust particles with sulfuric acid coatings, a system is employed to condense the soluble material onto the insoluble cores. The system has two components that include a heated reservoir to volatilize sulfuric acid and produce condensed-phase particles after cooling,

and a tube furnace that re-volatilizes the acid and deposits it on the surface of the insoluble particles.

Sulfuric acid droplets are formed in a similar manner as described in Chen et al. (2000). The sulfuric acid is contained in a small glass bubble in the elbow of a ¼" glass tube. The tube is held in an aluminum block along with a heater, a thermocouple, and a temperature controller that monitors and regulates the temperature of the block. The temperature of the system is maintained at 95°C and high purity nitrogen gas flows over the acid drop at 0.1 lpm. Under these conditions, sulfuric acid evaporates and is transported in the carrier gas where it rapidly cools and nucleates H₂SO₄ particles homogeneously. The stream that is laden with sulfuric acid is then mixed with monodisperse mineral dust particles exiting the DMA.

The combined particle stream enters a custom-designed tube furnace (Han and Martin, 2001). The tube furnace is an insulated Pyrex tube (1.2 m × 1.5 cm id) wrapped with a resistive heating element in steadily decreasing pitch. The temperature is regulated and monitored with two temperature controllers and two thermocouples that are attached to the outside of the tube. The first 20 cm are wrapped at the same pitch and controlled by one temperature controller, and the next 80 cm are wrapped with decreasing pitch with the temperature controller attached to the first 10 cm of this region. The remaining portion of the tube is left unheated. Figure 2.5 shows the temperature profile achieved by setting each of the controllers to heat the outside of the tube to 210°C and with a total flow rate through the tube of 2.0 lpm. The tube is designed so that the sulfuric acid component of the aerosol stream entering the tube will volatilize in the hot end of the tube, and condense onto the mineral dust cores as the stream steadily cools

along the decreasing temperature gradient. The result is a stream of monodisperse mineral dust cores coated with sulfuric acid.

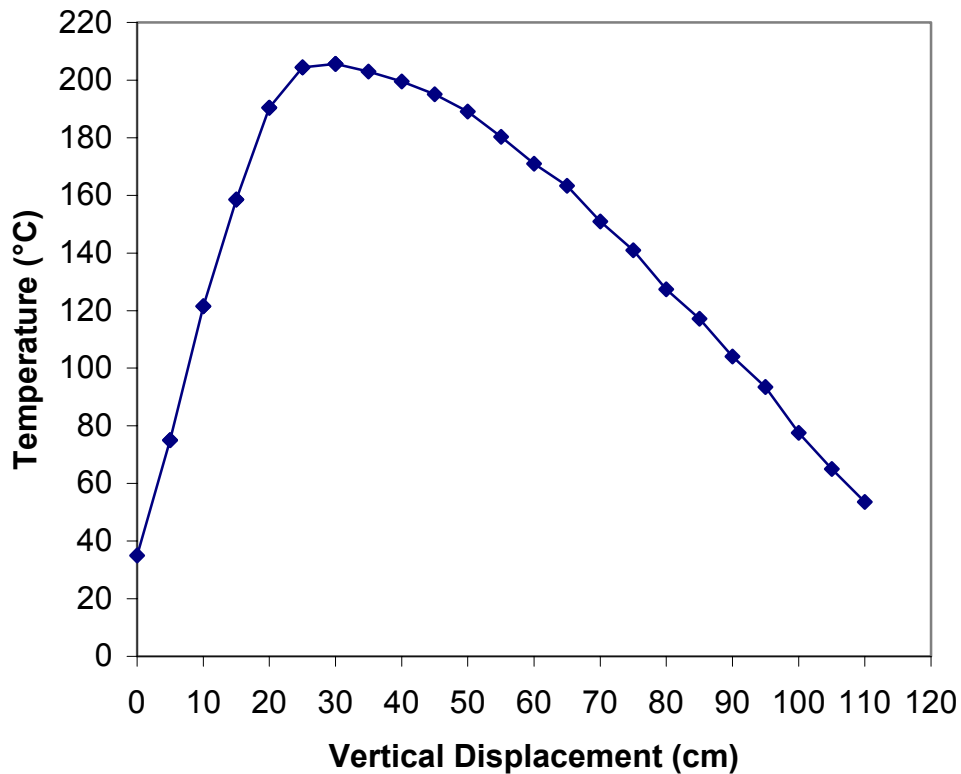


Figure 2.5: Horizontal temperature profile in the tube furnace.

2.2 Condensation Nuclei Counter

A Condensation Nuclei Counter (CNC, TSI Model 3025A), also called an Ultrafine Condensation Particle Counter (UCPC), is used to determine total particle concentration. Submicrometer particles are drawn into the counter and grow by condensation of butanol until reaching sizes that measure several micrometers in diameter that can be optically detected. This instrument is capable of detecting particles smaller than 0.01 micrometer in diameter, at concentrations from less than 0.01 up to 9.99×10^4 particles/cm³ (TSI Model 3025A UCPC Manual, 2002).

In operation, the air sample is pulled through the CNC at 0.3 lpm. The aerosol stream is separated into sample flow and sheath flow. The sheath flow is filtered before entering a saturator section where it passes over a heated, butanol soaked wick. The wick continually draws butanol from a reservoir bottle that is attached outside the instrument. The butanol evaporates in the heated saturator and saturates the sheath air flow with butanol vapor.

The aerosol stream is routed through a capillary tube and is injected into the centerline of a vertical condenser tube. The vapor-saturated sheath air rejoins the sample as a laminar flow. The stream is then cooled and the vapor begins to condense on the particles in the sample stream to form larger droplets. The droplets pass from the condenser tube through a nozzle into the optical particle detector.

The optical particle detector has a laser diode light source. Light scattered by the particles is collected by a photodetector as electrical pulses, which are counted in real time and displayed on the front panel of the instrument. The CNC is also capable of full computer interfacing, and is connected via a serial cable to the data acquisition PC. A flow schematic of the CNC is shown in Figure 2.6.

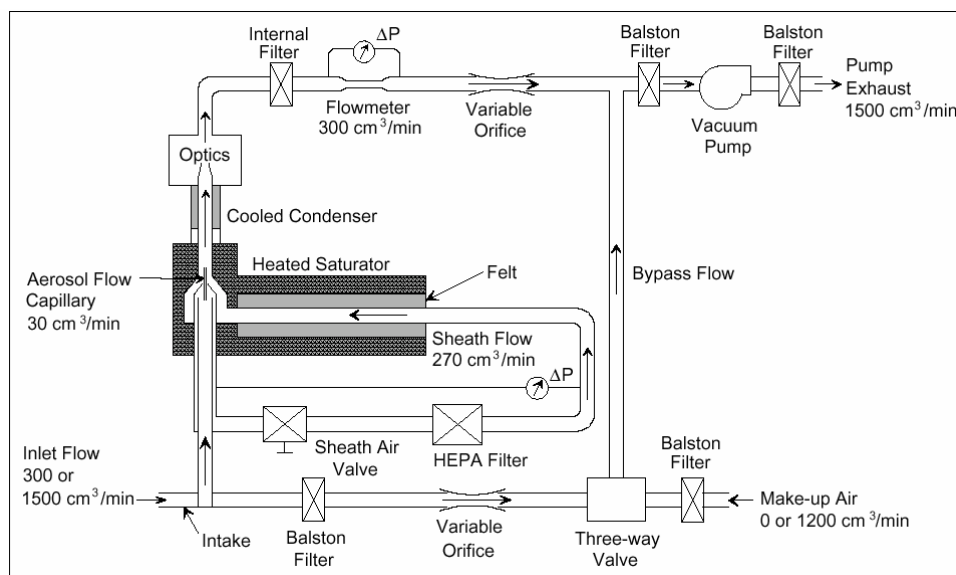


Figure 2.6: Flow schematic of the CNC (from TSI Model 3025A UCPC Manual, 2002). Bypass flow is not a consideration when operating at 0.3 lpm.

2.3 Humidified Tandem Differential Mobility Analyzer

The humidified tandem differential mobility analyzer (HTDMA) is used to measure the hygroscopic growth of the mineral particles. It has been used previously in our laboratory (e.g., Brechtel and Kreidenweis 2000). Two DMA instruments are coupled with two CNC instruments for this analysis. The apparatus is shown schematically in Figure 2.7.

In operation, dry particles pass through the first DMA (DMA 1) for size-selection and the first CNC (CPC 1) to determine the particle count. Size-selected particles are then exposed to a controlled relative humidity with respect to water, where humidification is achieved using Perma Pure tubing (model MD-110-48S). The Perma Pure tubing is impermeable to particles, but allows water vapor to be transported from a sheath flow, which is operated at a desired humidity, to the particles. A size distribution is then taken of the “wet” aerosol using the second DMA (DMA 2) and particle counts are determined

using a second CNC (CPC 2). For this analysis, the 50, 100 and 200 nm aerosol particle streams were each exposed to increasing relative humidity and the resulting particle size distribution was monitored.

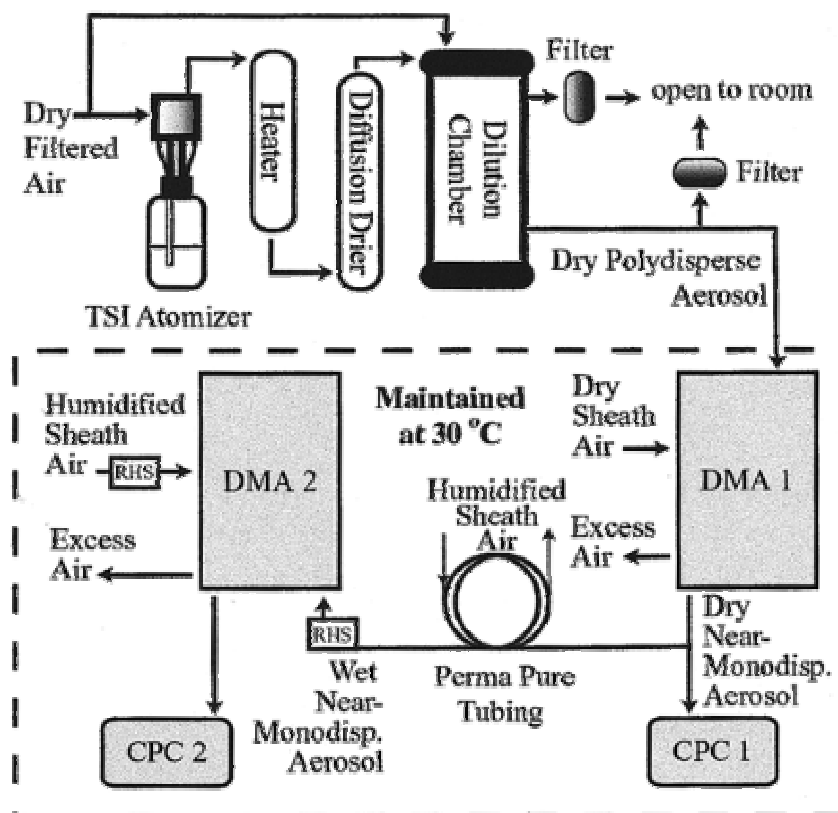


Figure 2.7: Schematic diagram of the humidified tandem differential mobility analyzer (from Prenni et al., 2001).

2.4 Cloud Condensation Nuclei Counter

Cloud condensation nuclei (CCN) are aerosol particles on which water condenses at supersaturations typical of cloud formation. The CCN counter used for these experiments is a modified Mee Industries (Model 130) thermal gradient diffusion chamber. The CCN activity of the mineral dust aerosols treated with H_2SO_4 is used to determine the amount of H_2SO_4 that is deposited on the insoluble particles. This is done

by using the CCN counter to determine the critical water vapor supersaturation (S_{crit}) and using modified Köhler theory for partially soluble spherical particles (see Appendix B) to relate S_{crit} of the mean size particles to the soluble weight percent of H_2SO_4 . S_{crit} is defined here as the water vapor supersaturation at which half of the particles activate as CCN. The soluble fraction of material on the particles can then be used to determine the approximate surface coverage in monolayers of sulfuric acid.

The diffusion chamber of the CCN counter consists of horizontally parallel metal plates that have facing surfaces covered with water-saturated filter paper. A temperature controller regulates the temperature of the top plate so that it is higher than the temperature of the bottom plate, creating supersaturated conditions throughout the chamber. Assuming quiescent conditions throughout the chamber, molecular diffusion prevails, and a linear temperature and nearly parabolic supersaturation profiles develop between the plates with the maximum supersaturation located midway (Nenes et al., 2001). Figure 2.8 shows a horizontal cross section of the CCN counter and Figure 2.9 shows a vertical cross section and supersaturation profile.

The sample is drawn through the chamber at 0.975 lpm for 5 seconds on a 20 second cycle. Particles that activate by taking up water are distinguished from particles that do not activate by illuminating them with a laser source that passes through the center of the chamber. A port in the chamber allows viewing of the illuminated particles with a CCD video microscope. The activated particles that intersect the laser are then counted manually on a video screen. The laser sample volume must be well defined, so that the particle count can be converted to a concentration using a volume correction factor. The volume of the laser imaged was calculated, and then validated by increasing

supersaturation conditions high enough to ensure complete activation of the sample particles. The CCN count at 100% activation, when multiplied by the volume correction factor, should equal the particle concentration simultaneously determined by the CNC. In practice, the concentration of particles that activate as CCN is compared to the total particle concentration from the CNC to yield the activated fraction.

Supersaturation conditions are determined from temperature differences between the plates by calibrating the instrument with monodisperse particles of known critical supersaturation. For these experiments, monodisperse particle streams of $(\text{NH}_4)_2\text{SO}_4$ were generated with mean sizes of 30, 50, 70 and 100 nm. Critical supersaturation conditions for the $(\text{NH}_4)_2\text{SO}_4$ particle streams were determined using Köhler theory. The following exponential formula was determined to relate the temperature difference between the plates to the maximum supersaturation conditions:

$$S_m = 0.0017(\Delta T)^{3.2685} \quad (2.1)$$

where S_m = maximum supersaturation with respect to water and ΔT = temperature difference between the plates.

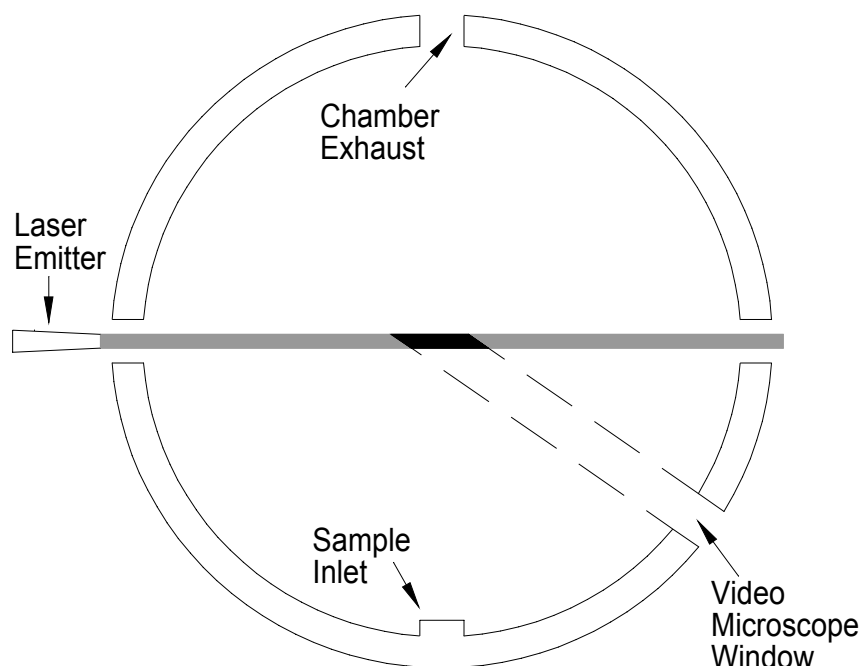


Figure 2.8: Horizontal cross section of the CCN counter.

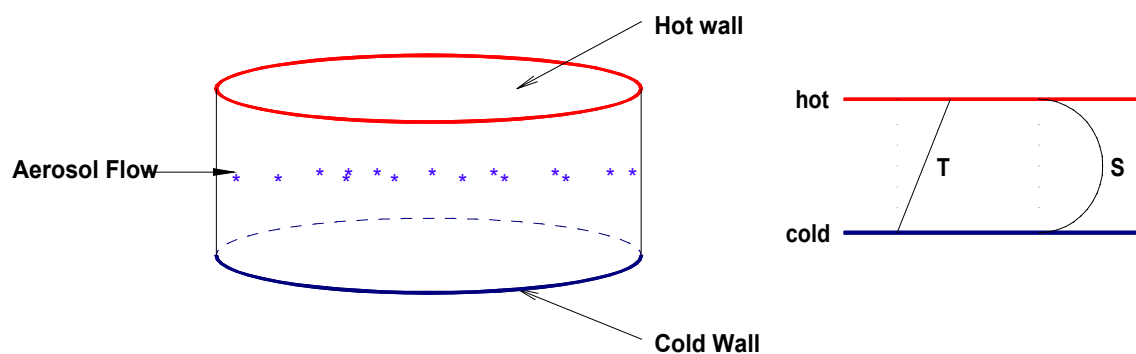


Figure 2.9: Vertical cross section and supersaturation profile for the CCN counter.

2.5 Continuous Flow Diffusion Chamber

The laboratory continuous flow diffusion chamber (CFDC) used in these experiments enables real time measurements of IN concentrations at controlled temperatures and humidities from a continuous stream of aerosol. The laboratory CFDC, along with an airborne CFDC (Rogers et al., 2001), was constructed at the CSU Department of Atmospheric Science through research grants sponsored by the National Science Foundation Division of Atmospheric Sciences. The laboratory CFDC is the same

instrument that was recently used to characterize homogeneous freezing by sulfuric acid/water aerosols (Chen et al., 2000) and is a modified version of the original chamber that is described in detail by Rogers (1988).

The processing section of the chamber consists of two concentric cylinders oriented for vertical air flow through the ~ 1.2 cm gap between the cylinders. The cylinder walls are coated with ice and maintained at different temperatures to produce vapor conditions that are supersaturated with respect to ice within the annular region. For these experiments, the chamber was operated between -45° and -60°C and from ice saturation to water supersaturation. Figure 2.10 is a schematic of the CFDC.

In operation the CFDC walls are first cooled to -25°C using two low temperature bath circulators (Neslab ULT-80) that are filled with a heat transfer fluid (Syltherm XLT, Dow Chemical). The coolant is circulated through copper tubing coils surrounding the outer wall and into a reservoir inside the inner wall. The chamber is then flooded with water, which is allowed to drain, leaving a thin layer (several hundred microns) of ice on each wall. The temperatures controlled by the circulators can then be lowered to create a desired temperature profile in the annular region.

Sample air is introduced into the chamber by first passing through a pre-cooler. The pre-cooler is a $1/2''$ copper tube surrounding a $3/8''$ copper tube that is reduced and welded to $1/4''$ stainless steel tubes at the intake (from aerosol generation) and outlet (to the inlet manifold of the CFDC). Freon is cooled with a compressor and condensing unit and pumped into the gap between the copper tubes. A thermocouple in the flow stream at the outlet of the pre-cooler monitors the temperature of the sample before it enters the CFDC chamber. The pre-cooler cools the sample to as low as -30°C to minimize any

water condensation at the CFDC inlet that might occur from a sharp temperature contrast due to introduction into the cold inlet manifold of the CFDC. This procedure also reduces water vapor density to a value where unresolved supersaturations will not be generated in the temperature and vapor transition region of the CFDC processing section.

The sample air then enters the inlet manifold, which directs the sample into the center of the annulus and between two sheath flows of particle-free air. Typically, the sample air is 10% of the total flow. With a chamber length of 150 cm and a total flow rate of 12 lpm, the sample residence time for these experiments is about 11 seconds.

Figure 2.11 shows an example of temperature, humidity and velocity profiles inside the CFDC assuming steady-state conditions. Linear temperature and vapor pressure profiles are established within a short distance inside the CFDC and supersaturations are a consequence of the exponential variation of saturation vapor pressure. The chamber flow velocity is skewed slightly towards the cold wall because of the buoyant circulation produced from the density gradient that results from temperature differences. A critical flow rate is calculated and maintained to assure that reverse thermal flow does not occur along the warm surface. Specifying equal sheath air mass fluxes on either side of the aerosol lamina also displaces the aerosol lamina toward the cold side. This is because the sheath air near the cold wall is denser than the sheath air near the warm wall. Aerosol position and exposure conditions are calculated based on the simplified equations of Rogers (1988).

At the chamber exit all flow passes through an optical particle counter (OPC, Climet Model 7350A). Ice crystals that are nucleated in the CFDC grow to relatively large sizes compared to unactivated aerosol particles. All particles produce voltage

pulses in the OPC that are binned into 255 channels and counted by a multichannel analyzer (MCA) PC Card. The OPC has two gain settings for detecting pulses, referred to as high gain and low gain. Size resolution in the OPC is a function of particle velocity and approximate size has previously been calibrated for spherical particles in this OPC using nearly monodisperse polystyrene latex particles and oleic acid particles. For the conditions in these experiments, the calibration suggests that setting the OPC to high gain detects the smaller particles above $0.4\text{ }\mu\text{m}$, with an upper end that is ill-defined, but approximately $5\text{ }\mu\text{m}$. Likewise, the lower end for low gain is ill-defined, but the low gain setting detects particles from approximately $2.5\text{ }\mu\text{m}$ up to about $19\text{ }\mu\text{m}$. For the respective gain settings, the larger particles accumulate in the higher channel bins and the smaller particles in the lower bins.

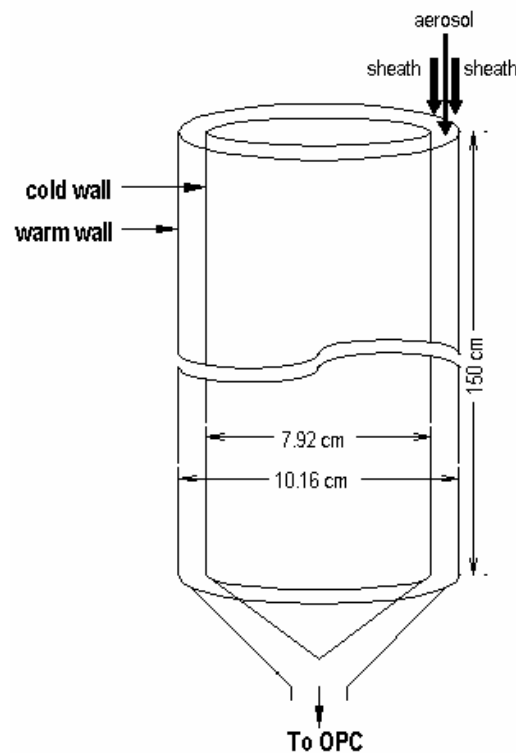


Figure 2.10: Schematic of the CFDC.

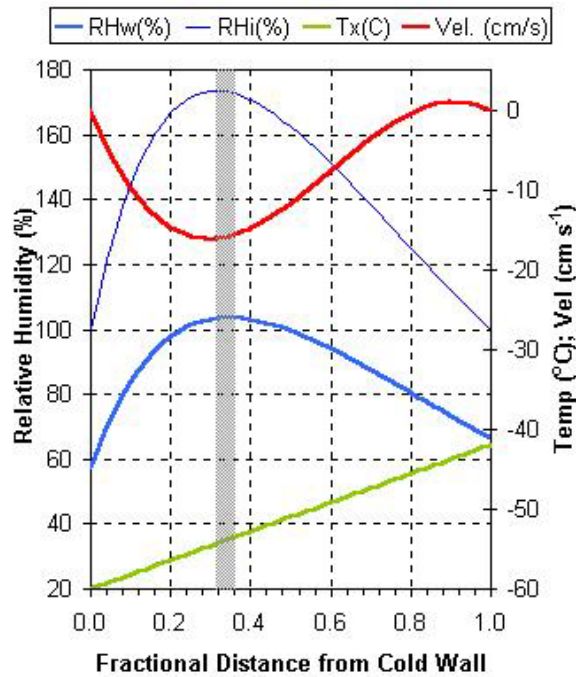


Figure 2.11: Steady-state temperature, supersaturation and velocity profile inside the CFDC.

2.6 Data Acquisition

Real time data acquisition for the CFDC is done using the National Instrument's (NI) LabVIEW graphical development environment integrated with NI Fieldpoint modular distributed I/O systems. LabVIEW programming was done by Original Code Consulting of Boulder, CO.

Temperature data are recorded from eight type-T thermocouples (copper-constantan) located inside the CFDC. Total and sheath flow rates are recorded from mass airflow sensors and sample flow is determined as the difference of these flows. These data are used by the program to calculate temperature and humidity conditions experienced by the sample (see Rogers, 1988). The critical flow rate is also calculated so the program can signal when the critical flow has been reached.

The two outputs from the OPC, high gain and low gain, are sent individually to the program. The MCA PC card reads digitized voltage signals from the OPC and sorts them into the 255 bins corresponding to particle diameters. Size distributions are measured as the particles exit the CFDC and data are recorded for particles larger than a specified cutoff size. The cutoff size used for these studies is 1.3 micrometers, or channel 39 in high gain. This cutoff size was determined to eliminate counting haze particles as ice particles because it is significantly larger than the expected size for hygroscopic growth below water saturation (Prenni et al., 2001). From these data, the program calculates and records IN/cm^3 .

Data are also recorded and displayed from the CNC. Graphical and channel data are displayed in real time, and a data exporter can be used for viewing binary data or creating ASCII output files. Figure 2.12 is an example of the data display mode for the CFDC data acquisition program.

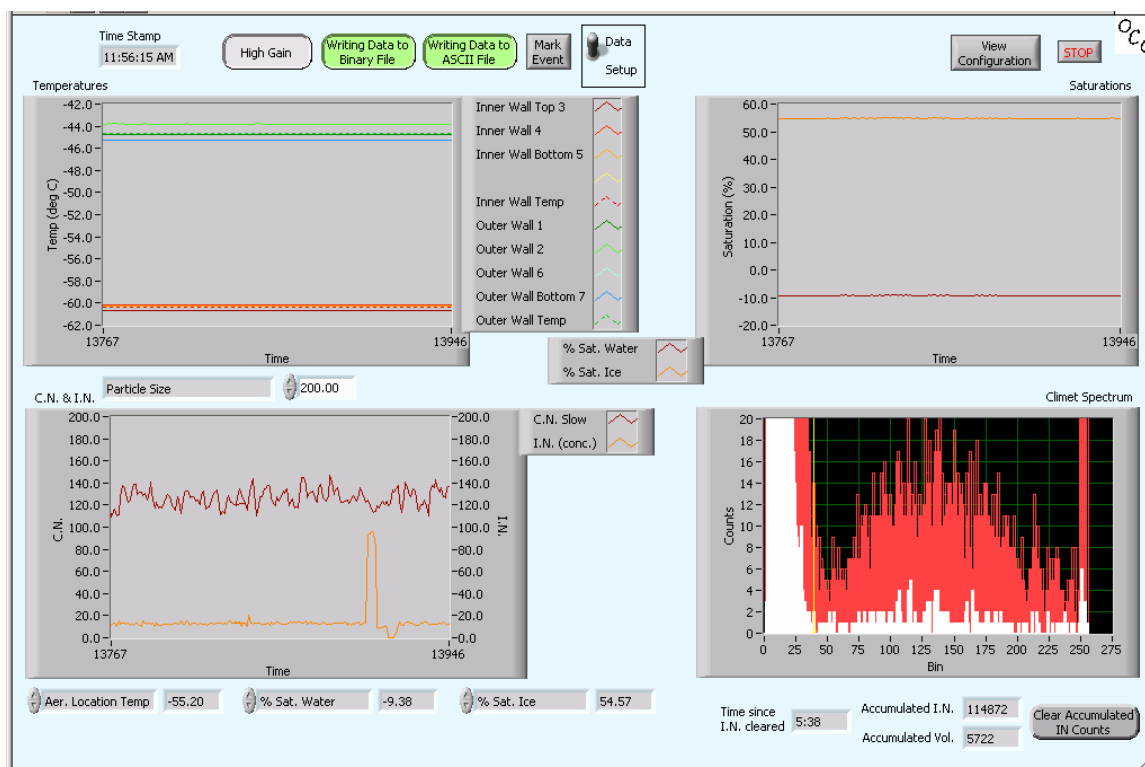


Figure 2.12: The data display mode of the CFDC data acquisition program developed by Original Code Consulting of Boulder, Co. The upper left graph is the temperature profile in the CFDC, the upper right is the ice and water supersaturation conditions, the lower left is the CN profile and the IN profile, and the lower right is the MCA particle size spectra (the darker color is a five second sum and the white is a 1 second value).

3. Experimental Results

3.1 Sample Information

3.1.1 Commercially produced nanoparticles

Commercially available metal oxide and alumina-silicate particles were obtained from the NanoProducts corporation (<http://www.nanoproducts.com>) in Longmont, CO. The sample preparation, as described by NanoProducts, begins by preparing a liquid solution from carefully chosen precursors corresponding to the stoichiometry of the

metals desired in the final powders. The liquid solution is atomized into an ultrafine mist with a reactant gas (oxygen) and processed in a two stage thermal process in the presence of plasma, which is essentially an electrically charged cloud of ionized gas. This environment leads to the formation of an elemental vapor with a high peak plasma temperature (exceeding 3000°C), which is then cooled leading to nucleation of nanoscale particles. The particle-containing gas stream is quenched at near sonic velocities using a Joule-Thompson expansion nozzle. This sonic quenching reduces collisions between the particles and produces free-flowing nanopowders that are then collected. Manufacturer estimates of the size characteristics for the nanopowders purchased are indicated in table 3.1. For this work, the nominal sizes as shown in Table 3.1 are not assumed, since we select a nearly monodisperse, well-characterized mobility size from the overall suspended sample via the DMA.

Figure 3.1 shows number size distributions of the samples that were measured using a scanning DMA coupled with a CPC. The distribution of the aluminum oxide and iron-oxide particles are shaped similarly and both have modes at about 20 nm. The alumina-silicate distribution was almost constant up through about 80 nm, and then the number concentrations started dropping off at the larger sizes.

Table 3.1: Descriptions of nanoscale powder products as provided by the NanoProducts Corporation in Longmont, CO.

Powder Type	BET Specitic Surface Area (m²/g)	Calculated BET Equivalent Spherical Diameter (nm)	XRD CrystalliteSize (nm)
Aluminum Oxide (Al ₂ O ₃)	26.0	57.7	13-19
Aluminum Silicate (72% Al ₂ O ₃ : 28% SiO ₂)	24.3	78.1	Amorphous
Iron Oxide (Fe ₂ O ₃)	12.9	88.8	37-39

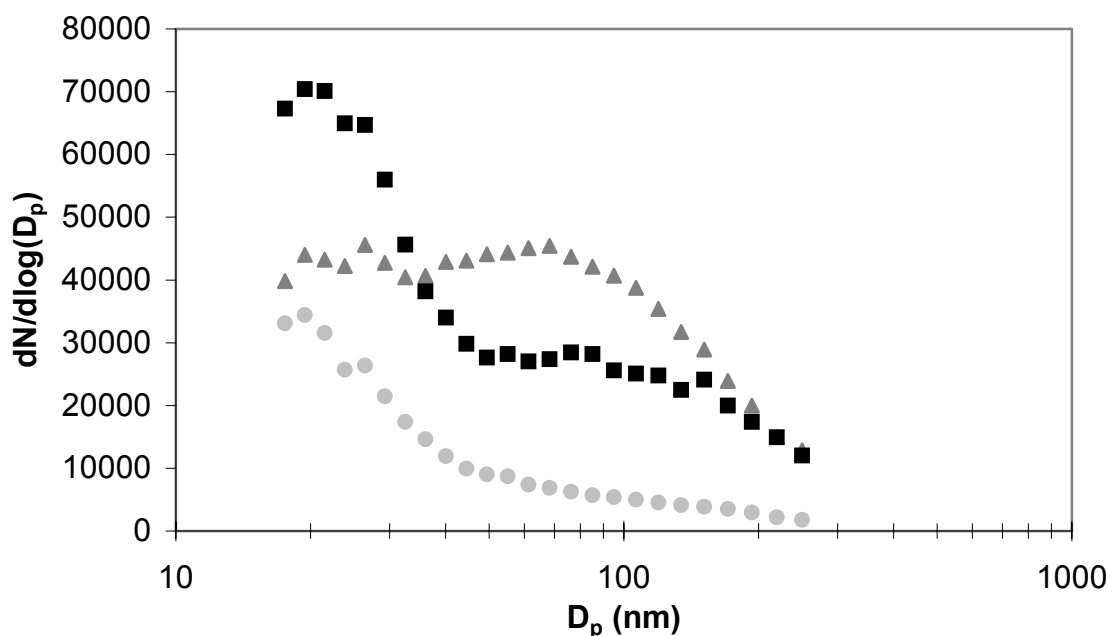


Figure 3.1: Number size distributions for aluminum oxide (squares), alumina-silicate (triangles) and iron oxide (circles) as determined at CSU using a scanning DMA coupled with a CPC.

3.1.2 Asian Mineral Dust Sample

A sample of Asian mineral dust was collected and prepared for analysis by Masataka Nishikawa of the National Institute for Environmental Studies in Japan. Dr. Nishikawa provided the following sampling and preparation description.

The original surface soil was sampled near Shapotou, which is located on the southeastern fringe of the Tengger Desert in China (40N-116E). This is one of the larger regions of origin for the “Kosa” dust storms that occur in springtime. The original dust sample was roughly sieved from over 20 kg of surface soil. The sample was then sieved by a wind tunnel system (16m-length) with a controlled wind speed of 2 m/s, which should result in particle sizes classified under 10 μ m. This sample (about 3g) was further refined by a small impactor system after transport back to Japan.

Table 3.2 shows the chemical constituents of the resulting Kosa sample, as determined by Dr. Nishikawa, using ICP analysis with acid digestion. Figure 3.2 shows the number distribution for the sample sizes. The distribution above $0.3\ \mu\text{m}$ was measured in Japan by a particle property analyzer (SA-CP4L, Shimadzu Co., Japan) that uses a centrifugal method for depositing particles suspended in water and analyzes concentration optically. It is possible that this method did not provide adequate information for particles smaller than about $1\ \mu\text{m}$. The distribution below $0.3\ \mu\text{m}$ was measured by atomizing water suspensions of the dust, removing particles larger than $1\ \mu\text{m}$ using two cylindrical jet impactors in series (see Rogers et al., 2001), and flowing the particles through a scanning DMA coupled with a CNC. The size distribution clearly shows two modes, one in the larger size regime and one in the smaller size regime.

Table 3.2: Chemical constituents of the sample as determined by ICP analysis with acid digestion ($\text{HNO}_3 + \text{HClO}_4 + \text{HF}$) treatment. Si was not determined, but can be assumed to be about 28%. Data provided by Dr. Masataka Nishikawa, National Institute for Environmental Studies, Japan.

Element	%	Element	$\mu\text{g/g}$
Ca	5.59	Mn	621
Al	5.63	Ba	519
Fe	2.89	Sr	252
K	1.8	Zn	105
Mg	1.48	V	81.6
Na	1.27	La	36.1
Ti	0.4	Cu	34.9

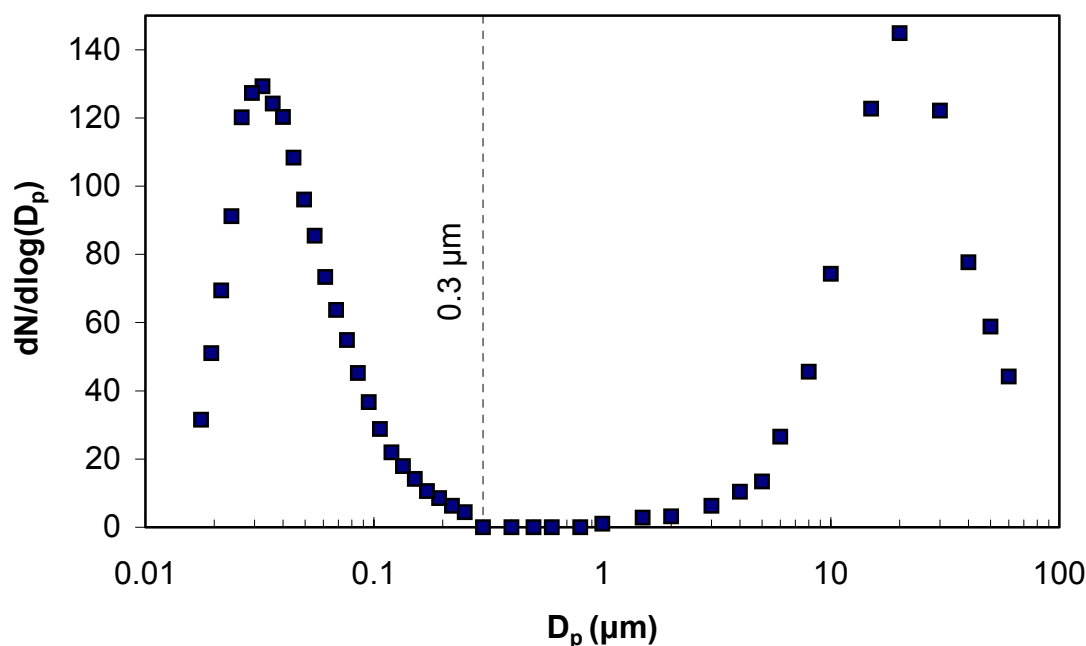


Figure 3.2: Number size distribution of the mineral dust sample. The distribution above $0.3 \mu\text{m}$ (300 nm) was determined Dr. Masataka Nishikawa, National Institute for Environmental Studies, Japan. Size distribution below $0.3 \mu\text{m}$ was determined at CSU using a scanning DMA coupled with a CNC.

3.2 HTDMA water uptake results

The water uptake for these particles was first characterized for conditions below water saturation using the humidified tandem differential mobility analyzer (HTDMA) described in section 2.3. HTDMA data were collected for this study using methods similar to those described in Prenni et al. (2001).

The data indicated no water uptake on any of the manufactured aluminum oxide, alumina-silicate or iron oxide particles below 93% relative humidity, which is the approximate upper limit for the method. The water uptake results for the Asian dust were very different as depicted in Figure 3.3. The data are presented as the hygroscopic growth factor on an RH_w scale. The hygroscopic growth factor ($D_{\text{wet}}/D_{\text{dry}}$) gives an

indication of the amount of water condensed on the particles where D_{wet} is the diameter of the particles after being exposed to the indicated humidity conditions, and D_{dry} is the dry particle diameter. For the 50, 100 and 200 nm sizes generated, all particles started to uptake water at about 60 %RH_w. Above 60 %RH_w, the smaller 50 and 100 nm particles grow to relatively larger sizes than the 200 nm particles. This seems to indicate that all of the particles contain some soluble material, and there is more soluble material in the smaller particles than in the larger ones. This provides some evidence that the different size modes possess different chemical constituents. This matter may be elucidated in the near future using electron microscopy analyses on collections of size-selected particles.

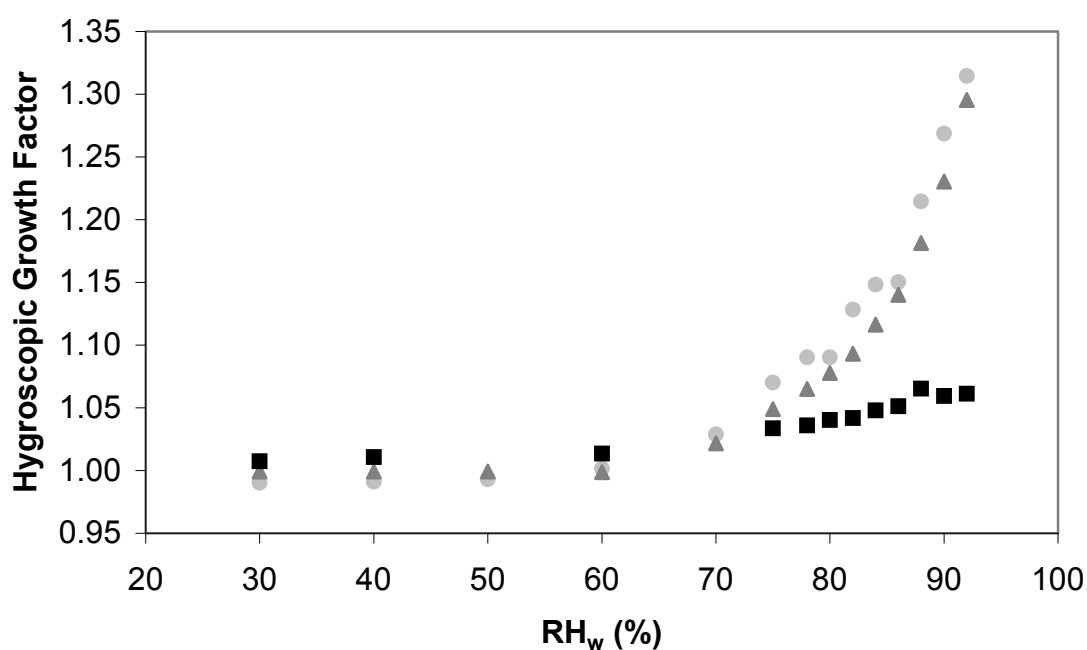


Figure 3.3: HTDMA water uptake results for 50 nm (circles) 100 nm (triangles) and 200 nm (squares) Asian dust particles.

3.3 CCN Results

CCN activity was determined using the CCN counter described in section 2.3. Particle streams are generated from 1 weight % suspensions of aluminum oxide, alumina-silicate or iron oxide particles. After the particle stream is dried it passes through the DMA where nearly monodisperse streams of 100 and 200 nm particles are selected. The 50 nm particles could not be generated in sufficient concentrations to be reliably measured by the CCN counter after activation. After size selection, particles pass through the sulfuric acid coating system described in section 2.1.3. The heated reservoir for the H_2SO_4 is maintained at 95°C while $\text{N}_2(\text{g})$ flows over the acid drop at 0.1 lpm. The total aerosol flow through the tube furnace is 2.0 lpm, with 1.0 lpm exiting the DMA, 0.1 lpm from the $\text{N}_2(\text{g})$ (industrial grade, General Air Co.) laden with H_2SO_4 , and 0.9 lpm from diluted, dry purified air. The particle stream, treated with H_2SO_4 , is then routed simultaneously through the CNC and the CCN counter. Alternately, the size selected particle stream bypasses the sulfuric acid coating system and enters the CNC and the CCN counter for analysis of untreated particles.

The percent of the particles activated as CCN is determined by incrementally increasing the difference between the warm and the cold plates (ΔT) in the instrument chamber in steps of 0.1°C . The increasing temperature difference corresponds to increasing supersaturation with respect to water (S_w), as indicated previously in equation 2.1. The percent activation is determined by comparison of the number of activated particles to the total particle population as indicated by the CNC. Data are recorded starting at 0% activation and proceeds until about 100% of the sample has activated as cloud drops.

The experimentally determined CCN activation conditions are used to estimate the soluble weight percentage of H_2SO_4 on the treated mineral particles. As described in appendix B, Köhler theory for partially soluble spherical particles relates S_{crit} to the amount of soluble material on the particle. The amount of soluble material on the particle can be used to estimate the number of monolayers of H_2SO_4 assuming uniform coverage around a spherical particle, and using the estimation that a simple, close packed sphere model for H_2SO_4 gives about 4.5×10^{14} molecules/cm² (Wyslouzil et al., 1994).

3.3.1 Aluminum oxide, alumina-silicate and iron oxide

The results of the CCN behavior of 100 and 200 nm treated and untreated aluminum oxide particles are shown in Figures 3.4 (a) and (b), for alumina-silicate in Figures 3.5 (a) and (b) and for iron oxide in Figures 3.6 (a) and (b). Data are presented as the CCN active fraction (CCN/CN) as a function of water vapor supersaturation. The plots include exponential line fits to the data from which S_{crit} can be estimated as the point at which 50% of the particles have activated as CCN. The exponential fit is not realistic for describing all of the data but is suitable for extracting the 50% points. Dashed lines indicate the S_{crit} values for the various compositions and sizes of the treated particles. The CCN counter was operated at a range of supersaturations from about 0.1% to over 1.0% supersaturation with respect to water.

There was not a marked difference in the behavior of particles with different mineral compositions. Both 100 and 200 nm particles showed modest CCN activity (greater than for an insoluble, but completely wettable, nucleus) while uncoated, and enhanced activity when exposed to H_2SO_4 vapor. The weight % of sulfuric acid deposited on the treated mineral particles, estimated using S_{crit} and Köhler theory for

partially soluble spheres, is indicated in Table 3.3. An approximation for the corresponding number of monolayers of acid is inferred, assuming spherical particles with uniform coverage. Smaller particles contained higher weight percent H_2SO_4 and larger particles lower weight percent. The treatments led to an inferred range of acid coatings from 1.11 to 2.20 monolayers with an average of 1.61.

The CCN activity on the untreated particles corresponds to an estimated range of 0.008-0.017% soluble matter on the 100 nm particles, assuming sulfuric acid as the solute, and a range of 0.002-0.005% soluble matter on the 200 nm particles. The HTDMA data indicated no water uptake on any of the particles below 93% relative humidity. The nature of this soluble matter is difficult to determine, but the HTDMA data suggest that it is not a simple electrolyte, but rather a material with a high deliquescence relative humidity. This may be volatile organic by-products from the precursor solutions re-condensed during the production of the mineral oxides.

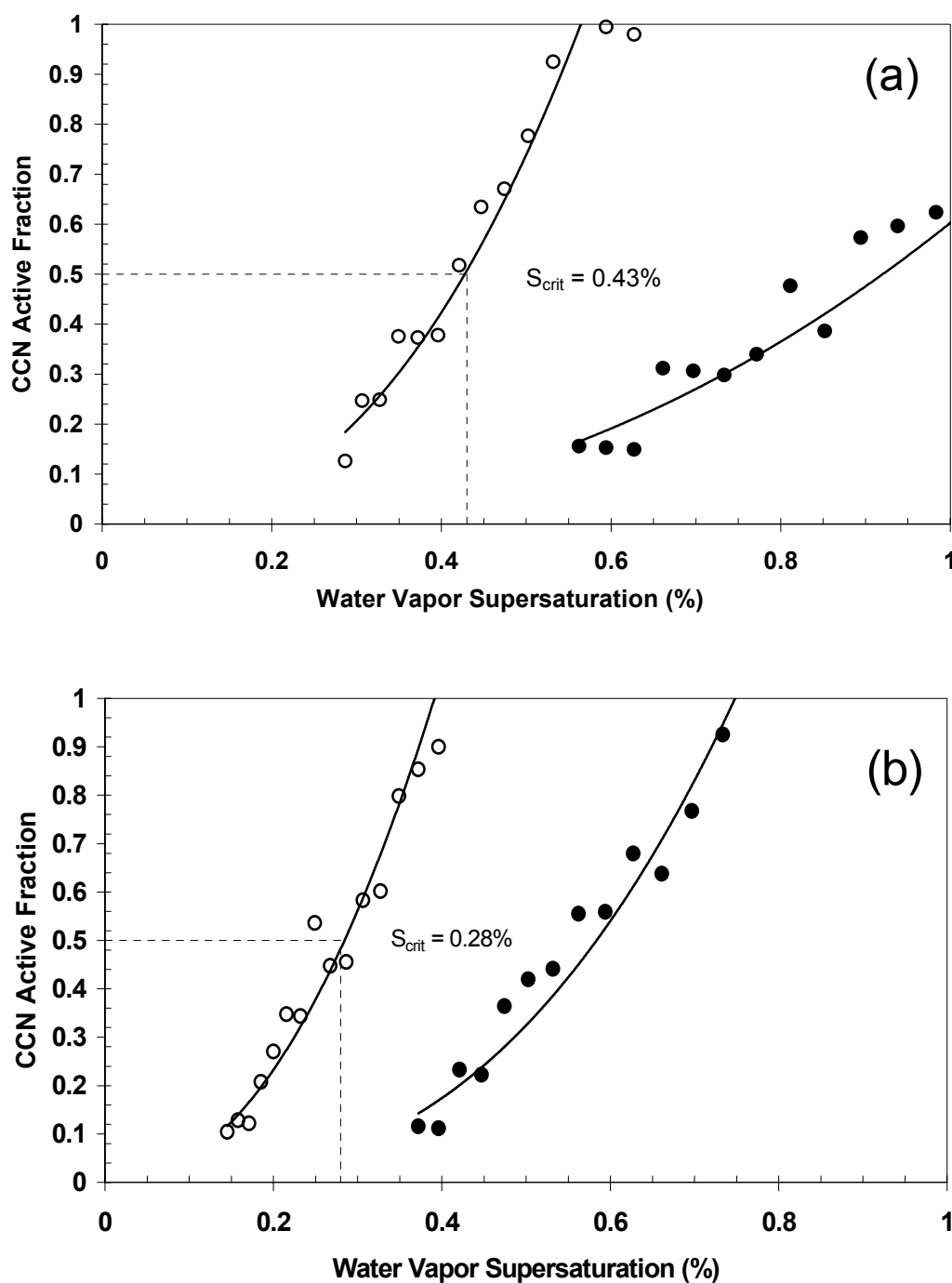


Figure 3.4: Measured CCN activity for 100 nm (a) and 200 nm (b) aluminum oxide particles. Symbols indicate cases of untreated aluminum oxide particles (closed circles) and aluminum oxide particles treated with H_2SO_4 (open circles). The lines indicate exponential fits to the data, and S_{crit} is the point on the line where 50% of the particles have activated as CCN.

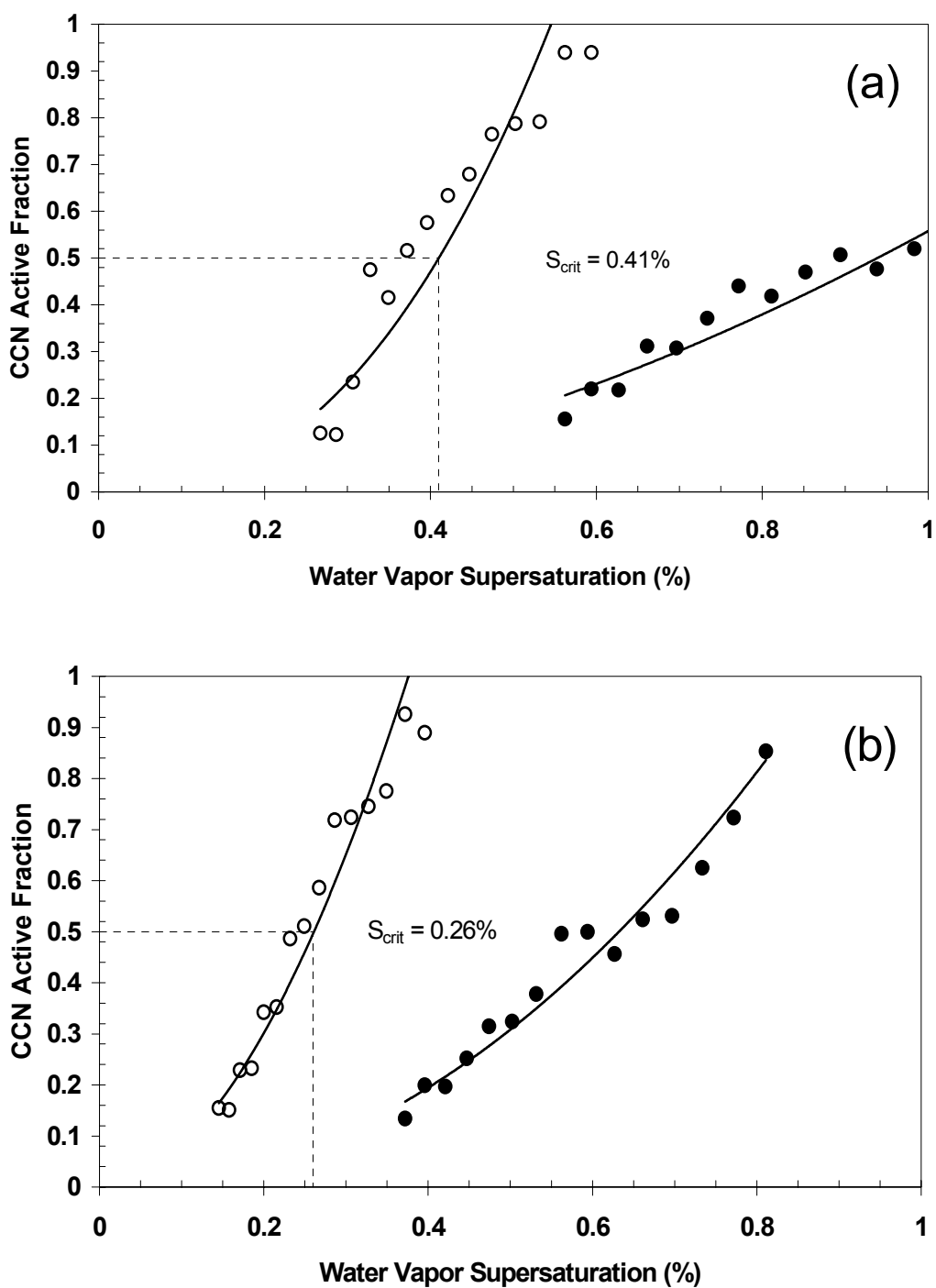


Figure 3.5: As in Figure 3.2, but for 100 (a) and 200 (b) nm alumina-silicate particles.

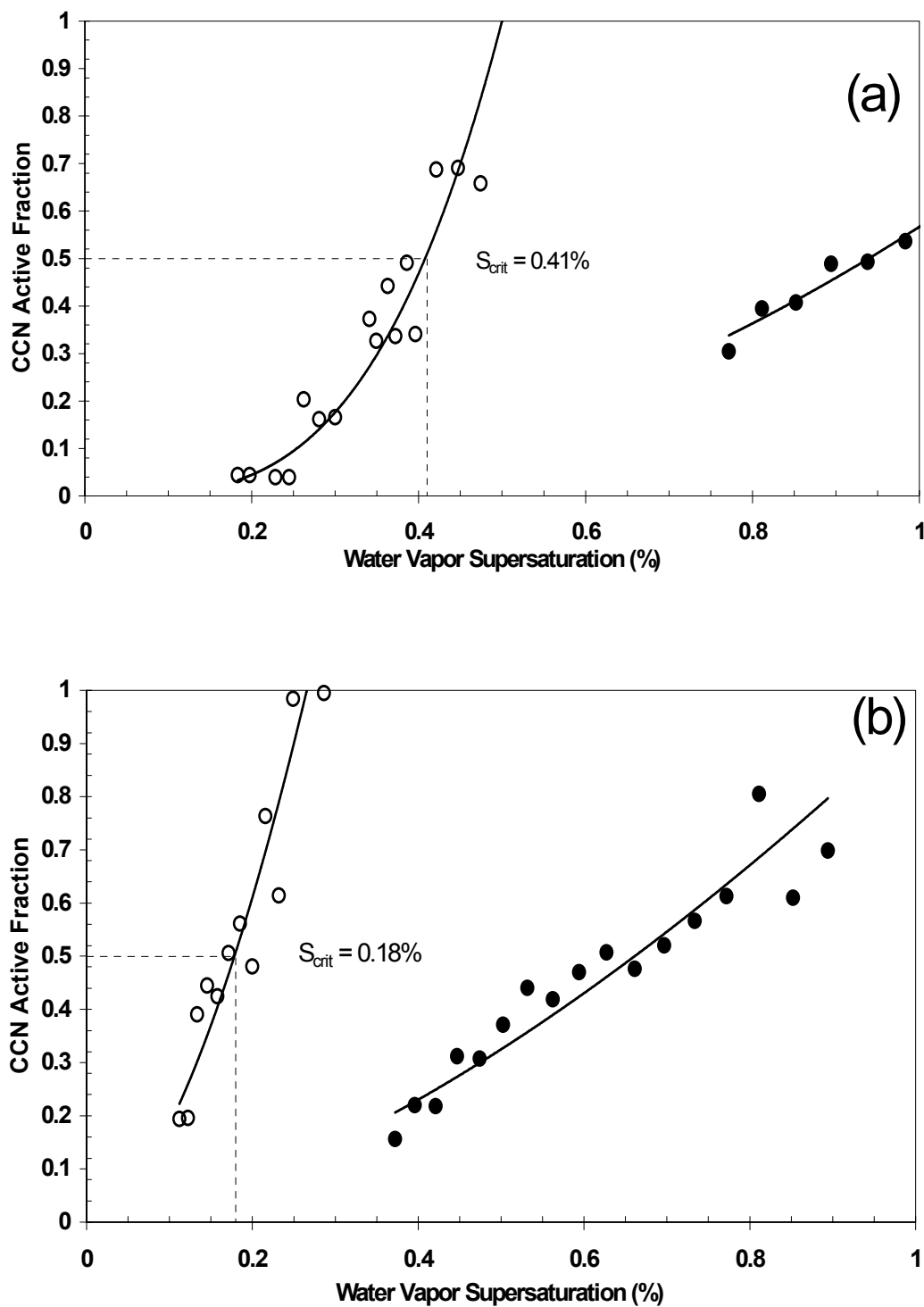


Figure 3.6: As in Figure 3.2, but for 100 (a) and 200 (b) nm iron oxide particles.

Table 3.3: The weight % of sulfuric acid deposited on the mineral particles determined using S_{crit} and Köhler theory for partially soluble spheres. The corresponding number of monolayers of acid is included in parenthesis where spherical particles are assumed with uniform coverage.

Particle Diameter (nm)	Weight % H_2SO_4 (<i>monolayers H_2SO_4</i>)		
	Al_2O_3	$3Al_2O_3:2SiO_2$	Fe_2O_3
100	0.05 (1.43)	0.08 (1.57)	0.05 (1.68)
200	0.03 (1.68)	0.03 (1.11)	0.03 (2.20)

3.4 CFDC Results

Ice nucleation activity was determined using the CFDC as described in section 2.4. Untreated and treated particle streams of 50, 100 and 200 nm aluminum oxide, alumina-silicate and iron oxide particles were generated in the same manner as described in section 3.2 for the CCN analysis. Ice nucleation activity was also determined for the reference mineral dust sample described in section 3.1. The particle stream, either untreated or treated with H_2SO_4 , was routed simultaneously through the CNC and the CFDC.

Ice activation for these experiments is determined as the temperature and RH_i conditions at which 1.0% of the particles activate as ice nuclei. For these experiments, the ice coated chamber walls are first set to the selected temperature for analysis (-45, -50, -55, or -60°C). Changing the temperatures of both chamber walls in opposite directions allows the sample temperature to be maintained while increasing the RH_i . The RH_i is increased in increments of about 5.0% ($\sim 3\%RH_w$), and ice activation is recorded until more than 1.0% of the particles have activated as ice nuclei. The exact RH_i for 1.0% particle activation is determined by interpolating between the nearest points at a given temperature. The contributions of larger, multiply charged, particles exiting the

DMA in monodisperse flow, and the resulting effects of on the initiation of ice nucleation are discussed in Appendix A.3. Some of the other uncertainties in these calculations are discussed in Appendix C.

For the mineral dust particles that are treated with H_2SO_4 , a comparison is made to the homogeneous freezing of the liquid components of the particles assuming the sulfuric acid in particles is distributed as a perfect spherical coating on the mineral dust cores. For these calculations, the dilution of the acid coating was determined assuming equilibrium conditions with the plotted RH. The procedure for determining the dilution of the acid involves using Köhler theory to relate the relative humidity conditions to the droplet size as described in appendix B. Homogeneous freezing conditions for this solution can then be calculated using parameterizations of the homogeneous freezing of $\text{H}_2\text{SO}_4/\text{H}_2\text{O}$ particles (Chen et al., 2000).

3.4.1 Aluminum Oxide

The conditions for freezing of 1.0% of the untreated 50, 100 and 200 nm aluminum oxide particles are shown in Figure 3.7 as a function of RH_i and temperature, with error bars representing a 95% confidence interval (see Appendix C). Included for comparison are homogeneous freezing results for pure sulfuric acid particles of the same sizes as the mineral dust particles, based upon data from Chen et al. (2000). The aluminum oxide particles did not require soluble coatings to activate as IN, and in fact behaved as fairly efficient IN without coatings. A general size effect is apparent, as the larger particles nucleate at lower relative humidity conditions than the smaller particles, and this size separation is more evident at colder temperatures. The 50 nm particles activated below water saturation at all temperatures except -45°C , but overall they did

not appear to induce freezing at warmer temperatures or lower RH_i than required for homogeneous nucleation of 50 nm H_2SO_4 particles. The 100 and 200 nm aluminum oxide particles intersect lines indicating homogeneous activity of similarly size sulfate particles at $-45^\circ C$, but at colder temperatures initiate ice formation at lower relative humidity conditions than where homogeneous freezing nucleation occurs. The 200 nm particles exhibited the best ice formation capability at temperatures below $-45^\circ C$. The slope of the relationship between RH_i and temperature for initiation of freezing appears to have the opposite sign as that for homogeneous freezing nucleation of 200 nm sulfuric acid particles.

The freezing conditions for 1.0% of the treated 50, 100 and 200 nm aluminum oxide particles are shown in Figure 3.8 as a function of RH_i and temperature with error bars again representing a 95% confidence interval. Included to help distinguish heterogeneous nucleation from homogeneous freezing of the liquid components of the particles are predictions of the conditions required for homogeneous freezing of the sulfuric acid coating, distributed as a perfect spherical coating on the aluminum oxide cores. Again, the larger particles nucleate at lower relative humidity conditions than the smaller particles. The 50 nm treated aluminum oxide particles do not appear to enhance nucleation when compared to the predicted conditions for homogeneous freezing of sulfuric acid coatings. The 100 nm coated particles indicate a modest heterogeneous freezing nucleation effect. The 200 nm mixed particles indicate a stronger heterogeneous effect by exhibiting nucleation at much lower relative humidity conditions than those required for homogeneous freezing of the liquid part of the particles.

The ice nucleation behaviors of the treated and untreated particles appear to be comparable at all conditions except -60°C . Using the hypothesis test described in appendix C, along with a pooled standard deviation encompassing the standard deviations in RH_i conditions for all replicates in this study, the conditions for 1.0% ice nucleation at -60°C are significantly different with at least 99.5% confidence levels. The ice nucleation conditions were statistically similar at all other temperatures.

3.4.2 Alumina-silicate

The conditions for freezing of 1.0% of the untreated 50, 100 and 200 nm alumina-silicate particles are shown in Figure 3.9 as a function of RH_i and temperature with error bars again representing 95% confidence intervals. Included for comparison are the same homogeneous freezing results for pure sulfuric acid particles shown on Figure 3.7.

Similar to the aluminum oxide particles, alumina-silicate did not require soluble coatings to activate as IN, and the larger particles nucleate at lower relative humidity conditions than the smaller particles with a more profound size effect at colder temperatures. At -45°C all particle sizes activated under similar conditions as the corresponding homogeneous freezing conditions of pure acid particles, but at temperatures colder than -45°C the activation conditions deviate from the homogeneous activation conditions. The 100 and 200 nm particle conditions deviate from homogeneous conditions very sharply and, similar to the 200 nm aluminum oxide particles, the activation conditions have the opposite slope as those for the pure acid particles.

The conditions for freezing of 1.0% of the 50, 100 and 200 nm alumina-silicate particles treated with sulfuric acid are shown in Figure 3.10 as a function of RH_i and temperature with 95% confidence error bars. As in Figure 3.8, included for comparison

are homogeneous freezing predictions for the sulfuric acid in the particles distributed as a perfect spherical coating on the alumina-silicate cores. Again, larger particles nucleate at lower relative humidity conditions than the smaller particles at all temperatures. There was some inhibition in the activation of the 50 nm particles, with most of them activating as ice nuclei at or above water saturation. Otherwise, the trends in freezing behavior for the treated alumina-silicate particles were similar to those of the treated aluminum oxide particles, with enhanced nucleation over pure H_2SO_4 particles only clearly observed for the 200 nm core particles.

In contrast to the findings for aluminum oxide particles, the ice nucleation behavior of the untreated and treated alumina-silicate particles is very different. The 50 nm untreated particles activated well below water saturation at most temperatures, while the treated 50 nm particles activated primarily above water saturation. Again, considering the hypothesis test described in appendix C, the conditions for nucleation of the 100 and 200 nm particles are different with a confidence level of 99.9% when temperatures reach -55 and -60°C .

3.4.3 Iron Oxide

The conditions for freezing of 1.0% of the untreated 50, 100 and 200 nm iron oxide particles are shown in Figure 3.11 as a function of RH_i and temperature with 95% confidence error bars. Included again for comparison are the same homogeneous freezing conditions for pure sulfuric acid particles as shown in Figure 3.7. Iron oxide also did not require soluble coatings to activate as IN, but were not quite as efficient as the other mineral oxides in this study. Nevertheless, 100 and 200 nm iron oxide particles did show enhanced activity over homogeneous freezing of similarly sized H_2SO_4

particles. The 50 nm particles activated at similar or higher RH_i than their homogeneous counterparts.

The conditions for freezing of 1.0% of the 50, 100 and 200 nm iron oxide particles treated with sulfuric acid are shown in Figure 3.12 as a function of RH_i and temperature with 95% confidence error bars. Included for comparison are predicted conditions for homogeneous freezing of the sulfuric acid coatings. All sizes (except the 50 nm particles at -60°C) had enhanced nucleation compared to the conditions predicted to be required to homogeneously freeze the diluted H_2SO_4 on the insoluble cores. The treated iron oxide particles, though not activating at the exact same conditions, have similar trends in the RH_i -temperature relationship as found for the treated aluminum oxide and alumina-silicate particles.

The ice nucleation behavior of the untreated and treated iron oxide particles is very similar. Using the hypothesis test in appendix C, again with a pooled standard deviation that encompasses all ice formation measurements in this study, the conditions for activation do not appear to be statistically different at higher temperatures, but the treated 50, 100 and 200 nm particles in this case activate at about 6 % RH_i lower than the untreated particles at -55 indicating differences at confidence levels between 95 and 97.5%. The 200 nm particle activation at -60°C was statistically different with a 99% confidence level.

3.4.4 Asian mineral dust sample

The conditions for freezing of 1.0% of the 50, 100 and 200 nm Asian mineral dust particles are shown in Figure 3.13 as a function of RH_i and temperature along with the predicted conditions required for homogeneous freezing of pure sulfuric acid particles of

the same sizes. Error bars again indicated 95% confidence intervals. The 50 nm dust particles activated near or above water saturation at all temperatures, which was higher than the relative humidity conditions required for homogeneous nucleation of 50 nm sulfuric acid particles. The 100 nm Asian dust particles required decreased RH_i at lower temperature for the onset of freezing, in contrast to the relationship expected for pure acid particles, indicating more effective ice nucleation as compared to homogeneous freezing of pure sulfate particles at -55°C . There appeared to be a more profound size separation between the activation conditions for the 100 and 200 nm Asian dust particles than that observed in the relatively pure single-component mineral dust particles. The 200 nm particles activated at almost constant RH_i conditions across the temperature range, and at significantly lower relative humidity conditions than similarly sized homogeneous particles. The RH_i for ice nucleation of the 200 nm particles was the lowest of any aerosol tested in this study.

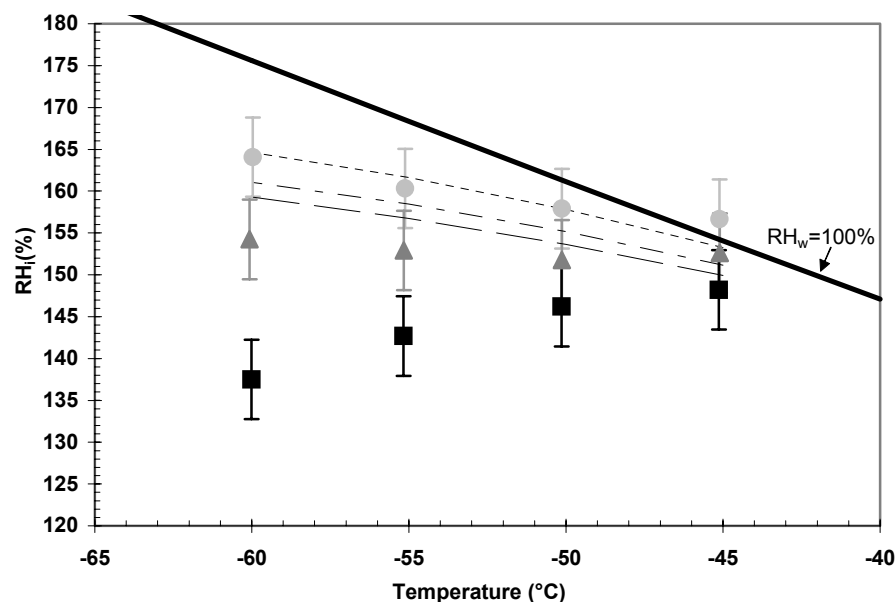


Figure 3.7: Average CFDC conditions for the formation of ice on 1% of aluminum oxide particles. Data are presented for 50 nm (circles), 100 nm (triangles), and 200 nm (squares) aerosol particles. Error bars indicate a 95% confidence level (see appendix C). For comparison homogeneous freezing for pure H_2SO_4 particles are included for 50 nm (dotted), 100 nm (dash-dot) and 200 nm (dashed) conditions based on observations from Chen et al. (2000). Also included is a line for $RH_w = 100\%$.

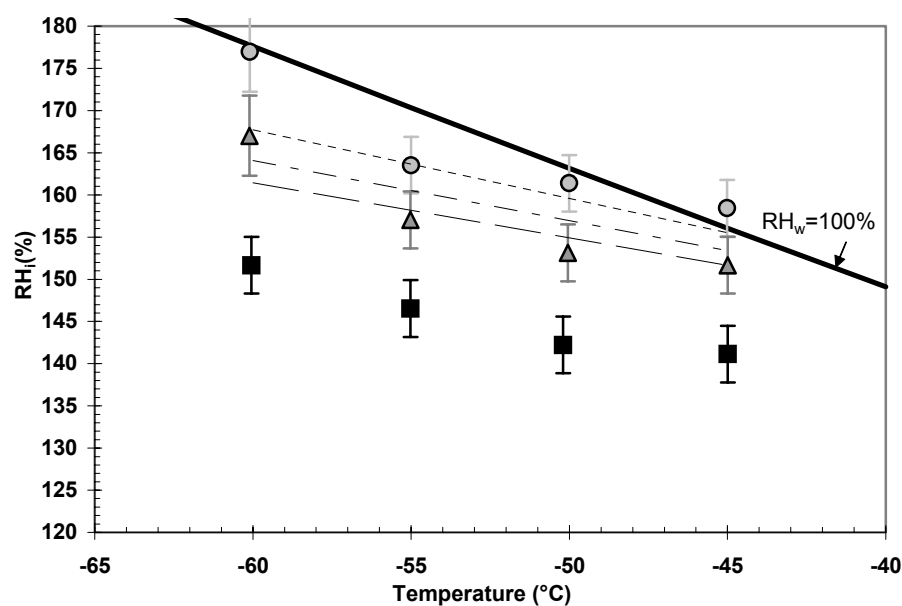


Figure 3.8: Average CFDC conditions for the formation of ice on 1% of aluminum oxide particles treated with H_2SO_4 . Data are presented for 50 nm (circles), 100 nm (triangles), and 200 nm (squares) aerosol particles. Error bars indicate a 95% confidence level (see appendix C). Lines indicate predictions for the conditions required for homogeneous freezing of the H_2SO_4 coatings on the 50 nm (dotted), 100 nm (dash-dot) and 200 nm (dashed) core particles, based on Chen et al. (2000). Also included is a line for $RH_w = 100\%$.

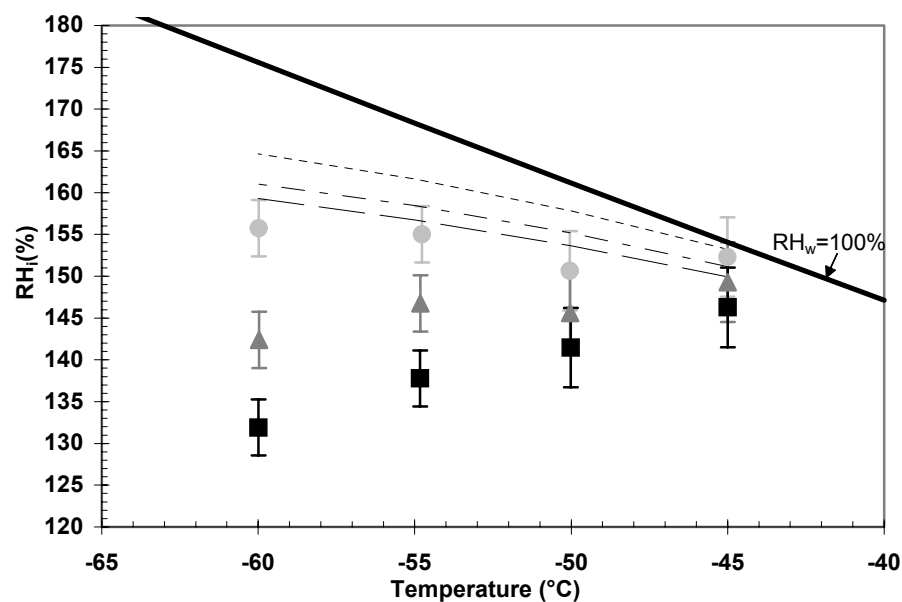


Figure 3.9: As in Figure 3.5, but for CFDC conditions for the formation of ice on 1% of alumina-silicate particles.

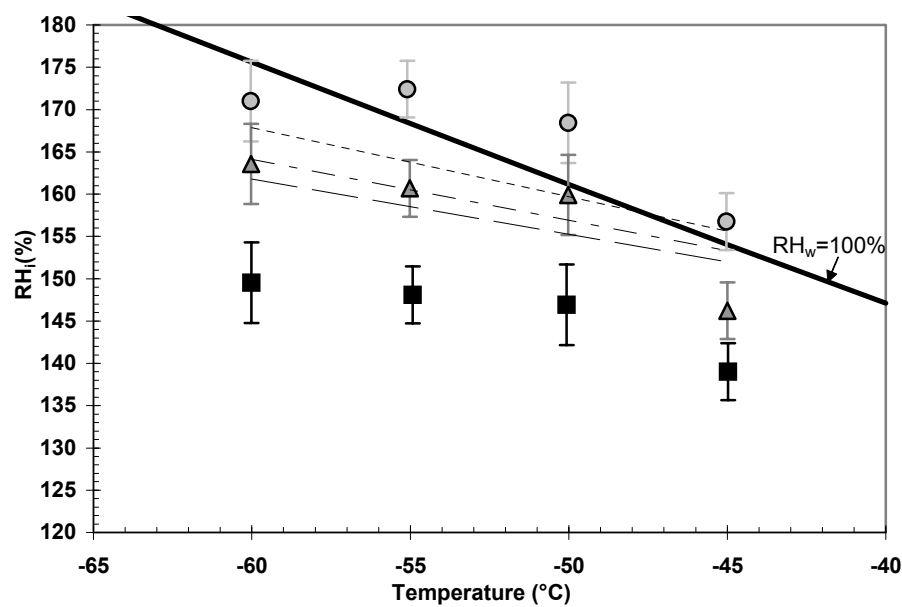


Figure 3.10: As in Figure 3.6, but for CFDC conditions for the formation of ice on 1% of alumina-silicate particles treated with H_2SO_4 .

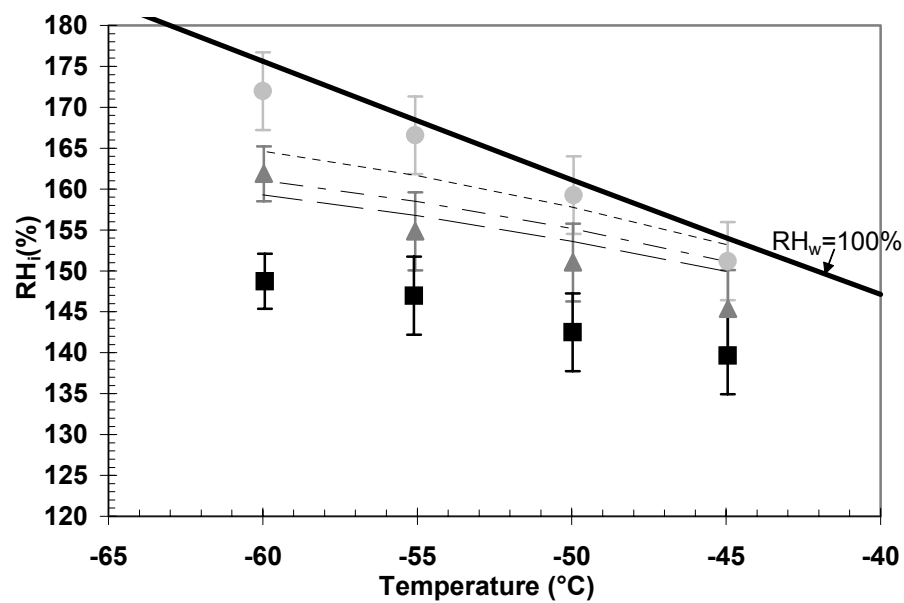


Figure 3.11: As in Figure 3.5, but for CFDC conditions for the formation of ice on 1% of iron oxide particles.

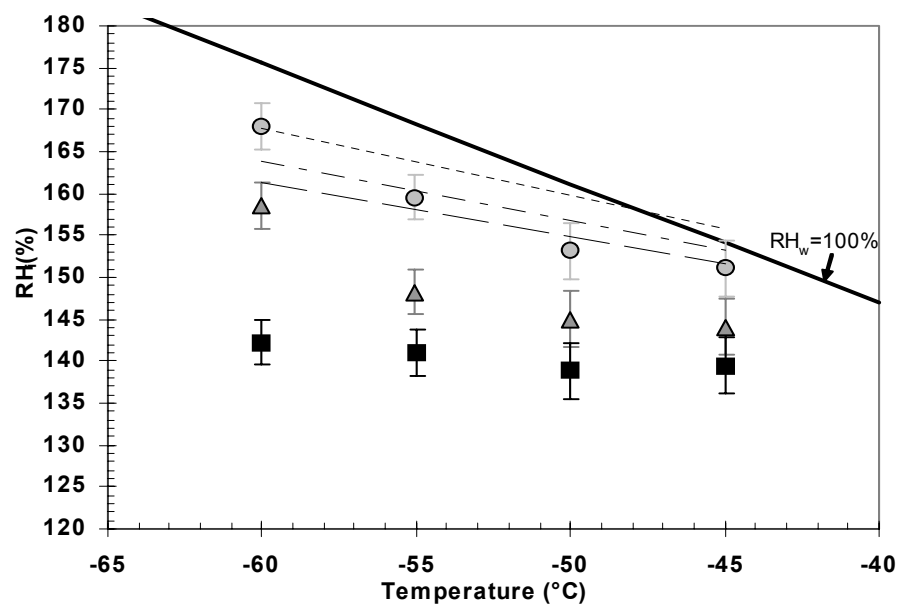


Figure 3.12: As in Figure 3.6, but for CFDC conditions for the formation of ice on 1% of iron oxide particles treated with H_2SO_4 .

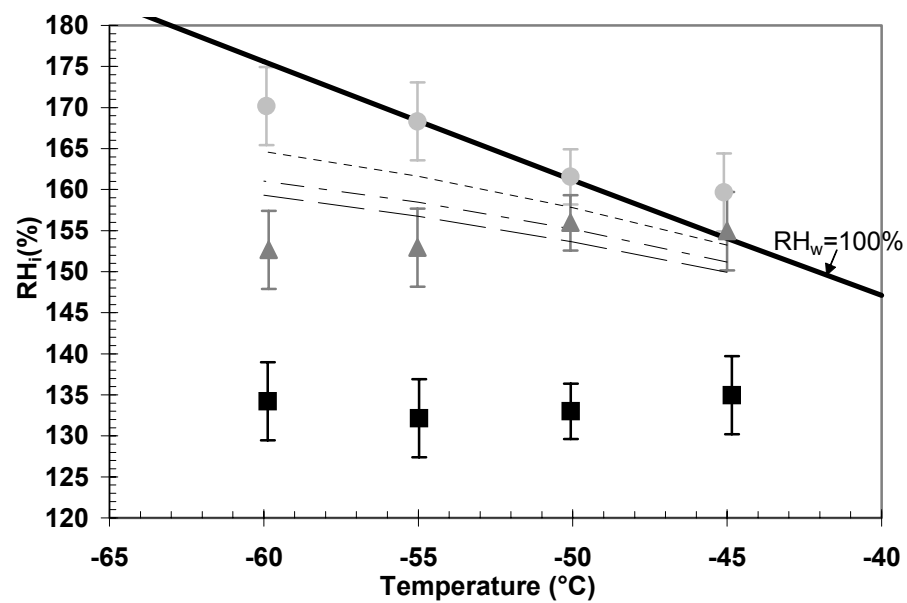


Figure 3.13: As in Figure 3.5, but for CFDC conditions for the formation of ice on 1% of particles from the reference sample of Asian dust particles.

4. Discussion and conclusions

4.1 *Summary of results*

Ice nucleation activity was determined for sub-micron mineral particles with and without condensed H_2SO_4 on the surface of the particles. These analyses do not consider the effects of larger sized particles that occur in a “monodisperse” size distribution resulting from multiple charging in the DMA. The contributions of multiply charged particles is discussed in appendix A.3, where it is discerned that larger particles do not contribute to more than 8% of the ice nucleation activity for 50 nm particles, 27% for the 100 nm particles and no more than 30% of the ice activation for the 200 nm particles when the respective sizes are selected by the DMA.

The aerosol particles displayed ice-forming ability at upper tropospheric temperatures in the CFDC without any H_2SO_4 uptake. The aluminum oxide and alumina-silicate particles exhibited different characteristics than the iron oxide particles. The RH_i determined for 1% ice nucleation of all sizes of the aluminum oxide and alumina-silicate particles equates to the RH_i for homogeneously freezing $\text{H}_2\text{SO}_4/\text{H}_2\text{O}$ particles of the same sizes at around -45°C . At lower temperatures, the RH_i conditions for activation of these particles trend away from the homogeneous freezing conditions and start to induce ice nucleation at warmer temperatures and lower RH_i than those required for homogeneous ice nucleation. Additionally, a profound particle size effect is indicated by increasingly enhanced ice nucleation behavior for the larger particles at colder temperatures. The ΔRH_i between iron oxide activation points for different particle sizes is more constant,

and there is little divergence in the nucleation behavior of the different sizes at lower temperature. Nonetheless, the 100 and 200 nm iron oxide particles still nucleate ice at warmer temperatures and lower RH_i than for homogeneous freezing of H_2SO_4/H_2O particles of these sizes.

Figure 4.1 (a) is a summary of the ice nucleation conditions for the dry, untreated 200 nm aluminum oxide, alumina-silicate and iron oxide minerals with error bars representing 95% confidence intervals. Also included are the homogeneous freezing line for 200 nm H_2SO_4 particles (Chen et al., 2000) and the RH_i inferred for the onset of continental cirrus cloud formation based on observations by Heymsfield and Milosevich (1995). The 200 nm aluminum oxide and alumina-silicate particles trend in the same direction as the conditions reported by Heymsfield and Milosevich. The slope of 200 nm iron oxide particle activation conditions trends more with the homogeneous freezing line. The iron oxide line actually indicates better nucleation at -45°C , but then follows the opposite slope as the aluminum oxide and alumina-silicate activation lines, ending up with ice nucleation at approximately 20% higher RH_i by -60°C .

These mineral aerosol particles showed some CCN activity above water saturation, but virtually no water uptake below 93 % RH_w as measured by the HTDMA system. While the CCN activity indicated the possible presence of a small amount of some condensed, slightly hygroscopic material (possibly organic by-products of the particle generation), the HTDMA data suggested a high deliquescence relative humidity for these compounds. This indicates that a likely ice activation mechanism is deposition nucleation on the insoluble surfaces. This study could shed no light on the microscopic details of such a mechanism.

H_2SO_4 was deposited on the particles to simulate the uptake of soluble material by dust particles that may occur during transit from desert regions, particularly when mixing occurs with polluted air masses. CCN supersaturation spectra measurements suggested that the coated particles contained around 3-8% soluble mass, corresponding to approximately 1.11-2.20 monolayers of acid on the particles. It is presumed that these coatings were sufficient to alter the ice formation mechanism to condensation-freezing. In most cases, this mechanistic alteration inhibited the ice formation ability in varying degrees by increasing the RH_i and the temperature required for activation. Iron oxide was the exception, as the coated and uncoated particles activated at approximately the same conditions within experimental uncertainty. In general, the 200 nm treated particles showed significantly enhanced nucleation over activation that would be expected from homogeneous freezing of the liquid component of the particles. Unlike the untreated particles, the activation lines of all of the treated particles slope in the same direction in RH_i -temperature space as would be expected for homogeneously nucleating particles.

Figure 4.1 (b) is a summary of the freezing conditions for the treated 200 nm aluminum oxide, alumina-silicate and iron oxide minerals, again with error bars representing 95% confidence intervals. Included again is the homogeneous freezing line for 200 nm H_2SO_4 particles (Chen et al., 2000) and the RH_i inferred for the onset of continental cirrus cloud formation from Heymsfield and Milosevich (1995). There is some spread in the data, but the error bars of the activation of the treated iron oxide particles and the aluminum oxide particles overlap when a 95% confidence level is considered. The heterogeneous freezing conditions of these metal oxide particles come much closer to the onset conditions for cirrus formation suggested by Heymsfield and

Milosevich than do previous results for homogenous freezing of sulfate particles measured with the CFDC instrument. The iron oxide results even start to intersect the Heymsfield and Milosevich conditions at -45°C . The range of cirrus formation conditions by the mineral oxide particles also spans the full range of cirrus formation conditions suggested in some other atmospheric studies (e.g., Jensen et al., 2001).

Ice nucleating activity of an Asian dust sample was also determined. The HTDMA water uptake results indicated that the particles contained some soluble matter and that the smaller 50 and 100 nm particles contained relatively more soluble matter than the larger 200 nm particles. This variation in soluble matter content seemed to contribute to a more profound size separation in nucleating conditions observed for the Asian dust particles, especially in the size step between 100 and 200 nm. The 100 nm particles were not remarkably better ice nuclei than homogeneously nucleating 100 nm sulfuric acid particles, but the 200 nm natural mineral dust particles were very effective ice nuclei. The nucleation conditions for the 200 nm Asian dust particles are included along with the data for the treated mineral particles on Figure 4.1 (b). The nucleation for these particles follows a similar shape as the treated particles, but nucleates at RH_i conditions that are 5-9% lower than the treated “pure” particles. Because of the soluble matter present in the Asian dust particles, it is difficult to determine if the nucleation is occurring as for uncoated or coated mineral oxides, although the latter is presumed.

Unlike the other mineral particles, iron oxide exhibited similar nucleation behavior for both uncoated and coated conditions. It seems to be coincidental that the untreated iron oxide surface acted in line with the treated particles, because the activity of the treated iron oxide particles was consistent with that of the other treated particles.

Further investigation into the morphological properties of the minerals (e.g. electron microscopy analyses) would likely provide more insight as to the difference in surface properties between the iron oxide and the other minerals, and the effects of surface morphology on the ice nucleation characteristics. Electron microscopy analysis might also provide some information on the size selective composition of the Asian dust particles, and help elucidate the mechanism by which the Asian dust nucleates ice at cirrus temperatures.

It is interesting that sulfuric acid coatings seemed to inhibit the ice nucleating capability of the aluminum oxide and alumina-silicate particles. A reasonable interpretation of these results may be that a given solid substance has characteristic ice nucleation active sites, which progressively become activated as the temperature is lowered. Bassett et al. (1970) suggested a heterogeneous freezing mechanism that involves adsorption of water at discrete locations on a hydrophobic surface, where the advantage of a hydrophobic surface is that it promotes cluster formations that more easily stabilize and form ice than a liquid-like layer of water. This suggests that a partially hydrophilic substrate, which is an effective ice-nucleating agent in water vapor, is less effective when the surface of the substrate is covered by a liquid layer (e.g. sulfuric acid). Another possibility is that the sulfuric acid partially dissolves the surface of the mineral, rendering some nucleation sites inoperative.

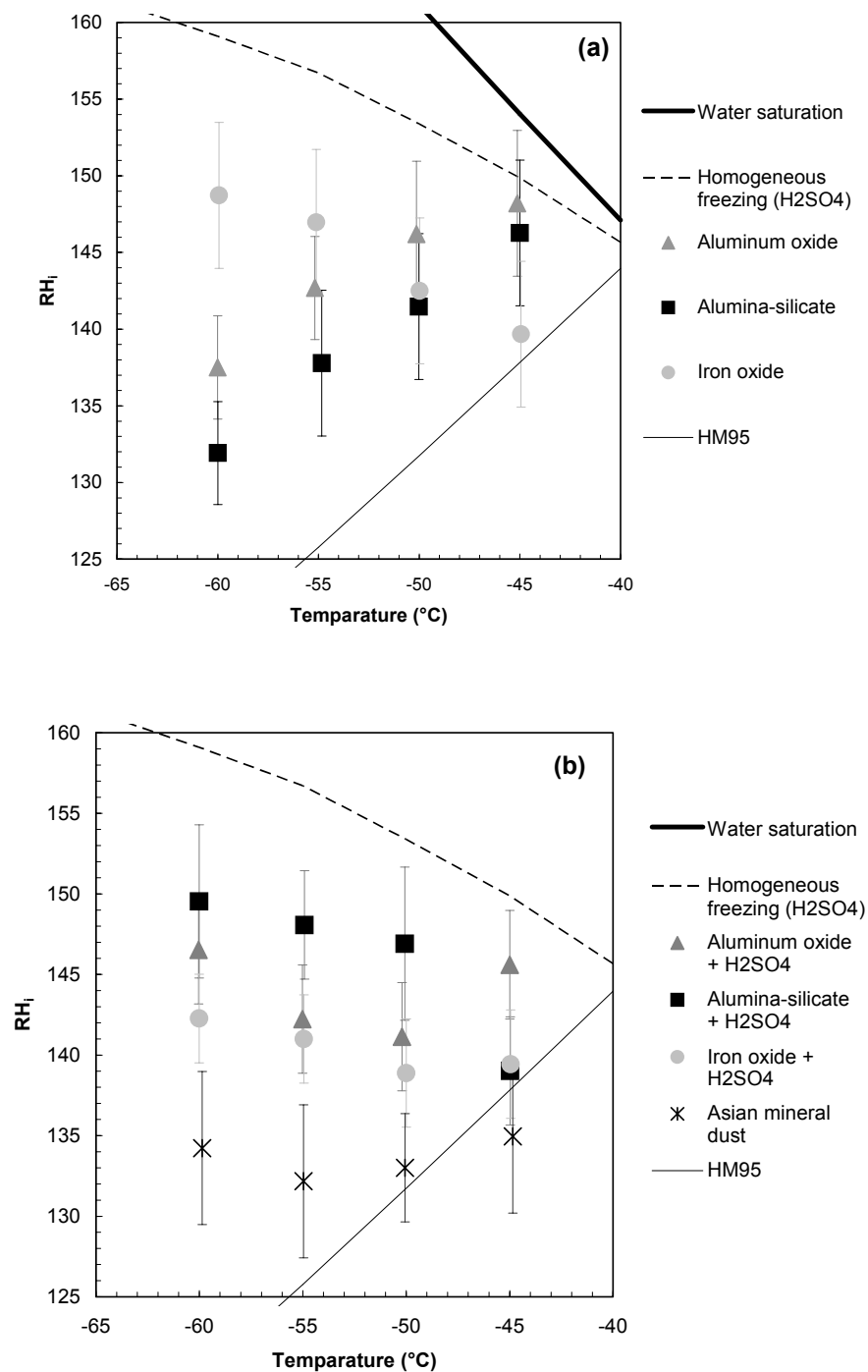


Figure 4.1: The ice formation conditions of 200 nm untreated mineral oxide particles (a) and the treated mineral aerosols along with the Asian dust aerosols (b). A line summarizing the relative humidity required for cirrus nucleation (HM95) derived in a different study (FIRE-II) by Heymsfield and Miloshevich (1995) is also shown. Other lines indicate conditions for homogeneous freezing of 200 nm pure sulfate particles based on CFDC measurements by Chen et al. (2000) and saturation with respect to water.

4.2 Comparison to other laboratory investigations

In order to compare the results for the treated particles in this study to recent results from other investigators, parameterizations and nucleation rate calculations are introduced. The parameterizations may find use in the further study of the implications of these experimental results to cirrus formation. Homogeneous nucleation has been described using a freezing point depression parameterization. Section 4.2.1 explores the possibility of using this parameterization to describe the heterogeneous nucleation of treated particles in this study. Alternately, Koop et al. (2000) has suggested that homogeneous nucleation can be described using parameterization of ice formation as a function of water activity. Section 4.2.2 explores using this parameterization for heterogeneous freezing, and compares these results to the heterogeneous freezing data of Zuberi et al. (2002) who employed a similar parameterization in their study of clay mineral dusts immersed in $(\text{NH}_4)_2\text{SO}_4$ solutions. Section 4.2.3 describes data from this study in terms of nucleation rates. This interpretation lends itself to comparison with data from Hung et al. (2002) who report nucleation rates for hematite (iron oxide) and corundum (aluminum oxide) mineral dust cores with $(\text{NH}_4)_2\text{SO}_4$ coatings.

4.2.1 Parameterization using freezing point depression

Solutes have the effect of lowering the equilibrium melting point of a solution. Sassen and Dodd (1988) formulated a parameterization of homogeneous freezing of solution droplets in cirrus based on earlier observations that the median homogeneous freezing temperatures of emulsified drops were depressed by solutes to an even greater extent than the lowering of the melting point, so that

$$\Delta T_{\text{hf}} = \lambda \cdot \Delta T_{\text{m}} \quad (4.1)$$

where ΔT_{hf} is the homogeneous freezing point depression and ΔT_{m} is the melting point depression for a specific salt concentration. Sassen and Dodd (1988) also proposed that the proportionality constant λ was valid at temperatures other than the temperatures at which drops freeze instantaneously, such that

$$T^* = T + \lambda \cdot \Delta T_{\text{m}} \quad (4.2)$$

where T^* is an effective homogeneous freezing temperature and T is the actual temperature of the solution drops. Using T^* instead of T in a temperature dependent theoretical or parametric expression for the volumetric nucleation rate of pure water then permits estimation of the volumetric nucleation rate of solution drops (J_{hf}) as a function of both temperature and composition. T^* is thus understood as the temperature at which a solution droplet achieves the same nucleation rate as a pure water droplet of the same size. The fraction (F_i) of an aerosol size category freezing in time interval Δt is then readily calculated using $J_{\text{hf}}(T^*)$ in numerical models for drops of volume V_i via the stochastic expression,

$$F_i = 1 - \exp(-J_{\text{hf}}V_i\Delta t). \quad (4.3)$$

DeMott (2002) stated that in investigations involving homogeneous nucleation, λ ranges from 1.4 to 2.2 for different solutions. Sassen and Dodd proposed a λ equal to 1.7 to characterize a wide range of solutes and Chen et al. (2000) confirmed values ranging from about 1.5 to 2 for sulfate aerosols.

It is interesting to ask if it may also be possible to use a similar parameterization to describe heterogeneous freezing and whether the proportionality constant λ is the same for heterogeneously freezing solutions or whether it depends also on the insoluble substrate. Such a parameterization would be useful to calculate $J_{\text{hetf}}(T_{\text{hetf0}})$ for use in a

stochastic equation similar to equation 4.3 (see equation 4.7 later), where J_{hetf} is the heterogeneous freezing rate and T_{hetf0} is an effective heterogeneous freezing temperature akin to T^* . Zuberi et al. (2002) used λ equal to 1.7 to fit their data for the heterogeneous nucleation of ice in aqueous $(\text{NH}_4)_2\text{SO}_4\text{-H}_2\text{O}$ particles containing kaolinite and montmorillonite. They deposited aqueous particles of $(\text{NH}_4)_2\text{SO}_4$ onto a surface containing the powdered dust, thus creating 10-55 μm -sized aqueous particles that had numerous dust particles immersed in each aqueous particle. The particles were then frozen, and optical microscopy was used to determine a median freezing temperature.

Melting point depression data are available from tabulated sources, such as the Handbook of Chemistry and Physics (CRC). A polynomial expression for ΔT_m of H_2SO_4 , based on such data, was given in DeMott et al. (1997)

$$\Delta T_m = 3.513627M + 0.471638M^2 + 0.033208M^3 + 0.02505M^4 \quad (4.4)$$

where M is the molality of the sulfuric acid solution. Following the discussion in DeMott et al. (1994), the expressions can be used for a particle containing a mixture of specific soluble and insoluble components and soluble mass fraction ε_m . M can be evaluated as

$$M = \frac{1000\varepsilon_m m_n}{M_s \left[\left(\pi D_a^3 \rho_l'' \right) / 6 - \varepsilon_m m_n \right]} \quad (4.5)$$

where m_n is the mixed particle mass, M_s is the molecular weight of the solute, D_a is the particle diameter and ρ_l'' is solution density. Droplet sizes and molalities can be inferred by solving the Köhler equation as described in appendix B.

Köhler theory gives expected equilibrium growth and dilution conditions at any RH assuming equilibrium conditions, which is a reasonable assumption for slow vertical motions and RH_w less than 95% (DeMott et al., 1997). The treated 50 nm aluminum oxide and alumina-silicate particles activated as ice nuclei close to or above water

saturation, so the residence time in the chamber may not have been long enough for these particles to equilibrate, and a kinetic model would probably do a better job of describing the particle growth. For this reason, only analyses of the 50 nm treated iron oxide, along with all of the treated 100 and 200 nm particles, are included in this discussion.

Figure 4.2 shows the heterogeneous freezing temperatures recorded using the CFDC for 200 nm treated aluminum oxide particles plotted against water activity (a_w). Water activity was used as the dependent variable because it provides a better means for future comparison with studies that may include a soluble compound other than sulfuric acid. Water activity and the freezing point depression are both functions of molality as indicated in equation 4.4 and appendix B. The curved dotted line in Figure 4.2 indicates the best fit of the data to an equation of the form of 4.2. The line is extrapolated to $a_w = 1$ to estimate an intercept temperature T_{hetf0} , akin to T^* , as the temperature at which pure water particles with mineral dust immersions would freeze in the proportion measured (e.g., 1 in 100 particles freezing) in the CFDC residence time. The best fit was determined by using a least square method, where values of T_{hetf0} and λ were optimized to minimize the square of the distance between the experimental results and melting point depression equation. The resulting equations for treated aluminum oxide, alumina-silicate and iron oxide are listed in Table 4.1. Included under each equation is the square of the correlation coefficient relating the equation to the corresponding experimental data set. Overall, forms of equation 4.2 could be fit to describe the nucleation behavior of the treated 200 nm particles fairly well, with an average r^2 of 0.89. The 100 nm particles could not be fit quite as well with the equations, with an average r^2 of 0.53. For these investigations, the coefficient λ ranges from 1.1 to 1.9 for solutions of H_2SO_4 on 100 and

200 nm aluminum oxide, alumina-silicate and iron oxide particles. The lowest correlation in these studies was for the 100 nm alumina-silicate particles ($r^2=0.37$) where $\lambda = 1.1$. Disregarding this point, the values for the coefficient λ range from 1.4 to 1.9. This range agrees with the range that has been reported from homogeneous freezing investigations ($\lambda = 1.4-2.2$).

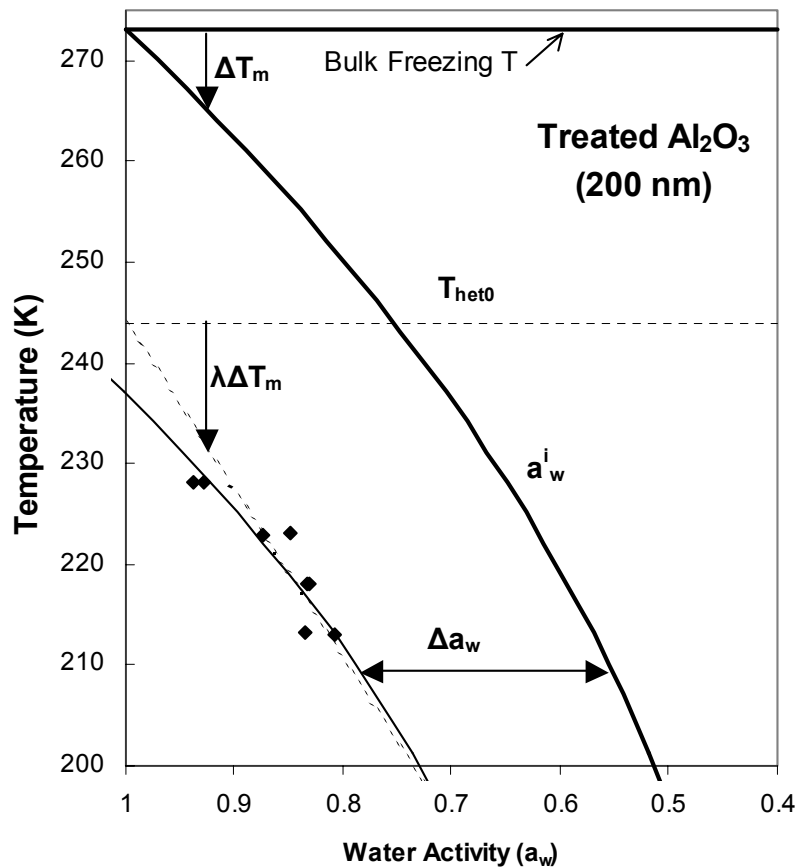


Figure 4.2: Example of data for heterogeneous freezing temperature vs. water activity. The dark solid curve is the activity of water in a bulk solution in equilibrium with ice (a_w^i) and the intersecting solid horizontal line is the bulk freezing temperature for pure water (273.15K) (Buck, 1981). The diamonds represent heterogeneous freezing data (1% of particles freezing in the CFDC residence time) for 200 nm treated Al_2O_3 particles. Arrows represent the melting point depression for pure water (ΔT_m) and the nucleation point depression for diluted sulfuric acid with a mineral immersion ($\lambda \Delta T_m$). The dotted line represents the equation $T = 244 - 1.6 \Delta T_m$ (a) and horizontal dotted line represents the temperature at which pure water with a mineral immersion is expected to freeze (T_{het0}). The solid line represents a_w^i shifted by $\Delta a_w = 0.42$.

Table 4.1: Comparison of the best fit equations for two methods, $T=T_i+\lambda T_m$ and $\Delta a_w=a_w-a_w^i$, used to describe heterogeneous nucleation data for treated 100 and 200 nm aluminum oxide, alumina silicate particles and treated 50, 100 and 200 nm iron oxide particles. Also included is r^2 for each equation as compared to the experimental data set.

		$T (r^2)$	$\Delta a_w (r^2)$
Aluminum Oxide	100	$234-1.5\Delta T_m$ (0.74)	$0.52a_w$ (0.73)
	200	$244-1.6\Delta T_m$ (0.92)	$0.42a_w$ (0.93)
Alumina silicate	100	$230-1.1\Delta T_m$ (0.37)	$0.52a_w$ (0.33)
	200	$247-1.9\Delta T_m$ (0.85)	$0.42a_w$ (0.83)
Iron Oxide	50	$233-1.4\Delta T_m$ (0.55)	$0.52a_w$ (0.54)
	100	$238-1.4\Delta T_m$ (0.47)	$0.45a_w$ (0.48)
	200	$246-1.4\Delta T_m$ (0.91)	$0.38a_w$ (0.91)

4.2.2 Parameterization using water activity

Koop et al. (2000) suggested that homogeneous freezing appears to depend on water activity, such that Δa_w is constant for a given particle size:

$$\Delta a_w = a_w - a_w^i \quad (4.6)$$

where a_w is the water activity of the solution and a_w^i is the water activity of the solution in equilibrium with ice. Zuberi et al. (2002) obtained a reasonable fit when they tested whether this method could be applied to heterogeneous freezing of the mineral dust immersions. To test whether this same idea can be applied to the current data set, best fit Δa_w values were calculated from freezing data for the treated 100 and 200 nm particles in these experiments. The best fit was calculated using a least squares method to minimize the square of the distance between the experimental data and a curve shifted by a constant Δa_w from the a_w^i line. Results for Δa_w for treated aluminum oxide particles are plotted in Figure 4.2 along with the line using the effective freezing temperature concept described earlier. Included in the plots is the line for a_w^i as it relates to temperature (Buck, 1981).

The corresponding Δa_w equations for treated aluminum oxide and the equations that were best fits to the treated alumina silicate and iron oxide data are listed in Table 4.1.

Correlations between these data and the experimental data are also listed. Equation 4.6 could be fit to describe the nucleation behavior of the treated 100 nm and 200 nm particles at least as well as equation 4.2. The 200 nm water activity fit had an average r^2 to the experimental data of 0.89 and the 100 nm particles had an average r^2 of 0.51.

The degree of correlation using the change in water activity concept is very similar to the correlations using the freezing point depression equation. However, there are significant differences in the temperature (T_{hetf0}) at which pure water with a mineral dust immersion is indicated to freeze (where $a_w=1$). For example, looking at Figure 4.2 $T_{\text{hetf0}} = 244\text{K}$ using equation 4.2, and $T_{\text{hetf0}} = 237\text{K}$ using equation 4.6. Because of the limited data set, and the similar goodness of fits between the two methods and the experimental data, it is difficult to determine which method better describes heterogeneous freezing at cirrus temperatures as observed in these experiments. Future experiments to evaluate where similar proportions of highly dilute aerosols freeze at these warmer temperatures could help resolve this issue.

Figure 4.3 shows the constant Δa_w line fits for size resolved data for various compositions of treated particles in this study. For comparison, we also show a constant Δa_w line fit to the Zuberi et al. data for the heterogeneous nucleation of ice in aqueous $(\text{NH}_4)_2\text{SO}_4\text{-H}_2\text{O}$ particles containing koalinite and montmorillonite. The data are compared using water activity in an attempt to normalize the effects of different solutes on the particles. The data from this study approach the data from the Zuberi et al. study as the particles become larger. The mineral dust surface areas in the Zuberi et al. work

are not well quantified, but were certainly representative of much larger particles than in the current study. As suggested by Hung et al. (2002), the Zuberi et al. results could possibly be considered as limiting values obtained for an infinite surface. The new data collected in this thesis support this basic hypothesis and the possible generality of the relation between heterogeneous freezing and water activity for solute-containing mineral oxide and clay particles.

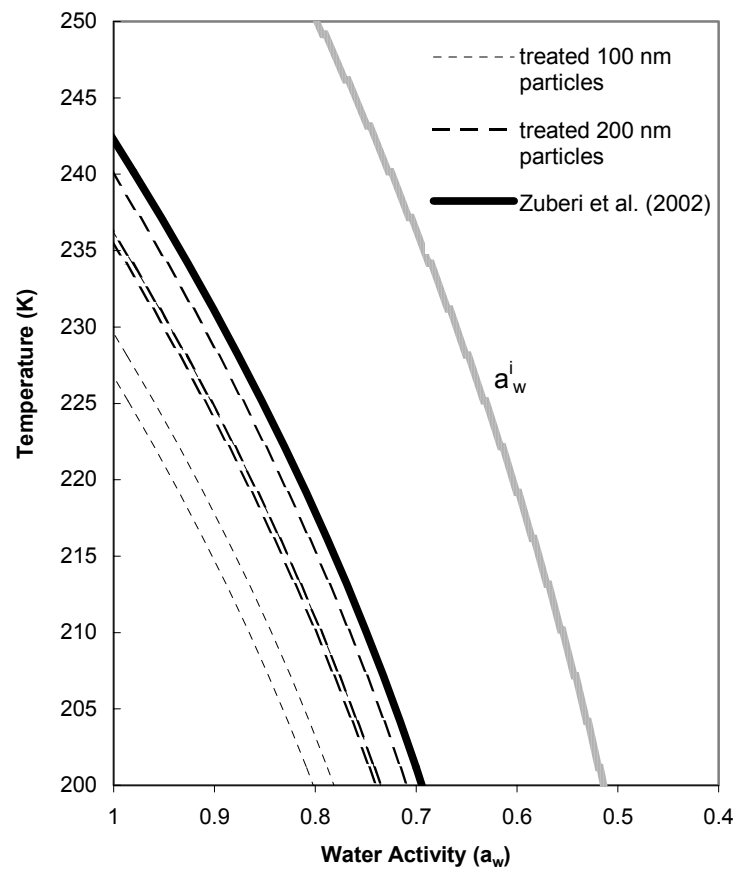


Figure 4.3: Comparison of freezing data using line fits to constant Δa_w . The thick solid line represents results from Zuberi et al. (2002) for large koalinite and montmorillite inclusions in aqueous $(\text{NH}_4)_2\text{SO}_4$. The dotted (dashed) lines represent results from this study for 100 nm (200 nm) aluminum oxide, alumina-silicate and iron oxide particles with H_2SO_4 coatings.

4.2.3 Nucleation rates for ice formation

Equation 4.3 indicated a stochastic expression for the fraction (F_i) of an aerosol of volume V_i homogeneously freezing in a time interval Δt . Heterogeneous nucleation is thought to critically depend on the number of ice nucleation active sites, with the probability of a particle containing active sites increasing with particle surface area. Using the assumption that heterogeneous nucleation depends on the surface areas of the aerosol particles, rather than the volume of the aerosol, a similar expression to equation 4.3 can be used for the probability of heterogeneous freezing,

$$F_i = 1 - \exp(-J_{\text{hetf}} A_i \Delta t) \quad (4.7)$$

where J_{hetf} ($\text{cm}^{-2}\text{s}^{-1}$) is the heterogeneous freezing rate of the particles and A_i (cm^2) is the surface area of the core particle.

Hung et al. (2002) reported values of J_{hetf} computed for hematite (iron oxide) and corundum (aluminum oxide) core particles treated with $(\text{NH}_4)_2\text{SO}_4$. The particles were generated using spray pyrolysis of aqueous metal salt solutions, and subsequently coated with sulfuric acid and neutralized by ammonia. A scanning mobility analyzer was used to characterize the number size distributions of the aerosol, and the mode of this distribution (80 to 250 nm) was changed by varying the precursor solution concentration as indicated in Figure 4.4. The A_i used by Hung et al. for the reported nucleation rates was a function of the mode diameter of various size distributions (D_i), where $A_i = \pi D_i^2$. The sulfuric acid coatings were achieved in a similar manner as described in section 2.1.3 of this work, and the coated particles were neutralized with excess $\text{NH}_3(\text{g})$. Freezing is detected in an aerosol flow tube (AFT) that includes a number of ice-coated segments for preconditioning and a low temperature region where ice nucleation occurs. Infrared

spectroscopy is used to determine the ice formation temperature, and to characterize mole fraction of sulfate on the particles. Nucleation rates were determined by an iterative procedure that involved guessing J_{hetf} values in equation 4.7 and modeling ice formation and growth in the experimental section of the flow tube until the ice mass inferred from calculation matched that inferred from the spectroscopic measurements. The particle composition associated with the frozen particles was inferred from a combination of spectroscopic measurement and numerical modeling of particle-size dependent composition.

For this study, the residence time in the CFDC was approximately 12 seconds. Rogers (1988) indicated that the adjustment time of sample air from room temperature and low RH_w ($\sim 1\%$) to the CFDC conditions was about 2 seconds. Using this information, a Δt of 10 seconds is used. A_i is computed assuming spherical particles where $A_i = \pi D_i^2$ and D_i is the diameter of the mineral dust core, not including the larger particle diameters in the monodisperse flow which result from multiple charging in the DMA (see appendix A.3). With the variables, F_i , A_i and Δt , J_{hetf} can be calculated using equation 4.7. The same system of equations used in the previous section were applied in order to associate a composition and water activity to the nucleation rates that are fixed by the particle sizes and the residence time. Data for conditions where 0.1% of the particles activated were used in this analysis to achieve a broader sense of the trends in nucleation rates. Figure 4.5 shows nucleation rates for aluminum oxide core particles treated with H_2SO_4 compared to the nucleation rates reported by Hung et al. for aluminum oxide core particles treated with $(NH_4)_2SO_4$, and Figure 4.6 shows a similar comparison for the treated iron oxide particles. The results are compared on a water

activity scale to normalize the difference between the use of H_2SO_4 coatings and $(\text{NH}_4)_2\text{SO}_4$ coatings in the respective studies. Homogeneous freezing conditions of H_2SO_4 and $(\text{NH}_4)_2\text{SO}_4$ are not very different as a function of water activity, so it is reasonable to expect that the effect of the solutes on heterogeneous freezing is also quite similar as a function of water activity. The Hung et al. nucleation rates were reported as functions of the $(\text{NH}_4)_2\text{SO}_4(\text{aq})$ mole fraction which was converted to water activity using the Aerosol Inorganics Model (AIM) of Clegg et al. (1998).

Figure 4.5 and Figure 4.6 show that the nucleation rates in this study are higher than the nucleation rates in Hung et al. This is to be expected because this study looks at fractions of 1.0 and 0.1% activating as ice nuclei over about 10s, while Hung et al. reported activation fractions between 0.003 and 0.000003% over 60 s. The slopes of the nucleation rates in this study are shallower at higher nucleation rates and get steeper towards lower nucleation rates. The steeper slopes begin to approach the slopes of the Hung et al. lines, especially in the case of iron oxide. For both minerals, the constant a_w lines for this study are more spread across a larger temperature range than those reported by Hung et al. One factor to be considered in the nucleation rates of Hung et al. is that the particles sizes represent a mode in a number size distribution of data. Figure 4.4 from Hung et al. (2002) shows the amount of overlap in the size distributions represented by the diameter modes. Because the empirically determined nucleation rate in equation 4.7 has a strong dependence on the surface area of the insoluble particles, it is likely that finer resolution in particle size would increase the slope of the constant a_w lines determined from the Hung et al. data, and possibly increase the temperature range represented by the lines. Nevertheless, when the nucleation rates approach comparable

magnitude, the rates from this study appear to become centered on the temperature scale in approximately the same place as the rates from the Hung et al. study. This seems to indicate that the results could be comparable if particle size distributions were defined in a similar manner, instead of comparing broad distributions to nearly monodisperse particle streams. The results also suggest that the particles used in the respective studies were of similar morphology and nucleating characteristics. The results in the current study extend the nucleation rate observations over a wider range of J_{hetf} for use in numerical parameterizations of ice formation by mineral dusts.

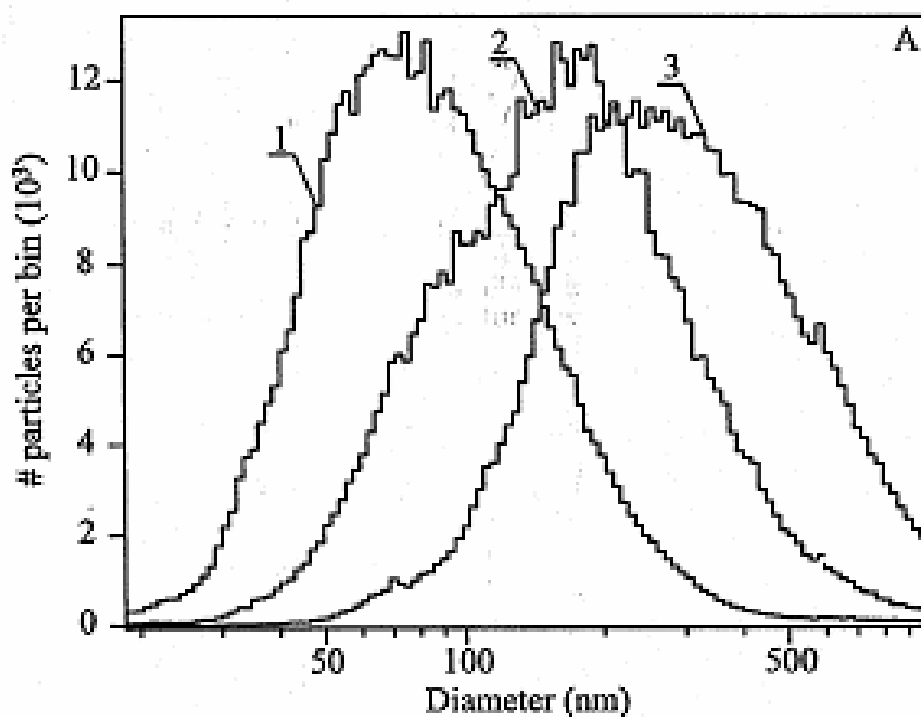


Figure 4.4: Number size distributions of hematite cores prepared from several different $\text{FeCl}_3(\text{aq})$ precursor concentrations (from Hung et al., 2002). Particles generated from 10 mM $\text{FeCl}_3(\text{aq})$ precursor had an 80 nm mode (1), 100 mM a 150 nm mode (2) and 1000 mM a 250 nm mode (3).

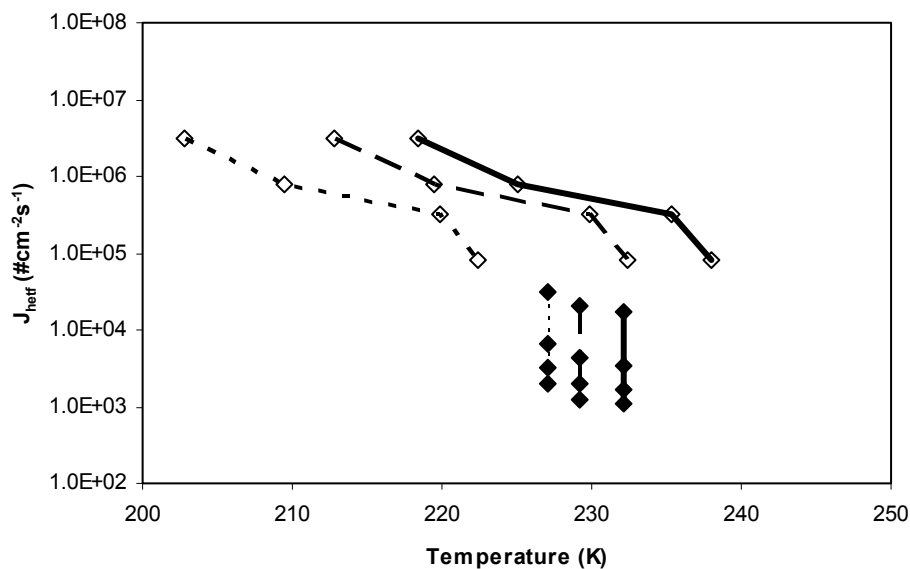


Figure 4.5: Lines with open diamonds represent lines of constant a_w for 1.0 and 0.1% activation of 100 and 200 nm aluminum oxide particles treated with H_2SO_4 . Lines with filled diamonds represent data from Hung et al. (2002) for constant a_w lines indicating between 0.003 and 0.000003% activation of aluminum oxide particles treated with $(\text{NH}_4)_2\text{SO}_4$ with mode diameters of 50, 120, 150 and 200 nm. The different lines represent $a_w = 0.91$ (solid) $a_w = 0.87$ (dashed) and $a_w = 0.79$ (dotted).

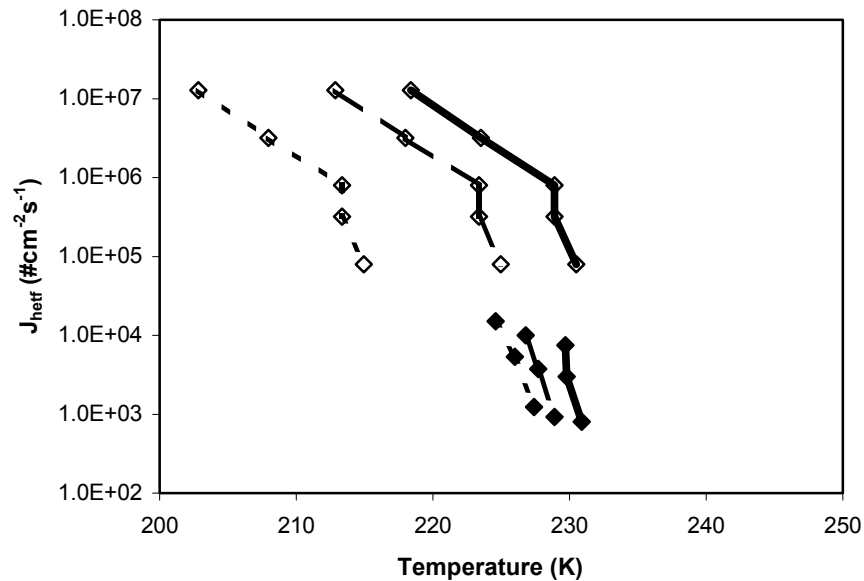


Figure 4.6: Lines with open diamonds represent lines of constant a_w for 1.0 and 0.1% activation of 50, 100 and 200 nm iron oxide particles treated with H_2SO_4 . Lines with filled diamonds represent data from Hung et al. (2002) for constant a_w lines indicating between 0.03 and 0.0003% activation of iron oxide particles treated with $(\text{NH}_4)_2\text{SO}_4$ with mode diameters of 80, 150 and 250 nm. The different lines represent $a_w = 0.91$ (solid) $a_w = 0.87$ (dashed) and $a_w = 0.79$ (dotted).

4.3 Conclusions

A continuous flow diffusion chamber was used to characterize the ice forming characteristics of several nano-scale mineral particles of atmospheric importance at cirrus relevant temperatures. Included in this study were aluminum oxide, alumina-silicate, and iron oxide particles both as single component aerosols and treated with a coating of sulfuric acid. Ice nucleating characteristics were also determined for a reference sample of Asian dust that originated in the Tengger desert in China. These experiments lend themselves to the following conclusions:

- Mineral dust particles are strong contributors to heterogeneous IN populations, especially without soluble coatings. The larger mineral oxide particles used in this study (200 nm in diameter) activated ice formation at lower ice supersaturations than required to homogeneously freeze equivalent-sized sulfate particles. The activation conditions of the larger particles trend towards the cirrus nucleation conditions inferred from the field studies of Heymsfield and Miloshevich (1995), with the onset conditions for the large aluminum oxide and alumina-silicate particles nearly matching the slope of the Heymsfield and Miloshevich line on a RH_i scale.
- Soluble coatings did not enhance the nucleating ability of the mineral particles, and in some cases the coatings were detrimental to the ice forming ability. Nevertheless, coating the 200 nm mineral particles with sulfuric acid led to heterogeneous freezing under less stringent conditions than those where diluted sulfuric acid should freeze homogeneously. Also, while dust particles of different compositions displayed a range of ice nucleation activities in the pure state, they had similar ice nucleation

behaviors when coated with soluble matter. It is theorized that the fundamental ice formation mechanism is altered and that the solute may in some cases have a detrimental effect on the nucleating characteristics of particles because the coatings alter the properties of active nucleation sites on the substrate.

- A clear size effect was indicated for ice formation by all of the particles as larger particles consistently nucleated ice at lower humidity than smaller particles. The smaller 50 nm particles did not show much evidence of being active heterogeneous ice nuclei in cirrus conditions, unlike the 100 and 200 nm particles. This size dependence is reflected in classical theory of heterogeneous nucleation including active sites and is consistent with observations that suggest that IN typically have sizes larger than 0.1 μm (100 nm) (Pruppacher and Klett, 1997; Chen et al., 1998).
- A freezing point depression parameterization that has been used to model homogeneous freezing was applied with some success to heterogeneous freezing of the treated mineral particles in this study. Freezing point depressions were found in a range that is consistent with data that have been reported for homogeneous freezing parameterizations for pure sulfates. A parameterization of ice formation as a function of water activity, also used in describing homogeneous freezing data, was also useful in describing the heterogeneous freezing data with correlations that were similar to the freezing point depression parameterization. Both parameterizations would be useful for describing heterogeneous freezing of mixed dust/sulfate aerosols in numerical cloud models.

In general, the findings in this study support observations that mineral dust particles can act as efficient ice nuclei. These laboratory observations appear to come

closer to a viable explanation of the existing observations of the full range of cirrus onset conditions than homogeneous nucleation alone. This information provides more insight into the radiative forcing of clouds, as these particles in competition with homogeneous freezing processes freeze more readily and can lead to a reduction in ice crystal density in slow updraft cloud parcels, and hence also to a decrease in net cloud albedo (DeMott et al., 1997). Also, the parameterizations developed here should be useful for integrating global dust fields into the modeling of ice formation in cirrus conditions, and for interpreting observations of ice formation in clouds. Climate prediction models that include some of the impacts of mineral dust could also provide some evidence of the effects of increased aridity caused by anthropogenic activities.

4.4 Recommendations for Future Work

These findings regarding heterogeneous ice formation begin to provide a viable explanation for the range and variability of the thermodynamic conditions at which cirrus clouds have been observed to form, but there still remains much to be discerned about the impact of aerosol composition on the heterogeneous freezing process. In this regard, the following suggestions are offered for future research:

- Much of this ice nucleation research has been dedicated to experiments with varieties of materials, but there is little indication as to what makes a certain particle a good or poor nucleator. Electron microscope imagery could help discern characteristics in particle morphology that might relate to active sites for ice nucleation. Imagery could also give an idea of the how the sulfuric acid coatings are distributed, and whether uniform coverage is a valid assumption for the treated particles. Also, imagery could help determine the size-resolved chemistry of the Asian dust sample, for which

smaller particles were believed to have more soluble material than larger ones. To this end, transmission electron micrograph (TEM) grid samples have been collected from this work and will be analyzed in the near future. Pursuit of collaboration with investigators involved in surface catalysis studies is also suggested.

- The H_2SO_4 coatings that were achieved in this study were in the range of approximately 1-2 monolayers. It would be interesting to quantify any change in ice nucleating behavior that results from more variable surface loadings of sulfuric acid. Additionally, it would be interesting to determine whether less acidic sulfate coatings lead to different results.
- Mineral particles in the upper atmosphere are observed coated with water-soluble material including both sulfur and nitrogen compounds (Dentener et al., 1996). Laboratory experiments should be conducted that include analyses of insoluble cores associated with nitric acid (HNO_3) and soluble nitrates at cirrus temperatures.
- A large variety of substances including not only mineral oxides, but clays and partially soluble and insoluble organics, have been implicated as potentially effective IN in the UT. A broader understanding of IN would include not only further laboratory analysis of surrogates of these particles alone, but mixtures that might in themselves include several insoluble and soluble components both internally and externally mixed.
- Analysis of a larger variety of particles, including particle mixtures would come closer to atmospherically relevant particles, but the most atmospherically relevant particles are those from actual sources, like the Asian dust particles that were collected and analyzed for this study. An effort should be made to collect similar

desert dust samples from various regions of the globe to determine relative IN efficiency of aerosols that are associated with dust storms and dust transport.

Appendix A

THEORY OF OPERATION FOR THE DIFFERENTIAL MOBILITY ANALYZER

A.1 Relationship between electrical mobility and particle size

The Differential Mobility Analyzer (DMA) separates submicrometer particles from the incoming polydisperse distribution of particles based upon the relationship between particle electrical mobility and particle size. Charged particles enter an electric field generated in the gap between concentric cylinders in the DMA. The electrical mobility, Z_p , is a measure of the particle's ability to move in an electric field and is defined in the following equation:

$$Z_p = \frac{neC}{3\pi\mu D_p} \quad (A.1)$$

where C is the Cunningham slip correction (Allen and Raabe, 1985), and is defined:

$$C = 1 + \frac{\lambda}{D_p} \left[2.284 + 1.116 \exp\left(\frac{-0.5D_p}{\lambda}\right) \right] \quad (A.2)$$

where n is the number of elementary charges on the particle, e is an elementary charge (1.6×10^{-19} Coulomb), λ is the gas mean free path (cm), μ is the gas viscosity (dyne • s/cm²), and D_p is the particle diameter (cm) (TSI Model 3071A Classifier manual, 2000).

The trajectory of particles in the instrument also depends on the geometry and flowrates used in the classifier. Knutson (1975) determined the following relationship between particle electrical mobility and the DMA parameters:

$$Z_p = \frac{[q_t - 0.5(q_m - q_p)] \ln\left(\frac{r_2}{r_1}\right)}{2(\pi)VL} \quad (\text{A.3})$$

where q_t is the total flowrate through the classifier (11 lpm), q_m is the flowrate of monodisperse aerosol out of the classifier (1 lpm), q_s is the flowrate of sheath air into the instrument (10 lpm), r_2 is the outer radius of the annular space (1.958cm), r_1 is the inner radius of the annular space (0.937cm), V is the voltage on the inner collector rod (volts) and L is the length between the exit slit and polydisperse aerosol inlet (44.4 cm).

Combining equations (A.1) and (A.3) gives an equation that relates the particle diameter to the DMA parameters:

$$D_p = \frac{2neCVL}{3\mu[q_t - 0.5(q_m - q_p)] \ln\left(\frac{r_2}{r_1}\right)} \quad (\text{A.4})$$

Using equation (A.4) particles with a narrow range of electrical mobility can be related to particle size as long as the number of charges on the particle is known.

A.2 Charge distribution

The formula used to calculate the charge distribution for particles carrying zero, one or two charges is a modification by Wiedensohler (1988) of the original charge distribution theory of Fuchs (1963). The approximation formula is:

$$f(N) = 10^{-\left[\sum_{i=0}^5 a_i(N) \left(\log \frac{D_p}{nm} \right)^i \right]} \quad (\text{A.5})$$

Equation (A.5) is valid for the size ranges: $1 \text{ nm} \leq D_p \leq 1000 \text{ nm}$ for $N = -1, 0, 1$; and $20 \text{ nm} \leq D_p \leq 1000 \text{ nm}$ for $N = -2, 2$. For $D_p < 20 \text{ nm}$ the particles carry, at most, one elementary charge. The approximation coefficients $a_i(N)$ are listed in table A.1.

The approximation for the fraction of particles carrying three or more charges is based upon a derivation by Gunn in 1956 (TSI Model 3071A Classifier manual, 2000):

$$f(N) = \frac{e}{\sqrt{4\pi^2 \epsilon_0 D_p k T}} \exp \left[- \frac{\left[N - \frac{2\pi\epsilon_0 D_p k T}{e^2} \ln \left(\frac{Z_{i+}}{Z_{i-}} \right) \right]^2}{2 \frac{2\pi\epsilon_0 D_p k T}{e^2}} \right] \quad (\text{A.6})$$

where e is an elementary charge (1.6×10^{-19} Coulomb), ϵ_0 is the dielectric constant (8.85×10^{-12} farad/m for air), D_p is the particle diameter (m), k is Boltzmann's constant (1.38×10^{-23} joule/K), T is the temperature (K), N is the number of elementary charge units and Z_{i+}/Z_{i-} is the ion mobility ratio (0.875).

Table A.1: Coefficients for equation (A.5)

$a_i(N)$	N				
	-2	-1	0	1	2
a_0	-26.3328	-23.1970	-0.0003	-2.3484	-44.4756
a_1	35.9044	0.6175	-0.1014	0.6044	79.3772
a_2	-21.4608	0.6201	0.3073	0.4800	-62.8900
a_3	7.0867	-0.1105	-0.3372	0.0013	26.4492
a_4	-1.3088	-0.1260	0.1023	-0.1553	-5.7480
a_5	0.1051	0.0297	-0.0105	0.0320	0.5049

A.3 Effects of DMA charge distribution on interpretation of nucleation rates in the CFDC

As stated earlier in section 2.1.2, a purely monodisperse distribution is not achieved by DMA classification because some of the particles become more than singly charged. Multiple charges on a larger particle give it a higher mobility, equal to that of a smaller, singly charged particle. This means that some larger particles reach the exit slit of the DMA and are carried in the monodisperse flow along with particles of the desired size.

The larger particles in the “monodisperse” flow have some influence on the nucleation activity. In section 4.3, a stochastic expression for the heterogeneous nucleation rate (equation 4.3) was used to express the fraction (F_i) of an aerosol of surface area A_i heterogeneously freezing in a time interval Δt . Equation 4.3 is repeated here for reference as equation A.7:

$$F_i = 1 - \exp(-J_{\text{hetf}} A_i \Delta t) \quad (\text{A.7})$$

In the analysis provided here, the general validity of this expression is assumed (e.g., particles are spherical and active sites are not preferentially distributed with respect to size) and it is also assumed that secondary factors do not influence the relative nucleation rates of different sizes of particles. This latter assumption is most valid for the case of uncoated particles, as the coated particle case requires additional consideration of variation of coating with particle size and the effect of differing degrees of solute dilution on nucleation rate. Nevertheless, it is expected that the conclusions apply also to the coated particle case.

Table 2.1 in section 2.1.2 indicated the size and fraction of an evenly distributed particle population that is expected to exist as multiply charged particles for a given particle size selection. The initial size distributions in Figures 3.1 and 3.2 can be used to determine the initial number of particles that exist in a size bin i (dN_i), where dN_i is related to the width of the sampling slit at the bottom of the collector rod. Manufacturer specifications indicate that a selected mobility is obtained within 10% (TSI Model 3071A Classifier manual, 2000), which can be used with equation A.1 to determine a range of particle size as $(1.01 \pm 0.1)D_p$. It follows that a particle size selection of 50 nm

corresponds to a range of 45.5 to 55.5 nm, 100 nm corresponds to a range of 91 to 111 nm, and 200 nm corresponds to 182 to 222 nm.

The sizes and fractions of the charged particles exiting the DMA (Table 2.1) and the values for dN_i , Table A.2 can be constructed which indicates the actual number of particles of a given sizes exiting the DMA. Also indicated are the J_{hetf} calculated using equation A.7 that correspond to 1.0% nucleation of the selected particle size, and a weighted J_{hetf} that indicates the relative contribution of each rate towards nucleation when the multiply charged, different size particles are exposed to the same conditions. The respective J_{hetf} values can be multiplied by the dN_i exiting the DMA to determine the percent that each particle size contributes to the 1.0% activation threshold.

The table indicates that, for DMA particle selections of 50, 100 and 200 nm, the percent contribution to 1.0% activation of the multiply charged particles is at least 6%, but at most 30%. This means that the singly charged particles dominate activation for all particle compositions and sizes in this study. In the preceding results and discussion, when particles sizes are referenced, it should be kept in mind that that the particles are actually discrete distributions, but that the reference particle sizes of 50, 100 and 200 nm likely represent at least 70% of the particle activation when ice nucleation is considered.

Table A.2: The DMA selected diameter, the diameters that result from multiple charges, the initial dN_i determined from the initial size distribution, the fraction of dN_i that is charged in the DMA, and the resulting dN_i of each size which exits the DMA. Also included are nucleation rates for the selected particle size, the weighted effect of each nucleation for the larger particles as compared to the 50, 100 or 200 nm rates and the % that each particle size of the given concentration contributes to the 1.0% activation threshold.

	Selected diameter (nm)	(# charges) size (nm)	Total dN_i	Charged fraction	dN_i exiting DMA	J_{heff} ($\# \text{cm}^{-2} \text{s}^{-1}$) / Weighted rate	% contribution to activation
Aluminum Oxide	50	(+1) 50	2023	0.1694	343	1.28E+07	0.92
		(+2) 72	2109	0.0066	14	2.07	0.08
		(+3) 90	1992	0.0000	0	3.24	0.00
	100	(+1) 100	1941	0.2140	415	3.20E+06	0.78
		(+2) 149	1510	0.0316	48	2.22	0.20
		(+3) 191	1092	0.0034	4	3.65	0.02
	200	(+1) 200	1010	0.2042	206	8.00E+05	0.70
		(+2) 317	500	0.0716	36	2.51	0.30
		(+3) 426	0	0.0154	0	4.54	0.00
Alumina-silicate	50	(+1) 50	1270	0.1694	215	1.28E+07	0.92
		(+2) 72	1318	0.0066	9	2.07	0.08
		(+3) 90	1294	0.0000	0	3.24	0.00
	100	(+1) 100	1236	0.2140	265	3.20E+06	0.73
		(+2) 149	1234	0.0316	39	2.22	0.24
		(+3) 191	945	0.0034	3	3.65	0.03
	200	(+1) 200	906	0.2042	185	8.00E+05	0.74
		(+2) 317	360	0.0716	26	2.51	0.26
		(+3) 426	0	0.0154	0	4.54	0.00
Iron oxide	50	(+1) 50	412	0.1694	70	1.28E+07	0.94
		(+2) 72	311	0.0066	2	2.07	0.06
		(+3) 90	268	0.0000	0	3.24	0.00
	100	(+1) 100	255	0.2140	55	3.20E+06	0.77
		(+2) 149	202	0.0316	6	2.22	0.20
		(+3) 191	161	0.0034	1	3.65	0.03
	200	(+1) 200	149	0.2042	30	8.00E+05	0.76
		(+2) 317	52	0.0716	4	2.51	0.24
		(+3) 426	0	0.0154	0	4.54	0.00
Asian dust	50	(+1) 50	4359	0.1694	738	1.28E+07	0.95
		(+2) 72	2814	0.0066	19	2.07	0.05
		(+3) 90	1970	0.0000	0	3.24	0.00
	100	(+1) 100	1619	0.2140	347	3.20E+06	0.86
		(+2) 149	753	0.0316	24	2.22	0.13
		(+3) 191	469	0.0034	2	3.65	0.01
	200	(+1) 200	430	0.2042	88	8.00E+05	0.94
		(+2) 317	31	0.0716	2	2.51	0.06
		(+3) 426	0	0.0154	0	4.54	0.00

Appendix B

MODIFIED KÖHLER THEORY FOR MIXED PARTICLES

A number of applications in this study require the formulation of Köhler theory for an insoluble particle coated by a sulfuric acid. This is necessary to infer the amount of coating based on CCN data and once this is known, to infer the composition of the solute shell at the freezing points of mixed particles. This discussion of Köhler theory is adapted from DeMott et al. (1997). In formulating these mathematical expressions, the tacit assumption is made that the solute is evenly distributed as a perfect shell on the insoluble core and that the core itself is spherical.

It is useful to begin with the familiar case without an insoluble core, since a number of terms are common to the more general case. Thus, the equilibrium supersaturation ratio (S_{vw}) is determined by curvature and solution effects in the form,

$$\ln(S_{vw}) = \frac{2M_w\sigma_{s/a}}{RT\rho_w a} - \frac{\nu\Phi m_s M_w/M_s}{(4/3\pi\rho_s'' a^3) - m_s}. \quad (B.1)$$

The different terms in this equation may be separated as,

$$A = \frac{2M_w\sigma_{s/a}}{RT\rho_w}; \quad B = \frac{\nu\Phi m_s M_w/M_s}{4/3\pi\rho_s''}; \quad C = \frac{m_s}{4/3\pi\rho_s''}.$$

In these equations, M terms are molecular weight and m terms are mass for water (w) and solute (s), T is temperature, $\sigma_{s/a}$ is the interfacial surface tension at the solution air interface, ρ_w and ρ_s'' are the densities of water and solution, a is droplet radius and R is the Universal Gas Constant. Additionally, the term $\nu\Phi$ is related to molality M and water activity a_w by,

$$\nu\Phi = -\frac{\ln a_w}{(MM_w/1000)}. \quad (\text{B.2})$$

Dilute solution approximations are now considered in order to solve this system of equations for the interesting cases of higher relative humidity and droplet activation. Noting in this case that $\ln S_{vw} \approx S_{vw}$ and dropping the subscript notation for simplicity it is seen that,

$$S-1 = \frac{A}{a} - \frac{B}{a^3 - C} \quad (\text{B.3})$$

This equation may be solved numerically by Newton's method to determine drop radius at any $S-1$. This is done by rearranging terms on the LHS of equation B.3 to get an expression equal to 0, and equating it to the derivative of B.3 with respect to drop size.

Thus,

$$da = \frac{[(S-1)a^3 - Aa^2 + ACa^{-1} + B - C(S-1)]}{[3(S-1)a^2 - 2Aa - ACa^{-2}]} \quad (\text{B.4})$$

By making an initial guess on a (e.g., $a = (B/A)^{0.5}$), the calculation converges very quickly to a condition where $a-da < 10^{-8}$.

Equation B.4 becomes numerically insolvable beyond the critical supersaturation value for droplet activation. This critical value can be determined analytically by noting that the term C can easily be ignored under activation conditions (i.e., $m_s \ll m_w$). Thus, from the derivative of B.3,

$$a_{\text{crit}} = \sqrt{\frac{3B}{A}} \quad (\text{B.5})$$

and upon re-substitution in (B.3),

$$S_{\text{crit}} - 1 = \sqrt{\frac{4A^3}{27B}} \quad (\text{B.6})$$

The general case of a mixed particle is now considered. In this case, B.1 may be shown (see, e.g., Pruppacher and Klett, 1997) to take the form,

$$\ln(S_{\text{vw}}) = \frac{2M_w \sigma_{s/a}}{RT \rho_w a} - \frac{\nu \Phi m_s M_w / M_s}{4/3 \pi \rho_w (a^3 - r_u^3) - \frac{m_s}{\rho_s''}} \quad (\text{B.7})$$

The insoluble particle radius r_u has been introduced in this equation. The solute mass in this case is $m_s = \epsilon_m m_p$, where ϵ_m is the soluble mass fraction and m_p is the total particle mass. In the dilute solution approximation, as before, this equation may be rewritten,

$$S - 1 = \frac{A}{a} - \frac{B'}{a^3 - C'} \quad (\text{B.8})$$

where $B' = \frac{B \rho_s''}{\rho_w}$ and $C' = r_u^3 + C \rho_w$.

Thus, B.4 holds in this case if C is replaced with C' . For very dilute solutions as exist near cloud activation, $\rho_s'' \approx \rho_w \approx 1$, so $B' \approx B$ and $C' \approx r_u^3 + C$. Again, term C is negligible at critical conditions, so it is clear that in this general case for mixed particles, expressions B.5 and B.6 are also valid approximations for the critical size and supersaturation as long as ϵ_m is not less than the equivalent of at least one monolayer of surface coverage. This was confirmed by solving the general form of B.4 numerically to the point of activation.

The expressions introduced thus far become less accurate as relative humidity decreases. To obtain a more exact solution for determining the equilibrium composition

of coated solutions under the conditions where ice formed in the CFDC studies, the Köhler equation was evaluated numerically in the form,

$$S_{vw} = \exp \left[\frac{2M_w \sigma_{s/a}}{RT \rho_w a} - \ln(a_w) \right] \quad (B.9)$$

This form is convenient because most parameters may be expressed as a function molality or weight percent solute based on tabulated experimental and thermodynamic model data. For example, a_w is available from thermodynamic models (e.g., Clegg et al., 1998) and $\sigma_{s/a}$ is tabulated versus sulfuric acid composition in the CRC Handbook of Chemistry and Physics. Also,

$$a = \left(\frac{V_s}{4/3\pi} + r_u^3 \right)^{1/3} \quad (B.10)$$

where solution volume V_s is given by,

$$V_s = \frac{1}{\rho_s} \left(\frac{1000 \epsilon_m m_p}{M M_s + \epsilon_m m_p} \right) \quad (B.11)$$

Using an initial guess on M , values were obtained for $\sigma_{s/a}$, a_w , and ρ_s from polynomial expressions that were derived over the valid range of tabulated data. A bisectional solver routine was used to minimize the difference between observed S_{vw} and the LHS of B.9 in order to define a as a function of RH at the observation temperature. The homogeneous freezing rate of the liquid portion of particles can be computed using B.9 to B.11 in combination with an expression for homogeneous freezing as a function of molality, as provided by Chen et al. (2000).

Appendix C

UNCERTAINTY ANALYSIS FOR THE CFDC

C.1 Variations in average temperature and relative humidity

Inner and outer wall temperatures in the CFDC were independently controlled by bath circulators with temperature control sensitivity of $\pm 0.02^\circ\text{C}$. The circulators chill and circulate the heat transfer fluid through copper tubing coils surrounding the outer wall and into a reservoir inside the inner wall. Four outer wall thermocouples and three inner wall thermocouples (copper-constantan (type “T”) thermocouples) were used to measure temperature along the length of the CFDC. On the outside wall, these thermocouples were electrically insulated from, but kept in close thermal contact with the copper pipes carrying fluid from the circulators. A hollow brass rod contains the thermocouples that measure the temperature of the inner wall in the CFDC. The approximate location of each of the seven thermocouples is indicated in Figure C.1. The assumptions are made that the temperatures of the outer ice surface and the temperature of the outer wall of CFDC are equal, and that the temperature of the inner ice surface, and the temperature measured in the coolant reservoir are equal.

The sample temperature is a function of the temperature of the cold wall (T_c), the temperature of the warm wall (T_w) and the fractional distance of the sample lamina from the cold wall (x):

$$T_x = T_c + x(T_w - T_c) \quad (\text{C.1})$$

The aerosol position x is also a function of temperature, as it is determined by the mass balance of sheath air on either side of the aerosol lamina. The aerosol position is

displaced towards the cold side because the colder, denser air has less volume per unit mass of air.

The temperature difference between the two cylinders is also the fundamental quantity defining the relative humidity at the sample position. The vapor pressure with respect to ice at temperature T ($e_i(T)$) is calculated using an equation from Buck (1981) which is optimized for conditions in the temperature range between -80 and 0°C :

$$e_i(T) = 6.1115 \exp\left(\frac{22.542T}{T + 273.48}\right) \quad (\text{C.2})$$

where $e_i(T)$ is the vapor pressure in mb and T is the temperature in $^\circ\text{C}$. Equation (C.2) can be used to calculate the vapor pressure at the cold wall ($e_i(T_c)$) and the vapor pressure at the warm wall ($e_i(T_w)$). The vapor pressure at position x (e_x) can then be interpolated in a similar manner as the temperature at position x :

$$e_x = e_i(T_c) - x[e_i(T_c) - e_i(T_w)] \quad (\text{C.3})$$

The relative humidity with respect to ice (RH_i) at position x can then be calculated as the ratio of the vapor pressure at position x and the saturation vapor pressure at the temperature T_x :

$$\% \text{RH}_i = 100 \times \frac{e_x}{e_i(T_x)} \quad (\text{C.4})$$

The data acquisition program (see section 2.5) uses an average of the four thermocouples along the warm wall and the three thermocouples along the cold wall to compute T_w and T_c . These temperatures are then used along with the above equations to compute the temperature and relative humidity conditions experienced by the sample. Table C.1 is an example of the variability of the temperature and relative humidity conditions experienced by the sample as recorded by the data acquisition program using

average wall temperatures. The values represent the averages of about 3 minutes of data, where data are recorded by the program every 1 second. Under stable conditions, the maximum standard deviation for the temperatures was about 0.02° , while the maximum standard deviation of the percent relative humidity with respect to ice was about 0.14%.

While the data acquisition program records variability in the overall average readings for the warm and cold walls, no accounting is made for variability amongst the thermocouples along the warm and cold walls. The four thermocouples on the outer wall and the three thermocouples along the inner wall are placed at different positions along the chamber length as indicated in Figure C.1. To assess the range of temperature variation that a sample experiences as it travels vertically through the CFDC, the data are recorded at each of the seven thermocouples. A standard deviation of temperatures along the warm wall can be calculated along with a standard deviation of the temperatures along the length of the cold wall. The standard deviation of the dependent variables T_x , $e_i(T)$, e_x and $\%RH_i$, can then be calculated using an error propagation formula.

For this error analysis, the standard error propagation formula is used, wherein if we have a function:

$$u = f(x, y, z) \quad (C.5)$$

then the standard deviation of the function u (s_u) is calculated using the following formula:

$$s_u = \sqrt{\left(\frac{\partial u}{\partial x}\right)^2_{y,z} s_x^2 + \left(\frac{\partial u}{\partial y}\right)^2_{x,z} s_y^2 + \left(\frac{\partial u}{\partial z}\right)^2_{x,y} s_z^2} \quad (C.6)$$

Applying (C.6) to (C.1) gives the standard deviation of T_x (s_{Tx}):

$$s_{Tx} = \sqrt{(1-x)^2 s_{T_c}^2 + (x)^2 s_{T_w}^2 + (T_w - T_c)^2 s_x^2} \quad (C.7)$$

The standard deviation of $e_i(T)$ is calculated by applying equation (C.6) to (C.2):

$$s_{e_i(T)} = \left(\frac{22.542(T + 273.48) - 22.542T}{(T + 273.48)^2} \right) \exp\left(\frac{22.542T}{T + 273.48} \right) s_T \quad (C.8)$$

The standard deviation of e_x is found by applying (C.6) to (C.3):

$$s_{e_x} = \sqrt{(1-x)^2 s_{e_i(T_c)}^2 + (x)^2 s_{e_i(T_w)}^2 + (e_i(T_c) - e_i(T_w))^2 s_x^2} \quad (C.9)$$

and the standard deviation of $\%RH_i$ is found similarly by applying (C.6) to (C.4):

$$s_{\%RH_i} = \sqrt{\left(\frac{100}{e_i(T_x)} \right)^2 s_{e_x}^2 + \left(-\frac{100e_x}{e_i^2(T_x)} \right)^2 s_{e_i(T_x)}^2} \quad (C.10)$$

Table C.2 is an example of the variability in the temperature and RH_i conditions that the sample experiences along the length of the CFDC, calculated using the above equations. The table indicates average temperatures from each of the thermocouples, and the variability that thermocouple location imparts upon the temperature and RH_i calculations. This error is about one order of magnitude larger than the error indicated in Table C.1.

Table C.1: Example of the average and standard deviation of temperature and relative humidity conditions recorded in the CFDC. Each value is an average of about 3 minutes of data recorded every 1 second.

Outer Wall (°C)	Inner Wall (°C)	$T_x \pm s_{T_x}$ (°C)	$RH_i \pm s_{RH_i}$
-34.5	-50.5	-45.0 ± 0.02	146.6 ± 0.13
-39.9	-55.3	-50.0 ± 0.01	146.6 ± 0.13
-45.4	-60.0	-55.1 ± 0.01	146.6 ± 0.13
-50.5	-64.6	-60.0 ± 0.01	147.2 ± 0.14

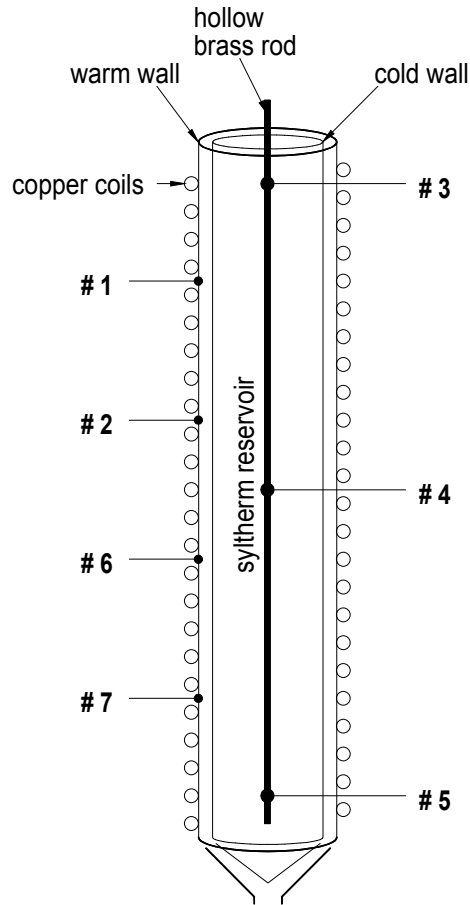


Figure C.1: Approximate location of the four warm wall thermocouples (#1,2,6,7) and the three cold wall thermocouples (#3,4,5) along the length of the CFDC. Also indicated are the copper coils which carry coolant from the circulator to cool the outer wall, and the coolant reservoir that contains a brass rod which holds the inner wall thermocouples. Figure is not to scale.

Table C.2: Example of variability in temperature and relative humidity conditions propagated from temperature variability along the length of the CFDC. Each value is an average of about 3 minutes of data recorded every 1 second.

Outer Wall (°C)				Inner Wall (°C)			$T_x \pm s_{T_x}$ (°C)	%RH _i ± s _{%RH_i}
1	2	3	4	1	2	3		
-34.9	-34.7	-34.6	-33.7	-50.4	-50.9	-50.3	-45.0 ± 0.3	146.6 ± 1.4
-40.4	-40.2	-40.1	-39.0	-55.2	-55.4	-55.1	-50.0 ± 0.2	146.6 ± 1.5
-45.8	-45.6	-45.5	-44.5	-59.9	-60.2	-59.9	-55.1 ± 0.2	146.6 ± 1.5
-51.0	-50.7	-50.6	-49.6	-64.3	-65.0	-64.3	-60.0 ± 0.3	147.2 ± 1.7

C.2 Estimation of error in onset of ice formation

The experiments in this study are time consuming, so more effort was placed in acquiring breadth of data to distinguish overall trends, than in replicate analysis. Out of 84 distinct data points collected for different particle sizes, composition and temperature conditions, 1 to 2 replicates were performed for 39 (46%) of the points. To determine the standard deviation in RH_i conditions at which 0.1% of particles form ice, a pooled standard deviation (s_p) is used:

$$s_p = \sqrt{\frac{(n_1 - 1)s_1^2 + \dots + (n_j - 1)s_j^2}{n_1 + \dots + n_j - j}} \quad (\text{C.11})$$

where n_1, \dots, n_j indicate the number of data points in each set 1, ..., j and s_1, \dots, s_j indicate the corresponding standard deviations of these subgroups. If all data are grouped together, an $s_p = 2.83 \text{ \%RH}_i$ (1.67 \%RH_w) is calculated.

Because the sample sizes for each of the individual tests are small (2-3 replicates), a t statistic can be used to compute the confidence intervals about a sample mean as follows:

$$\text{C.I.} = x \pm t \frac{s_p}{\sqrt{n}} \quad (\text{C.12})$$

where x is the sample average, n is the number of duplicates in the sample set and s_p is the pooled standard deviation that was calculated for the entire set of data. The value t is determined at the appropriate confidence level from a table of the t-statistic for the total degrees of freedom corresponding to the entire data set (in this case, 45). To determine whether 2 results are statistically different a hypothesis test can be used. This is most accurately done by using the pooled standard deviation and calculating $t_{\text{experimental}}$ as:

$$t_{\text{experimental}} = \frac{|x_1 - x_2|}{s_p \sqrt{\frac{1}{n_1} + \frac{1}{n_2}}} \quad (\text{C.13})$$

where x_1 and x_2 are the average values to be compared, n_1 and n_2 are the number of experiments included in each of the averages and s_p is the pooled standard deviation that was calculated for the entire set of data. The value t_{critical} is determined at the appropriate confidence level from a table of the t-statistic for the total degrees of freedom used to calculate s_p .

As an example, consider two results for 200 nm iron oxide particles where $x_1 = 148.7 \%RH_i$ is an average of two points for 1.0% ice nucleation by untreated particles at -60°C and $x_2 = 142.3 \%RH_i$ is an average of three points for treated particles. We can calculate a $t_{\text{experimental}}$ using equation C.13:

$$t_{\text{experimental}} = \frac{|148.7 - 142.3|}{2.83 \sqrt{\frac{1}{2} + \frac{1}{3}}} = 2.47 \quad (\text{C.14})$$

Comparing $t_{\text{experimental}}$ with t_{critical} values from table C.3 (an excerpt from a table of the t-statistic for 45 degrees of freedom) we see that $2.41 < 2.47 < 2.69$, so we can say with somewhere between a 99% and 99.5% confidence level that there is a statistically significant difference between these values. The calculated % confidence levels for several other comparisons of experimental data for this study are indicated in Table C.4. Values indicate when a difference between data points cannot be statistically verified with at least 90% confidence (< 90) and when values can be considered statistically different at confidence levels greater than 90%.

Table C.3: Values at selected confidence levels for t_{critical} at 45 degrees of freedom.

d.o.f	Confidence level (1- α)							
	0.6	0.75	0.9	0.95	0.975	0.99	0.995	0.999
45	0.25	0.68	1.30	1.68	2.01	2.41	2.69	3.28

Table C.4: The % confidence levels at which the difference in RH_i conditions for 1% ice nucleation of the indicated particle sizes for the indicated comparisons are calculated to be statistically different. Comparisons include mineral particles (untreated) and mineral particles with surface treatments of sulfuric acid (treated), mineral particles and pure sulfuric acid (H_2SO_4) and mineral particles with sulfuric acid coatings compared with the calculated homogeneous freezing conditions of the coating (H_2SO_4 coating).

		<i>particle diameter (nm)</i>											
		50				100				200			
		<i>Temperature (°C)</i>											
Aluminum oxide	Untreated and treated	<90	<90	<90	99.5	<90	<90	<90	99.5	<90	<90	<90	99
	Untreated and H_2SO_4	95	<90	<90	99.5	97.5	<90	<90	<90	99.5	99	99.5	99.5
	Treated and H_2SO_4 coating	<90	<90	<90	99	<90	<90	<90	<90	<90	99.9	99.9	99.9
Alumina-silicate	Untreated and treated	<90	99.9	99.9	99.9	<90	99.9	99.9	99.9	97.5	<90	99.9	99.9
	Untreated and H_2SO_4	99.5	99.5	<90	<90	99.5	99.5	99	99	99.5	99.9	99.9	99.9
	Treated and H_2SO_4 coating	<90	97.5	97.5	<90	95	<90	<90	<90	99.9	97.5	99.5	99.5
Iron oxide	Untreated and treated	<90	95	97.5	<90	<90	95	95	<90	<90	<90	95	99
	Untreated and H_2SO_4	99.9	<90	97.5	99.9	99.9	95	<90	99.5	99.9	99.9	<90	<90
	Treated and H_2SO_4 coating	<90	95	<90	<90	99	99.9	99.9	<90	99.9	99.9	99.9	99.9
Asian Dust	Untreated and H_2SO_4	<90	<90	99	99.9	<90	<90	<90	<90	99.9	99.9	99.9	99.9

REFERENCES

- Afeti, G.M., F.J. Resch, 2000: Physical characteristics of Saharan dust near the Gulf of Guinea. *Atmospheric Environment*, **34**, 1273-1279.
- Bassett, D.R., E.A. Boucher and A.C Zettlemoyer, 1970: Adsorption studies on ice-nucleation substrates. Hydrophobed silicas and silver iodide. *Journal of Colloid and Interface Science*, **31**, 436-446.
- Brechtel, F.J. and S. M. Kreidenweis, 2000: Predicting Particle Critical Supersaturation from Hygroscopic Growth Measurements in the Humidified TDMA, Part I: Theory and Sensitivity Studies. *J. Atmos. Sci.*, **57**, 12, 1854-1871.
- Buck, A.L., 1981: New equations for computing vapor pressure and enhancement factor. *J. Appl. Meteor.*, **20**, 1527-1532.
- Buseck, P.R., and M. Posfai, 1999: Airborne minerals and related aerosol particles: Effects on climate and the environment. *Proc. Natl. Acad. Sci.*, **96**, 3372-3379.
- Chen, Y., P.J. DeMott, S.M. Kreidenweis, D.C. Rogers, and D.E. Sherman, 2000: Ice formation by sulfate and sulfuric acid aerosol particles under upper tropospheric conditions. *J. Atmos. Sci.*, **57**, 3752-3766.
- Chen, Y., S.M. Kreidenweis, L.M. McInnes, D.C. Rogers, and P.J. DeMott, 1998: Single particle analysis of ice nucleation aerosols in the upper troposphere and lower stratosphere. *Geophys. Res. Lett.*, **25**, 1391-1394.
- Clegg, S.L., P. Brimblecombe, and A. S. Wexler, 1998: A Thermodynamic Model of the System $\text{H}^+ - \text{NH}_4^+ - \text{SO}_4^{2-} - \text{NO}_3^- - \text{H}_2\text{O}$ at Tropospheric Temperatures. *J. Phys. Chem.*, **102A**, 2137-2154.
- DeMott, P.J., 2002: *Laboratory studies of cirrus cloud processes*. In *Cirrus*, D.K. Lynch, K. Sassen, D.O.C. Starr, and G. Stephens Eds., Oxford Univ. Press, 102-135.
- DeMott, P.J., D.C. Rogers, and S.M. Kreidenweis, 1997: The susceptibility of ice formation in upper tropospheric clouds to insoluble aerosol components. *J. Geophys. Res.*, **102**, 19575-19584.
- DeMott, P.J., M.P. Meyers, and W.R. Cotton, 1994: Parameterization and impact of ice initiation processes relevant to numerical model simulations of cirrus clouds. *J. Atmos. Sci.*, **51**, 77-90.
- DeMott, P.J., Y. Chen, S.M. Kreidenweis, D.C. Rogers, and D.E. Sherman, 1999: Ice formation by black carbon particles. *Geophys. Res. Lett.*, **26**, 2429-2432.

- Dentener, F.J., G.R. Carmichael, Y. Zhang, J. Lelieveld, and P.J. Crutzen, 1996: Role of mineral aerosol as a reactive surface in the global troposphere. *J. Geophys. Res.*, **101**, 22869-22889.
- Fuchs, N.A., 1963: On the stationary charge distribution on aerosol particles in a bipolar ionic atmosphere. *Geophys. Pura Appl.*, **56**, 185-193.
- Han, J. and S.T. Martin, 2001: An aerosol chemical reactor for coating metal oxide particles with $(\text{NH}_4)_2\text{SO}_4\text{-H}_2\text{SO}_4\text{-H}_2\text{O}$. 1. New particle formation. *Aerosol Science and Technology*, **34**, 363-372.
- Heintzenberg, J., K. Okada, and J. Stöm, 1996: On the composition of non-volatile material in upper tropospheric aerosols and cirrus crystals. *Atmospheric Research*, **41**, 81-88.
- Heymsfield, A.J. and L.M. Miloshevich, 1995: Relative humidity and temperature influences on cirrus formation and evolution: Observations from wave clouds and FIRE II. *J. Atmos. Sci.*, **52**, 4302-4326.
- Hung H.M., A. Malinowski and S.T. Martin, 2002: Kinetics of Heterogeneous Ice Nucleation on the Surfaces of Mineral Dust Cores Inserted into Aqueous Ammonium Sulfate Particles. Submitted to *J. Phys. Chem. A*.
- Isono, K., M. Komabayasi, and A. Ono, 1959: The nature and origin of ice nuclei in the atmosphere. *J. Meteor. Soc. Japan*. **37**, 211-233.
- Jensen, E.J., O.B. Toon, S.A. Vay, J. Ovarlez, R. May, T.P. Bui, C.H. Twohy, B.W. Gandrud, R.F. Pueschel, and U. Shumann, 2001: Prevalence of ice-supersaturated regions in the upper troposphere: Implications for optically thin ice cloud formation. *J. Geophys. Res.*, **106**, 17253-17266.
- Koop, T., B.P. Luo, A. Tsias, and T. Peter, 2000: Water activity as the determinant for homogeneous ice nucleation in aqueous solutions. *Nature*, **406**, 611-614.
- Levin, Z., E. Ganor and V. Gladstein, 1996: The effects of desert particles coated with sulfate on rain formation in the eastern Mediterranean. *Journal of Applied Meteorology*, **35**, 1511-1523.
- Liou, K.N., 1986: Influence of cirrus clouds on weather and climate processes: a global prospective. *Monthly Weather Review*, **114**, 1167-1199.
- Nenes, A., P.Y. Chuang, R.C. Flagan, and J.H. Seinfeld, 2001: A theoretical analysis of cloud condensation nucleus (CCN) instruments. *J. Geophys. Res.*, **106**, 3449-3474.

- Noble, C.A., and K.A. Prather, 1996: Real-time measurement of correlated size and composition profiles of individual atmospheric aerosol particles. *Environ. Sci. and Technol.*, **30**, 2667-2680.
- Penner, J.E., D. Hegg, and R. Leaitch, 2001: Unraveling the role of aerosols in climate change. *Environ. Sci. and Technol.*, 332A-340A.
- Prenni, A.J., P.J. DeMott, S.M. Kreidenweis, and D.E. Sherman, 2001: The effects of low molecular weight dicarboxylic acids on cloud formation. *J Phys. Chem.*, **105**, 11240-11248.
- Pruppacher, H.R., and J.D. Klett, 1979: *The Microphysics of Clouds*. Reider Publication, 714 pp.
- Rogers, D.C., 1988: Development of a continuous flow thermal gradient diffusion chamber for ice nucleation studies. *Atmospheric Research*, **22**, 149-181.
- Sassen, K., 2002: Indirect climate forcing over the western US from Asian dust storms. *Geophys. Res. Lett.*, **29**(10), doi: 10.1029/2001GL014051.
- Sassen, K., and G. C. Dodd, 1988: Homogeneous nucleation rate for highly supercooled cirrus cloud droplets. *J. Atmos. Sci.*, **45**, 1357-1369.
- Stephens G.L., S.C. Tsay, P.W. Stackhouse, Jr., and P.J. Flatau, 1990: The relevance of the microphysical and radiative properties of cirrus clouds to climate and climatic feedback. *J. Atmos. Sci.*, **47**, 1742-1753.
- Wiedensohler, A., 1988: An approximation of the bipolar charge distribution for particles in the submicron size range. *J. Aerosol Sci.*, **19**, 387-389.
- Wiedensohler, A., and H.J. Fissan, 1991: Bipolar charge distributions of aerosol particles in high-purity Argon and Nitrogen. *Aer. Sci. and Tech.*, **14**, 358-364.
- Wyslouzil, R.E., K.L. Carleton, D.M Sonnenfroeh, and W.T. Rawlins, 1994: Observation of hydration of single, modified carbon aerosols. *Geophys. Res. Lett.*, **19**, 2107-2110.
- Zhang Y., and G.R. Carmichael, 1999: The role of mineral aerosol in tropospheric chemistry in East Asia – a model study. *J. App. Chem.*, **38**, 353- 366.
- Zuberi, B., A.K. Bertram, C.A. Cassa, L.T. Molina and M.J. Molina, 2002: Heterogeneous nucleation of ice in $(\text{NH}_4)_2\text{SO}_4\text{-H}_2\text{O}$ particles with mineral dust immersions. *Geophys. Res. Lett.*, **29**(10), doi: 10.1029/2001GL014289.